

Vibronic and electronic excitations
of large organic molecules in gas and
condensed phase

Dissertation zur Erlangung des
naturwissenschaftlichen Doktorgrades
der Julius-Maximilians-Universität Würzburg
vorgelegt von
Dominique Hübner

aus Schweinfurt
November 2010

Eingereicht am 26.11.2010

bei der Fakultät für Physik und Astronomie

Gutachter der Dissertation:

1. Gutachter Prof. Dr. E. Umbach
2. Gutachter Prof. Dr. J. Geurts

Prüfer der mündlichen Prüfung: 20.05.2011

- 1.Prüfer: Prof. Dr. E. Umbach
- 2.Prüfer: Prof. Dr. G. Reents

Contents

1	Introduction	1
2	Experimental / Theoretical Background	5
2.1	LEED	6
2.2	HREELS	8
2.2.1	Basics	8
2.2.2	Dipole scattering	11
2.2.3	Impact scattering	14
2.2.4	Negative ion resonance	16
2.3	NEXAFS	16
2.3.1	NEXAFS-process	17
2.3.2	Franck-Condon-Principle	19
2.4	Group theory	21
3	Systems under investigation	27
3.1	NTCDA	27
3.1.1	NTCDA crystal	28
3.1.2	Monolayer structures on Ag(111)	30
3.1.3	NTCDA multilayers	32
3.2	Naphthalene	33
3.3	ANQ	33

4	Experimental details	37
4.1	HREELS apparatus	37
4.2	SPA-LEED	40
4.3	Gasphase measurements	41
4.3.1	Gas cell	42
4.3.2	Beamlines	44
5	Results and Discussion	47
5.1	Naphthalene gas phase	47
5.2	Naphthalene condensed phase	57
5.3	ANQ gas and condensed phase	67
5.4	HREELS: NTCDA room temperature multilayers	80
5.5	HREELS: NTCDA room and low temperature phase	92
5.6	NTCDA/Ag(111) monolayers	103
5.7	SPA-LEED results for NTCDA multilayers	124
6	Zusammenfassung / Conclusions	135
A	Excited states of Naphthalene	139
B	NTCDA A_g modes	141
C	SPA-LEED annex	145

List of Figures

2.1	Escape depth of electrons versus electron energy	6
2.2	Schematic overview of a LEED optic and the Ewald construction	7
2.3	Dipole field of an incoming electron and parameters involved in dipole scattering	9
2.4	Fourier spectrum of a monochromatic electron	10
2.5	Surface selection rule for the excitation of a dynamic dipole . .	12
2.6	Schematic sketch of the NEXAFS process for a diatomic molecule	17
2.7	Illustration of the Franck Condon principle	21
3.1	Sketch of the NTCDA molecule	27
3.2	NTCDA molecular crystal viewed from different directions . .	29
3.3	STM, LEED and real space suggestion for a relaxed monolayer	31
3.4	STM, LEED and real space suggestion for a compressed mono- layer	32
3.5	Sketch of a naphthalene molecule.	33
3.6	A sketch of the ANQ molecular crystal	34
3.7	Sketch of an ANQ molecule.	35
4.1	Schematic overview of a HREELS spectrometer	39
4.2	Schematic overview of a SPA-LEED optics	41
4.3	Schematic overview of the gas cell vacuum chamber	43
4.4	Schematic overview of the gas cell	45
5.1	C-K edge NEXAFS spectrum of gas phase h8-naphthalene . .	51

5.2	Comparison of the high-resolution NEXAFS spectra for d8- and h8-naphthalene in the gas phase	53
5.3	Fit of the NEXAFS spectra of non-deuterated and predeuterated naphthalene	56
5.4	Overview of NEXAFS C K-edge spectra of naphthalene h8 and g8 in both, gas and condensed phase	60
5.5	Detailed comparison of the first and second resonance for h8 naphthalene in gas and condensed phase	62
5.6	Comparison of the third and fourth resonances of naphthalene in gas and condensed phase	63
5.7	Comparison of ANQ O-K edge spectra in gas and condensed phase	70
5.8	Fit results of ANQ gas phase data	71
5.9	O-K edge NEXAFS spectrum of the Br ₂ Cl ₂ ANQ derivate . . .	74
5.10	Fit results for the Br ₂ Cl ₂ ANQ derivate	76
5.11	30 ML NTCDA/Ag(111) prepared at room temperature	84
5.12	HREELS spectra of 3, 6 and 30 ML NTCDA/Ag(111)	88
5.13	Thickness dependent intensity evolution of NTCDA vibronic peaks	89
5.14	HREELS multilayer spectra of NTCDA/Ag(111) for both, room and low temperature phase.	94
5.15	HREELS spectra for different film thicknesses and growth rates.	97
5.16	HREELS electronic excitation spectra for different NTCDA films.	99
5.17	EEL spectra for Ag(111) and NTCDA monolayer in different phases	106
5.18	Vibronic spectrum of a NTCDA monolayer	109
5.19	Flowchart of the fit process for the A _g modes	111
5.20	Vibrational spectrum taken at 20 eV to include electronic excitation	113
5.21	Fit results for A _g modes	114
5.22	Evolution of vibronic peaks from monolayer to multilayer for room and low temperature substrate	117

5.23	NTCDA vibrational spectrum of the low temperature phase transition	120
5.24	Submonolayer phase transition between multilayer islands . . .	122
5.25	NTCDA molecule crystal together with a glide reflection symmetry operation highlighted	125
5.26	SPA-LEED pattern of 30 ML NTCDA/Ag(111) and real space suggestion	127
5.27	Assignment of diffraction spots for the NTCDA multilayer pattern	129
5.28	Symmetry selection rules for the NTCDA multilayer LEED pattern	130
5.29	Comparison of NTCDA and CuPc LEED pattern	132
5.30	Film thickness dependent NTCDA SPA-LEED pattern	133
C.1	XPS spectra before and after electron irradiation	146
C.2	QMS comparison of sublimated and unsublimated NTCDA . .	147
C.3	Relaxed monolayer LEED pattern with additional impurity spots	148

Chapter 1

Introduction

Today there are many technical developments we do not want to miss. Many of these originate from fundamental physics research. Often great technical and economical progress is based on fundamental research. ‘Economists have shown, that 23% of the US gross national product results from the breakthrough in quantum mechanics’ [1]. A current example is the nobel prize 2007 in physics for GMR (Giant Magnetic Resistance) which led to miniaturization of data storage devices.

Today most electronic devices contain highly sophisticated semiconductor circuits which are continuously driven to smaller sizes. This leads to an increased influence of surface and interface related effects. Therefore tools and methods of surface science turn more and more from purely fundamental questions towards research and development of applied processes. This actually coincides with another nobel prize in 2007, namely with that in chemistry for studies of chemical processes on solid surfaces.

A promising field beside conventional semiconductors is research in new organic materials with numerous interesting optical and electronic properties. Organic thin films have a wide field of possible applications like organic light emitting devices (OLED) [2, 3], thin film displays [4], field effect transistors (OFET) [5, 6] and solar cells (OPV) [7, 8] which are already realized. Properties of organic thin films can be tailored by a variety of parameters like preparation conditions (temperature, organic flux, substrate) or via the molecules by size, shape and functional groups. In contrast, there is still a lack of knowledge about many fundamental aspects of organic thin films. In order to be able to produce, e.g. long range ordered films of these materials it is mandatory to understand the molecule-substrate and molecule-molecule interaction. Therefore there is a great interest in all questions regarding interactions within organic thin films and the resulting properties of organic thin

films. Especially the influence of functional groups and of the morphology upon properties is of interest.

Many theoretical and experimental techniques have been applied to these systems with success. In the framework of this thesis near X-ray absorption fine structure (NEXAFS), high resolution electron energy loss spectroscopy (HREELS) and spot profile low energy electron diffraction (SPA-LEED) were applied. As the intermolecular interaction is of special interest, condensed phase data will be compared to data taken from molecules in gas phase. The question of intermolecular and intramolecular interaction is addressed by NEXAFS spectroscopy. Therefore thin films deposited on different substrates are compared with the according spectra taken in gas phase. Molecules under investigation are NTCDA, ANQ and naphthalene.

The work will start with an investigation on the intramolecular coupling in naphthalene molecules in the gas phase. The C-K edge NEXAFS spectra are assigned with help of *ab initio* calculations and special emphasis is put on the explanation of the vibronic fine structure. Then we turn our attention towards intermolecular interaction. The condensed phase naphthalene will be compared and discussed together with gas phase results. Interesting changes lead to the question whether the interaction in organic thin films can be explained by mere van-der-Waals interaction.

In the next step, for a molecule with an asymmetric functional group (ANQ) and rich vibronic fine structure at the oxygen k edge NEXAFS data will be discussed for three different cases. First the comparison of ANQ in gas and condensed phase is presented. This is followed by an ANQ derivate in order to address questions of intramolecular interaction. The chapter will be finished by a short comparison of additional molecules in gas and condensed phase.

Further more a part of this work is devoted to the model molecule NTCDA deposited on an Ag(111) single crystal surface. This molecule is interesting in view of applications [9, 10] and fundamental research. The properties of the molecule are examined with HREELS for submonolayer and multilayer films with respect to vibronic and electronic excitations. First a detailed discussion of the vibrational properties of multilayer films prepared at room temperature will be given. Then the influence of the growth parameters on the vibrational and electronic structure of thick films will be discussed with a focus on the resulting changes for low substrate temperature. This is followed by a summary of the results for the NTCDA/Ag(111) monolayer with respect to vibronically and electronically excited states, where especially the question of molecule-substrate interaction and a low temperature phase transition will be addressed.

The resulting diffraction pattern for room temperature deposited films found during HREELS measurements were additionally investigated by SPA-LEED as function of film thickness and preparation parameters.

Chapter 2

Experimental Techniques and Theoretical Background

Low energy electrons are a highly suitable tool for surface sensitive analysis. This is on the one hand due to the high cross section with matter which can also be derived from the universal escape depth of electrons in matter (see.Fig.2.1).

On the other hand investigations are almost damage free as long as the primary energy of the electrons is small ($< 10\text{eV}$) and low currents are being used ($I \approx 1 \cdot 10^{-6} - 1 \cdot 10^{-9} \text{ A}$). Especially in organic monolayers an excitation can be efficiently dissipated. Thus in this work no beam damage in the covalently bound monolayers was found during the experiments.

In the scope of this work adsorbed molecular films have been investigated by two different electron methods. One is SPA-LEED (**S**pot-**P**rofile-**A**nalysis-**L**ow-**E**nery-**E**lectron-**D**iffraction), where elastically backscattered and interfering electrons are used to analyze surface the periodic surface geometric structure. The second is HREELS (**H**igh-**R**esolution-**E**lectron-**E**nery-**L**oss-**S**pectroscopy) where inelastically scattered electrons are used to analyze vibronic and electronic excitations of the sample.

Another main experimental method used was high resolution **N**ear **E**dge **X**-ray **A**bsorption of **F**ine **S**tructure (NEXAFS), which is a well established experimental tool and was used to analyze electronic and vibronic properties of organic thin films and organic molecules in the gas phase.

The basics of these methods will be outlined briefly in the following with a focus on relevant aspects for this work.

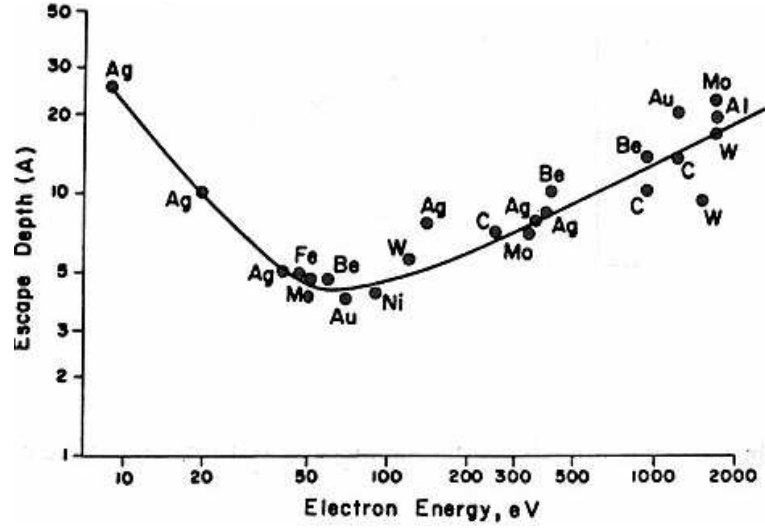


Figure 2.1: Escape depth of electrons versus electron energy

2.1 LEED as surface sensitive structure tool

In order to estimate the structural properties of the surface and to investigate the adsorbate superstructures of organic molecules on the Ag(111) surface LEED experiments were performed. In order to do LEED experiments electrons are accelerated to 10-200 eV, targeted upon the surface leading to an interference pattern via elastic backscattering. The elastically scattered electrons are made visible by a fluorescence screen and in case of constructive interference diffraction spots are observed.

Like for any elastic scattering the equation

$$\vec{k}_f - \vec{k}_i = n \vec{G} \quad (n \text{ integer})$$

for an intensity maximum must be satisfied, where \vec{k}_i is the wave vector of the incident and \vec{k}_f the wave vector of the scattered electron, \vec{G} is a reciprocal lattice vector of the surface unit cell.

Due to the low mean free path in the applied energy range the electrons are scattered predominantly only in the first surface layer. Therefore the reciprocal lattice points for diffraction become diffraction rods, as the periodicity perpendicular to the surface does not contribute. The diffraction term simplifies to wave vectors parallel to the surface, i.e. the parallel components of incoming and outgoing wave vector differ by a reciprocal surface lattice

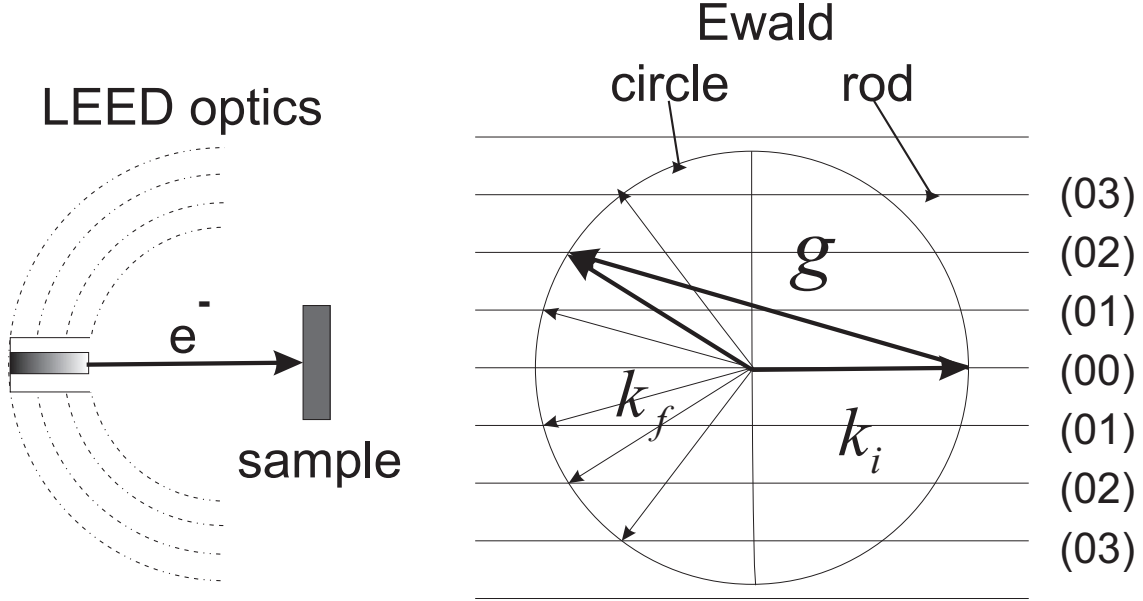


Figure 2.2: On the left side an overview of a LEED-Apparatus with electron gun and grids is shown. On the right side, the reciprocal space Ewald construction for diffraction at a surface including Ewald rods is shown.

vector, which does not necessarily coincide with a volume vector due to a possible reconstruction. The diffraction pattern is explained by an Ewald construction but now with diffraction rods instead of spots [11], where the crossing between the reciprocal lattice rods and the Ewald circle gives the direction of k_f leading to the possible diffraction spots. (see Fig.2.2).

For adsorbate superstructures the common matrix notation will be used, which is defined as written below [12]:

$$\left. \begin{aligned} \vec{b}_1 &= m_{11} \vec{a}_1 + m_{12} \vec{a}_2 \\ \vec{b}_2 &= m_{21} \vec{a}_1 + m_{22} \vec{a}_2 \end{aligned} \right\} \vec{b} = \hat{M} \cdot \vec{a}$$

Here $\vec{a}_{1/2}$ are the vectors of the substrate unit cell and $\vec{b}_{1/2}$ the vectors of the adsorbate superstructure. If all entries m_{ij} are integer, the superstructure is called commensurate, i.e. the lattice of the superstructure fits to the lattice of the substrate. In case at least one m_{ij} is not integer the superstructure is called incommensurate. The diffraction spots are related to the reciprocal lattice vectors via:

$$\vec{b}^* = \hat{M}^{-1} \cdot \vec{a}^*$$

Therefore by using the measured diffraction pattern with the inverse matrix one can derive the real matrix M leading to superstructure basis vectors. But due to the missing phase information in the diffraction pattern this back transformation is not unambiguous.

2.2 High Resolution Electron Energy Loss Spectroscopy (HREELS)

2.2.1 Basics

The technique of using inelastic scattering of low energy electrons to detect vibrations of well defined solid state surfaces has been discovered by Probst and Piper 1967 [13]. Via this pioneering work the great potential of vibrational spectroscopy for surface science and chemistry of adsorbed molecules became clear. In the 70ies Ibach and coworkers succeeded in gaining a resolution of 10 meV [14], which made systematic studies of adsorbate systems possible [15]. The instrumental equipment as well as the theoretical description of the electron optics improved continuously so that spectrometers with $\Delta E < 1\text{meV}$ are commercially available today. But already with a resolution of $\Delta E < 8\text{meV}$ ($\sim 70\text{ cm}^{-1}$; $1\text{meV} \hat{=} 8.066\text{ cm}^{-1}$) questions about bonding, adsorption sites and symmetry both within the adsorbate and between adsorbate and substrate can be investigated for many systems.

The advantage of the method is the almost damage-free measurement due to the low primary electron energy (2-5 eV) and the low currents in the range of nanoampere. HREELS is also (beside infrared spectroscopy) an excellent tool to investigate reactions and intermediate products as these can be identified by their normal modes. Fundamental molecular and solid state vibrations have excitation energies of up to 500 meV ($\sim 4000\text{ cm}^{-1}$) [16], although the excitation probability might be very low (like 10^{-5} [15]).

In the theoretical description, the inelastic scattering of electrons at surfaces is divided into different regimes, namely *dipole scattering*, *impact scattering* and *negative ion resonance scattering* [15, 17–30]. The selection rules of the different scattering mechanisms offer a key to understand the adsorbate complex. In the following these mechanisms will be described in detail.

Qualitative description

A schematic description of the interaction of an electron with a harmonic oscillator on a metal surface is shown in Fig. 2.3 [31]. The electric field of an

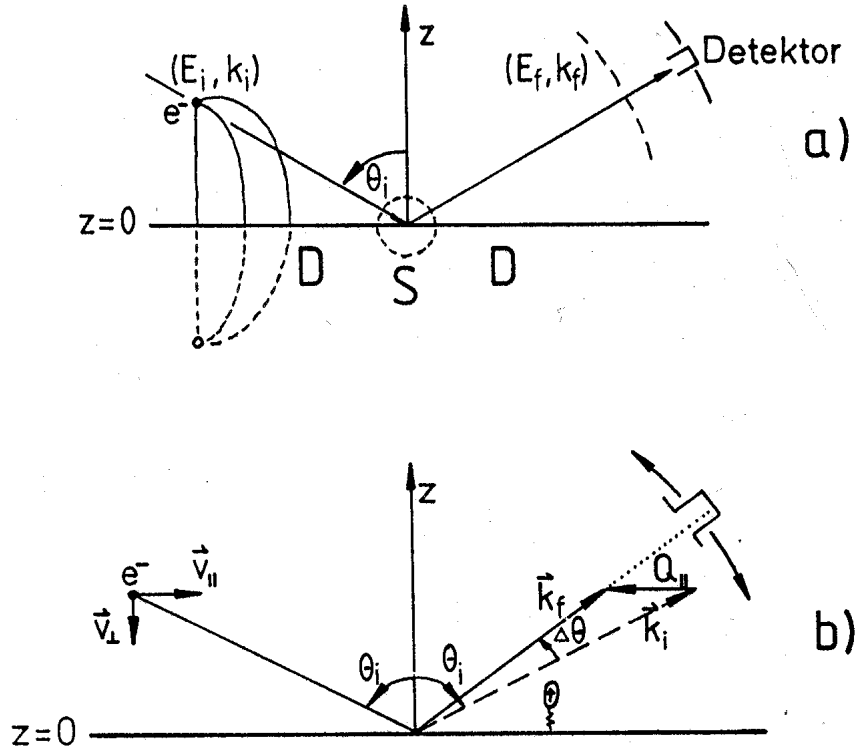


Figure 2.3: Upper part: Dipole field of a incoming electron with primary energy E_i and wavevector k_i . The scattering regimes for dipole scattering (D) and impact scattering (S) are highlighted. Lower part: Parameters involved in dipole scattering together with the resulting small angle electron lobe [31].

incoming electron with low primary energy ($E_{pr} < \hbar\omega_{Plasmon}$) in regime D is well described by a multipole expansion, the dipole part of which couples to the dipole field of charge and image charge. For higher energies this model is not valid anymore as the relaxation of the metal atoms is not fast enough, but it can be used for energies $\hbar\omega_{vib} \ll \hbar\omega_{Plasmon}$ as good approximation [32].

Due to electrodynamic reasons the electric field at a metal surface is always perpendicular to it, since the parallel components induce antiparallel image components within the metal which in turn reduce the parallel component of the electric field ($E_{||}$) to zero [33].

Calculating the Fourier components of the field of an incoming electron and its image charge,

$$E(t) = \int E(\omega) e^{-i\omega t} d\omega,$$

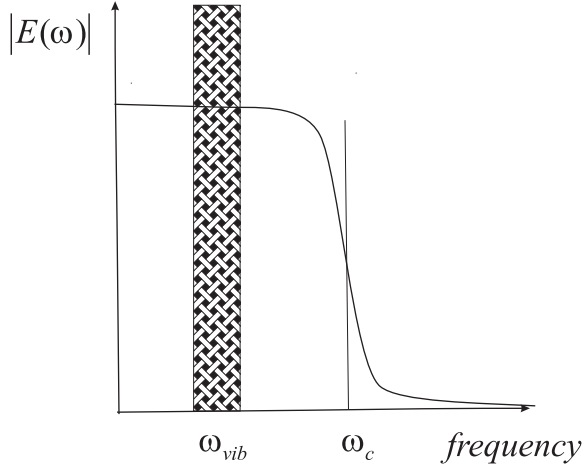


Figure 2.4: Fourier spectrum of a monochromatic electron with the cut off frequency of ω_c where only a small band around ω_{vib} actually contributes to the excitation of a vibration.

one obtains a continuous distribution with a cut off frequency at $\omega_c \approx E_{Pr} / \hbar$ for electrons with a primary energy of E_{Pr} (see Fig.2.4) [32]. From this distribution only a small band around ω_{vib} contributes to the excitation of a vibration. Therefore an incoming monochromatic electron beam leads to a broadband excitation spectrum.

For distances $d < d_{vib}$ ($d_{vib} = Q_{||}^{-1} \approx 2 E_{Pr} / (k_i \hbar \omega) \approx v_e / \omega_{vib}$) an incoming electron can excite vibrations on a surface [15]. With this approximation one gets with $E_{Pr} = 2.3$ eV and $\hbar \omega_{vib} = 1000 \text{ cm}^{-1}$ a value of $d < 60 \text{ \AA}$. Accordingly the cut off frequency is found to be ω_c : $d_c \approx 2 \text{ \AA}$ and for $\omega_{Plasmon}$: $d_{Pl} \approx 1 \text{ \AA}$. The values of $d(\omega)$ can be used as rough estimate of the range of the respective Fourier components of the electric field into the vacuum.

For significantly lower distances to the surface the applied model of a smooth surface breaks down as the electron sees the periodicity of the surface. The assumption that the field of the electron is perpendicular to the surface (resulting in the fact that this field can only couple to dipole moments \perp to the surface) is not justified any more. The exchange potential is no longer appropriately described by a multipole expansion the dipole part of which couples to the dipole scattering regime, as there are additional contributions of inelastic scattering of the electrons at atomic cores (impact scattering). In Fig. 2.3 both regimes (dipole approximation valid: $E_{||} \approx 0$; dipole approximation not valid: $E_{||} \neq 0$) marked by S and D according to dipole and impact scattering, respectively, are shown depending on which regime is predominant.

Theoretical description

Theoretically the interaction of an electron with a harmonic oscillator (with a dynamic dipole moment p_{dyn}) at a surface can be described in different ways. Depending on the treatment the system can be viewed in a quantum mechanical or classical way [32].

In the classical description, the scattering electrons and the harmonic oscillator are described by their classical trajectories and by their electromagnetic fields (e^- : dipole field due to charge and image charge; $\hbar\omega$: dynamic dipole field due to an excited vibration), in which via the $\hbar\omega$ -field work is done at the electrons. The quantum mechanical description starts with an incident plane electron wave, which has a certain excitation probability for a harmonic oscillator with an eigenfrequency of ω . In their semiclassical description Evans and Mills [24] calculated the vibrational excitation and the energy loss of the electron due to an oscillating dipole field by time dependent perturbation theory.

A semi quantum mechanical theory assumes a coherent excitation of harmonic oscillators $\hbar\omega_i$ by the dipole field of the incoming electron.

Multiple scattering is only included in a full quantum mechanical description of a surface vibration. Mathematically the problem is not exact solvable, therefore different approximation procedures like the first Born approximation and the assumption of a harmonic oscillator are necessary.

2.2.2 Dipole scattering

A molecular dipole above a metal surface creates an image dipole within the surface. The resulting dipole moment μ_z is twice the z component when the dipole is perpendicular to the surface, while a parallel component of $\vec{\mu}$ and its image dipole will cancel out each other (see Fig.2.5) in the far field of the two resulting dipoles.

The electrical field created by charge and image charge is described by:

$$E(t) = \int E(\omega) e^{-i\omega t} d\omega$$

This field is perpendicular to the surface and has an amplitude of [33]

$$E(r_e) = \frac{e}{2\pi\epsilon_0} \frac{1}{r_e^2}$$

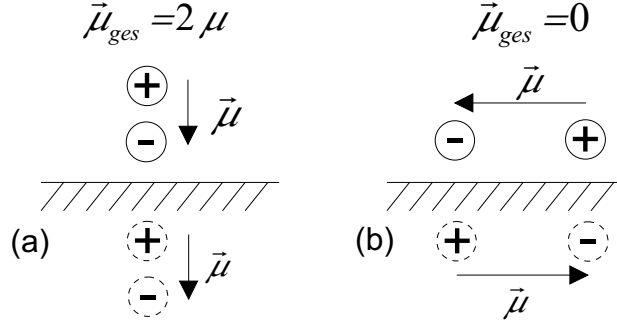


Figure 2.5: (a) Dipole $\vec{\mu}$ and image dipole perpendicular to a metal surface lead in the far field to a $\vec{\mu}_{ges} = 2\mu$. (b) Dipole $\vec{\mu}$ and image dipole parallel to a metal surface lead in the far field to a $\vec{\mu}_{ges} = 0$.

at the position of the adsorbed molecule.

For the wave vector of the incoming (\vec{k}_i) and outgoing electron (\vec{k}_f) the law of momentum conservation holds. Via dipole scattering only a momentum parallel to the surface is transferred. Therefore:

$$\vec{k}_{||i} - \vec{k}_{||f} = \vec{Q}_{||} + n\vec{G}; n \in \mathbf{N}$$

with

$$|\vec{G}| \gg |\vec{k}_{||i}|, |\vec{k}_{||f}|, |\vec{Q}_{||}|$$

where \vec{G} is a reciprocal lattice vector of the surface.

Due to energy conservation the following applies for the excitation of a vibration from the ground state.

$$E_i - E_f = \hbar\omega$$

with

$$E = \frac{\hbar^2 k_i^2}{2m_e} = \frac{m_e v_e^2}{2}$$

Momentum conservation for $n=0$ leads to

$$\frac{\hbar^2 k_i^2}{2m_e} = \frac{\hbar^2 (\vec{k}_i - \vec{Q}_{||})^2}{2m_e} + \hbar\omega.$$

Due to $\hbar\omega \ll E_i$, the term with $|\vec{Q}_{||}^2|$ can be neglected and one obtains

$$|\vec{Q}_{||}| \approx |\vec{k}_i| \frac{\hbar\omega}{2E_i} = \frac{\omega}{v_e}.$$

For a primary electron energy of $E_i \approx 5 \text{ eV}$ ($v_e \approx 1.3 \cdot 10^6 \frac{\text{m}}{\text{s}}$, $|\vec{k}_i| \approx 1.1 \cdot 10^8 \text{ cm}^{-1}$) and $\hbar\omega = 100 \text{ meV}$ ($\omega \approx 1.5 \cdot 10^{14} \text{ s}^{-1}$) one gets $\frac{|\vec{Q}_{||}|}{|\vec{k}_i|} \approx 0.01$. Therefore one can write $\Delta\Theta = \Theta_f - \Theta_i$ (with $\Delta\Theta/\Theta_i \ll 1$) (see Fig.2.3.b):

$$\Delta\Theta \approx \frac{\hbar\omega}{2E_i} \cos \Theta_i.$$

An incident angle of $\Theta_i = 60^\circ$ leads for this example to $\Delta\Theta \approx 0.3^\circ$.

The cross section for the excitation of a vibration on a surface for specular geometry is given by Fermis golden rule [26], [27]:

$$\frac{d\sigma}{d\Omega} = \left(\frac{me}{\pi\epsilon_0\hbar^2} \right)^2 \mu^2 \left| \frac{\vec{k}_f}{\vec{k}_i} \right|^2 \frac{1}{\cos \Theta_i} \frac{|\vec{k}_{||i} - \vec{k}_{||f}|^2}{|\vec{k}_i - \vec{k}_f|^4},$$

where the dynamic dipole moment μ is:

$$\mu = \int \Phi_f \mu_z \Phi_i d\tau = \langle \Phi_f | \mu_z | \Phi_i \rangle.$$

This is true for an excitation from the ground state $|\Phi_i\rangle$ into a final state $\langle \Phi_f |$. The inversion of the electron momentum \vec{k}_\perp perpendicular to the surface is instantaneous in the case of a textureless surface potential.

By using symmetry arguments one can find selection rules for dipole scattering. The cross section $d\sigma/d\Omega$ is different from zero if the matrix element

$$\mu^2 = |\langle \Phi_f | \mu_z | \Phi_i \rangle|^2$$

does not vanish, i.e. when $\langle \Phi_f | \mu_z | \Phi_i \rangle$ is totally symmetric in respect to the symmetry operation of the according point group. $\Phi_i \Phi_f^*$ have to transform like μ_z (i.e. like a translation in z direction). As z is totally symmetric also $\Phi_i \Phi_f^*$ has to be totally symmetric. If Φ_i is the ground state $|0\rangle$ which is totally symmetric then the wave function of the final state Φ_f has to be totally symmetric too. So only vibrations belonging to the totally symmetric representation can give a contribution to the dipole scattering (see [15] p.171).

These arguments lead to the following consequences:

- Forward scattering is strongly dominant in dipole scattering. The electrons are scattered in a small angular lobe around the elastically reflected electron beam, within an angle of $\Delta\Theta$ 2° up to 4° . Spectra taken in specular geometry are dominated by dipole scattering. For scattering angles larger than 5° dipole scattered electrons are very rare.
- Only vibrations with a non zero dynamic dipole moment perpendicular to the surface can be excited. This rule is true for the dynamic dipole but not for the actual motion of atoms which can be parallel to the surface. This means vibrations that are perfectly parallel to the surface can lead to a dynamic dipole moment μ_z , but only if the molecule is strongly bound to the surface. The surface selection rule is weakened for a growing distance between dipole and surface, i.e. for thicker films.
- Up to now the discussion was about single scattering by an adsorbate. But the actually measured intensity is the sum over the intensities from all molecules. In well ordered layers coherent scattering is therefore possible leading to an intensity which can be orders of magnitude higher compared to disordered layers. [19]. Furthermore the full width at half maximum of the elastically scattered electrons is noticeably smaller in ordered films.

2.2.3 Impact scattering

If the electron is scattered directly by the atomic potential of the adsorbate and not by long range dipole interaction, this leads to a different angular scattering distribution (see Fig. 2.3a S). A high amount of momentum is transferred to the surface and therefore the scattered electrons can have a different angular distribution. They are almost isotropically distributed over the half space which leads to a much lower intensity than dipole scattering, due to a small angular analyzer acceptance and the small cross section for these losses. Impact scattered electrons can hardly be identified in the specular lobe of dipole scattered electrons. Therefore impact scattering is measured in off specular geometry because the signal to noise ratio is better in absence of dipole scattered electrons. Thus by measuring in specular and off-specular geometry one can distinguish both scattering regimes.

As impact scattering is due to a short range interaction a theoretical description has to start with a microscopic model, where a detailed knowledge of the scattering potential between electron and adsorbate is mandatory.

The stray amplitude $f(\vec{k}_i, \vec{k}_f, \vec{R})$ depends upon the wave vector of the incoming (\vec{k}_i) und outgoing electron wave (\vec{k}_f) and the atom coordinates \vec{R} . The

matrix element for the excitation of a certain vibration s with the normal coordinate Q_s and eigenvalue $\xi_{i\alpha}^{(s)}$ is therefore according to [15]:

$$\begin{aligned} M(\vec{k}_i, \vec{k}_f, +s) &= \langle n_s + 1 | f(\vec{k}_i, \vec{k}_f, \vec{R}) | n_s \rangle \\ &= \sqrt{n_s + 1} \left(\frac{\hbar}{2N\omega_s} \right)^{1/2} \left(\frac{\partial f}{\partial Q_s} \right) \end{aligned}$$

with

$$\left(\frac{\partial f}{\partial Q_s} \right) = \sum_{i\alpha} \left(\frac{\partial f}{\partial R_{i\alpha}} \right) \frac{\xi_{i\alpha}^{(s)}}{\sqrt{M_i}}$$

.

The vibrational levels are according to Bose Einstein statistics occupied as follows:

$$n_s = \frac{1}{e^{\frac{\hbar\omega}{k_B T}} - 1}.$$

With $\left(\frac{\partial V}{\partial Q_s} \right) = \sum_i \frac{\xi_{i\alpha}^{(s)}}{\sqrt{M_i}} \frac{\partial V(\vec{R})}{\partial R_{i\alpha}}$, one gets the wave functions $|\Psi_i\rangle$ und $\langle\Psi_s|$ for incoming and outgoing electron waves:

$$\left(\frac{\partial f}{\partial Q_s} \right) = \langle\Psi_s| \frac{\partial V}{\partial Q_s} |\Psi_i\rangle$$

Due to parity conservation one can find selection rules for impact scattering which depend on the scattering geometry (see Fig.2.3.b):

- The stray amplitude in specular geometry is zero if the normal coordinate Q_s of the vibration is antisymmetric to a mirror operation at a plane which is both perpendicular to the surface and perpendicular or parallel to the impact plane.
- The stray amplitude in specular geometry is zero for vibrations that are antisymmetric with respect to a twofold rotation axis perpendicular to the surface.
- If the stray plane is a mirror plane and the normal coordinates Q_s are antisymmetric with respect to mirroring at this plane then the stray amplitude will vanish for the hole stray plane.

2.2.4 Negative ion resonance

Beside dipole and impact scattering there is a third scattering mechanism. In case of a so called *negative ion resonance* an electron is temporarily captured which leads to the formation of a negative ion. The lifetime of this quasi-bound state is typically in the range of $10^{-10} - 10^{-15}$ s, which is much longer than the time necessary for the unhindered transition through the molecule. A negative ion resonance can be identified by its cross section including the Lorentz line shape and energy dependence.

The resonances can be divided into one particle shape resonances and resonances with core excitation [30]. In a shape resonance the electron is located in a quasi stable level within the centrifugal barrier of the molecule, which is in its electronic ground state. Here mainly the shape of the potential is responsible for capturing the electron. As the differential cross section of the negative ion resonance is due to the symmetry of the resonance state the angular distribution might be completely different from that of dipole and impact scattering.

Resonance scattering can be recognized by the following characteristics:

- The cross section for certain vibronic excitations increases for specific primary energies up to several orders of magnitude.
- The cross section for excitation of vibronic overtones is increased in comparison to that of dipole or impact scattering. Overtones up to excitations of $\nu = 10$ are reported [30].
- The angular distribution of scattered electrons at the resonance energy is completely different from that far off resonance.

2.3 Near Edge Xray Absorption Fine Structure

Organic molecules were investigated by means of NEXAFS (**N**ear **E**dge **X**-**R**ay **A**bsorption **F**ine **S**tructure also known as **XANES X-Ray Absorption Near Edge Spectroscopy**). The theoretical aspects will be discussed briefly in the following; a detailed description can be found, e.g., in Ref. [34].

2.3.1 NEXAFS-process

In the NEXAFS process, a core electron is excited into an unoccupied orbital. This method can provide information about the geometric orientation and electronic structure of a sample, in particular of the unoccupied states. Especially it is sensitive to chemically differently bound atomic species within a molecule. For a diatomic molecule a schematic illustration of the NEXAFS process is displayed in Fig. 2.6. The fundamental relations of NEXAFS theory are outlined in the following.

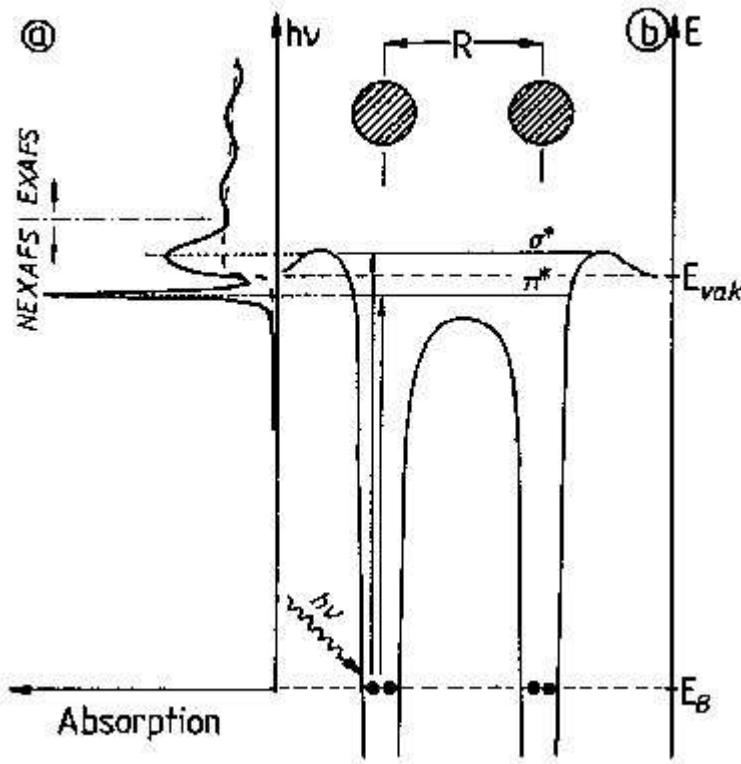


Figure 2.6: Schematic sketch of the NEXAFS process for a diatomic molecule. A variable photon source $h\nu$ excites core electrons into an unoccupied (anti bonding(*)) molecular orbital σ^* or π^* here [34].

The core electrons are excited by monochromatic electromagnetic radiation with the tunable energy $h\nu$. If this energy exceeds the ionization threshold E_i of the investigated level, the electrons are detected as photoelectrons with a high cross section near this energy. The well known absorption edges are

found at energies around $h\nu=E_i$. Beside the excitation into continuum states as final state also an excitation into unoccupied orbitals is a very effective channel. In Fig. 2.6 as example the excitation into the **Lowest Unoccupied Molecular Orbital** (LUMO) of a diatomic molecule is displayed. This orbital is bound according to Fig. 2.6 as it is found below the vacuum level, whereas other levels are not necessarily bound. For aromatic organic molecules the LUMO and the HOMO (**Highest Occupied Molecular Orbital**) do often have π symmetry. Unoccupied, anti-bonding molecular orbitals are often marked by an asterisk(*).

The cross section is high if the photon energy $h\nu$ equals the excitation energy E_α , which is necessary to excite a core electron into an unoccupied molecular orbital.

$$E_\alpha = E_i - h\nu,$$

where $h\nu$ is the photon energy for the excitation.

Like Koopman's theorem for photoelectron spectroscopy this relation is also an approximation, because the reaction of the other electrons in a molecule upon an excitation is not included, with the difference that here the excited electron is responsible for the main screening. Nevertheless with this description one can gain information about the electronic structure especially of the unoccupied states. Both, intramolecular and intermolecular interactions, for example the influence of a chemical bonding or the adsorbate-substrate interaction can be addressed.

Quantum mechanically the absorption cross section is derived by Fermis golden rule:

$$P_{if} = \frac{2\pi}{\hbar} |\langle f | \mathbf{A} \cdot \hat{\mathbf{p}} | i \rangle|^2 \varrho_f(E)$$

where $|f\rangle$ and $|i\rangle$ are the wave functions of the initial and final state, \mathbf{A} the electromagnetic vector potential, and $\hat{\mathbf{p}}$ the momentum operator.

Some data will be compared with Hartree Fock based ab initio calculations (GSCF3 code), using a code that has been developed by N. Kosugi. A detailed description is found in Ref. [35].

The calculation of the ground state is established semi empirical, by ab initio and DFT calculations, whereas the calculation of the final state is more difficult. For a correct description of the final state more orbitals have to be taken into account, as the complete absorption spectrum has to be described including resonances and the interaction of energetically higher channels with lower ones.

The actual measurement is done by the help of secondary channels, as the created core hole will be filled by an electron from a higher level. The core

level can be directly occupied by a higher level electron, by emission of a photon (fluorescence) or by decay via emission of an other electron (Auger). For the excitation of low atomic number elements like carbon the non fluorescent decay is indeed the favorite channel. Within this work all data was taken using the Auger channel, which leads to an ionized molecule. Therefore a molecule as ion and/or an emitted electron can be detected. Both can be measured in total or partial electron/ion yield as a current or with help of a channeltron. Total electron/ion yield includes the measurement of processes due to secondary electrons leading to an overall high signal but at the cost of a lower signal to background ratio. For partial electron/ion yield a retarding voltage is applied in order to reduce the low energy electron/ion background.

2.3.2 Franck–Condon–Principle

In Fig. 2.7 a schematic view of the electronic potentials, including their vibrational levels, involved in an electronic excitation process are displayed for a diatomic molecule AB. Polyatomic molecules can still be described in an analogue way when the intermolecular distance coordinate R is replaced by a more abstract reaction coordinate.

The energetically lowest potential curve is the electronic ground state (AB). The vibrationally excited levels of the ground state are hardly populated at low temperatures though it has to be taken into account that already a temperature of 300K leads to an energy kT of 25 meV, which can be enough to activate low energy bending modes in large planar organic molecules.

A core electron, from the ground state potential AB, is excited during the NEXAFS process into an unoccupied molecular orbital with the potential curve AB+. The final state potential will shift to a different R_0^+ by ΔR , if the bonding distance of the molecule is changed due to the process. If the orbital is anti-bonding R_0 will increase, which is the case for the π^* resonances of organic molecules used in this work. The excitation process is described as a vertical transition within this picture so the final state will be a vibronically excited state, because an excitation into such a level has a maximum wave function overlap. Therefore the energy required for the excitation process according to Fig.2.7 is

$$\hbar\omega = E_a + nE_{vib} = E_v$$

where E_{vib} is the energy of a vibronic level in the electronically excited state and E_a is the adiabatic energy difference between initial and final electronic state both in the vibronic ground state. E_v is the energy difference of the vertical transition.

In this description an approximation is included, which is known as the Born Oppenheimer approximation [36]. It assumes that the nuclear motion is slow compared to the electronic excitation. Applying this to a wave function this can be written as product of the nuclear wave function ψ and the electronic wave function ϕ $\Psi(R,r) = \psi_{vib}(R) * \phi_{el}(r)$ of the nuclear (R) and electron (r) coordinates. Therefore the wave functions in the initial and the final state can be written as

$$|i\rangle = \phi_{el}^i * \psi_{vib}^0, \text{ and} \\ |f\rangle = \phi_{el}^f * \psi_{vib}^{n'}$$

where the electron wave functions of the electronic ground and excited state are ϕ_{el}^i and ϕ_{el}^f . ψ_{vib}^0 and $(\psi_{vib}^{n'})$ are the nuclear wave functions in the vibronic ground state of the electronic ground state and of a vibrationally excited state in case of the electronically excited state.

In order to describe the excitation probability, Fermis golden rule is applied and the vibrational part $\psi_{vib}^{i,f}$ can be separated, because the vector potential \mathbf{A} only affects the electronic part $\phi_{el}^{i,f}$ leading to:

$$P_{if} = 2\pi\hbar\rho_f(E) \cdot \left\langle \phi_{el}^f \psi_{vib}^f(R) \left| \mathbf{A} \cdot \hat{\mathbf{p}} \right| \psi_{vib}^i(R) \phi_{el}^i \right\rangle \\ = \underbrace{2\pi\hbar\rho_f(E) \cdot \left\langle \phi_{el}^f \left| \mathbf{A} \cdot \hat{\mathbf{p}} \right| \phi_{el}^i \right\rangle}_K \left\langle \psi_{vib}^f(R) \left| \psi_{vib}^i(R) \right\rangle \right.$$

Within the range of a vibronic progression (approx. 1 eV) the density of final states $\rho_f(E)$ usually does not change, leading to the assumption of K being constant within an electronic excitation. Therefore the relative intensity distribution described by the so called Franck-Condon factors, can be written as

$$FCF_{i \rightarrow f} = \left| \left\langle \psi_{vib}^f(R) \left| \psi_{vib}^i(R) \right\rangle \right|^2 = \int \psi_{vib}^f(R) \cdot \psi_{vib}^i(R) dR^2$$

In order to be separable by the experimental resolution the vibrational levels need to have energy differences of at least 100 meV. According to Fig. 2.7 the intensity of the adiabatic excitation, i.e. 00 (E_A), might be considerably smaller than for the excitation with the highest intensity, the so called vertical transition (E_V). The Franck-Condon shift, defined as $\Delta E_{FC} = E_V - E_A$, is used together with the energy of the vibronic level of the excited state $h\nu'$ in an empiric formula [38] to get an estimate for the vibrational ground state levels $h\nu_0$:

$$h\nu_0 = h\nu' \cdot (\Delta E_{FC}/1,2 + 1)$$

Using this the resulting energies can be compared to those measured by ground state spectroscopies like infrared or HREELS.

theoretical framework to predict physical properties by their behavior upon coordinate transformations (translation, mirroring, rotation, inversion) [39]. If a system is transformed into itself (*inverse*) by an operation, then this symmetry operation is called symmetric (*antisymmetric*). All possible independent symmetry operations of a system define its symmetry group. This classification is extremely helpful, as symmetry related properties of a system are identical for all systems within the same symmetry group. Therefore the symmetry drawn conclusions are independent of the details of the respective system (i.e. the actual shape of the involved wave function).

The basic vibrations of a free molecule are usually called normal modes. These are defined by the following terms:

- All atoms of the molecule move with the same frequency and phase.
- The vibration does not lead to a translation or rotation of the whole molecule.
- Every normal mode can be excited independently of the others vibrations.

Normal modes can be characterized via a set of symbols which simplify an imagination of the vibration.

ν : Valence or stretch vibrations lead to a change of one or more bonding lengths.

δ : Deformation or bending modes (in-plane) lead to a change of bonding angles while atomic distances stay essentially constant.

γ : Deformation or bending modes (out-of-plane) lead to a change of bonding angles while atomic distances stay essentially constant.

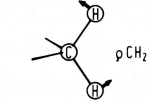
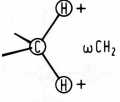
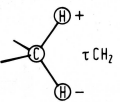
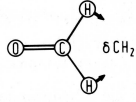
τ : Torsion lead to a change of the torsion angle (the angle between two planes with one common bond)

When larger units of a molecule are involved in a vibration some additional symbols are used:

These are rocking ρ , wagging ω , twisting τ and scissoring δ modes (see Fig. 2.1). A normal mode molecular vibration of an extended molecule is usually a combination of these in table 2.1 introduced subunit vibrations. Therefore often a sum of the according symbols is used to describe the vibration.

In contrast to the symmetry group which takes the symmetry elements of a static molecule into account, the symmetry race is introduced for vibrating

Table 2.1: Illustration for vibrations including larger subunits of a molecule.

Symbol	figure
ρ	
ω	
τ	
δ	

molecules. For many of the $3N-6$ ($3N-5$ for linear molecules) possible fundamental molecular vibrations the symmetry is different compared with those of the static molecule. The symmetry races are a set of symbols which describe the symmetry elements of the vibrating molecule with respect to the static molecule symmetry operations [39]. For example, Symbols like B_{3u} are used. The abbreviations used in this work are introduced briefly.

- (A) The symmetry with respect to the main axis (z-axis, being defined by the highest folded axis) is unchanged at any time during the motion.
- (B) The symmetry with respect to the main axis is not conserved during motion.
- The index g and u indicate that the vibration is symmetric/antisymmetric with respect to an inversion operation.
- Indices 1, 2 or 3 are used if there are, beside the main z-axis, additional symmetry operations conserved with respect to x or y axes.

Depending on the symmetry race conclusions about the physical properties of the oscillating molecule can be drawn, i.e. if there is a periodic change of the

Table 2.2: The symmetry races for the group D_{2h} [40]

race	activity				number of vibrations	sum
	IR	RE	RR	HR		
A_g	-	p	p	-	$r_x + r_y + r_z + 2m_x + 2m_y + 2m_z + 3n$	12
A_u	-	-	-	dp	$m_x + m_y + m_z + 3n$	5
B_{1g}	-	dp	ap	-	$r_x + r_y + m_x + m_y + 2m_z + 3n - 1$	4
B_{1u}	a	-	-	p	$n_0 + r_x + r_y + r_z + 2m_x + 2m_y + m_z + 3n - 1$	11
B_{2g}	-	dp	ap	-	$r_x + r_z + m_x + 2m_y + m_z + 3n - 1$	6
B_{2u}	a	-	-	p	$n_0 + r_x + r_y + r_z + 2m_x + m_y + 2m_z + 3n - 1$	11
B_{3g}	-	dp	ap	-	$r_y + r_z + 2m_x + m_y + m_z + 3n - 1$	11
B_{3u}	a	-	-	p	$n_0 + r_x + r_y + r_z + m_x + 2m_y + 2m_z + 3n - 1$	6
						Σ 66

a: infrared active

p: Raman or hyper Raman band

ap: in resonance Raman observable

dp: Raman or hyper Raman active, depolarized band

n : number of symmetry independent atoms, which are not on a symmetry element

n_0 : number of atoms in the symmetry center or intersection of several axes

r_x, r_y, r_z : number of symmetry independent atoms on a symmetry axis in x, y, z direction

m_x, m_y, m_z : number of symmetry independent atoms in a mirror plane, which are perpendicular to x, y, z. Atoms on the axis do not count.

dipole moment (*polarizability*), leading to infrared (*Raman*) active vibrations. As the group D_{2h} is of some importance the resulting symmetry races along with their activity are listed in table 2.2.

If a molecule is adsorbed on a surface or forming a molecular crystal, a reduction of the possible symmetry elements can occur. Then the symmetry group is reduced to a group with the according elements (see table 2.3). This can lead to change of symmetry races causing additional/less observable vibrations. Often the original symmetry group is still used to keep the original labeling of orbitals and symmetry races.

Table 2.3: symmetry reduction of D_{2h} due to, e.g. adsorption
 -infrared-active symmetry races are underlined

D_{2h}	D_2	$C_{2\nu}(z)$	$C_{2\nu}(x)$	$C_{2\nu}(y)$	$C_{2h}(z)$	$C_{2h}(x)$	$C_{2h}(y)$
A_g	A	<u>A_1</u>	<u>A_1</u>	<u>A_1</u>	A_g	A_g	A_g
A_u	A	A_2	A_2	A_2	<u>A_u</u>	<u>A_u</u>	<u>A_u</u>
B_{1g}	<u>B_1</u>	A_2	B_1	<u>B_2</u>	A_g	B_g	B_g
<u>B_{1u}</u>	<u>B_1</u>	<u>A_1</u>	<u>B_2</u>	<u>B_1</u>	<u>A_u</u>	<u>B_u</u>	<u>B_u</u>
B_{2g}	<u>B_2</u>	<u>B_1</u>	<u>B_2</u>	A_2	B_g	B_g	A_g
<u>B_{2u}</u>	<u>B_2</u>	<u>B_2</u>	<u>B_1</u>	<u>A_1</u>	<u>B_u</u>	<u>B_u</u>	<u>A_u</u>
B_{3g}	<u>B_3</u>	<u>B_2</u>	A_2	<u>B_1</u>	B_g	A_g	B_g
<u>B_{3u}</u>	<u>B_3</u>	<u>B_1</u>	<u>A_1</u>	<u>B_2</u>	<u>B_u</u>	<u>A_u</u>	<u>B_u</u>

Chapter 3

Systems under investigation

3.1 NTCDA

The molecule 1,4,5,8-Naphthalene-TetraCarboxylicacid-DiAnhydride (NTCDA) is often used, like Perylen-TetraCarboxylicacid-DiAnhydride (PTCDA) and Naphthalene-DiCarboxylicacid-Anhydride (NDCA), as modell molecular system. The NTCDA molecule (mass $M(C_{14}H_4O_6) = 268$ u) can be evaporated from a Knudsen cell [41].

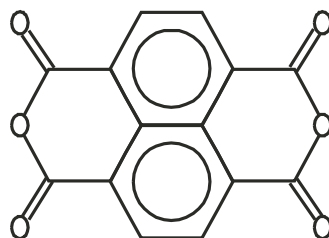


Figure 3.1: Sketch of the NTCDA molecule consisting of a naphthalene core and two anhydride groups.

The molecule contains four chemically different carbon atoms which are sp^2 hybridized and therefore lead to a planar geometry (see Fig.3.1). Additionally two different oxygen atoms the bridging and terminal oxygen, are found forming the anhydride groups. The long (anhydride-anhydride) axis has a length of 9.5 Å and the perpendicular one is 9.1 Å using van-der-Waals atomic radii.

In the following a short summary of the known relevant results of NTCDA thin films will be given, where most of them origin from our group. First,

the molecular crystal will be introduced followed by results for thick films and monolayer structures.

The molecule has 24 atoms leading to $3N - 6 = 66$ fundamental vibrations. With the following symmetry elements the symmetry group of the molecule is found.

- twofold rotation axis along the molecular main axis (one perpendicular and two in the molecular plane)
- two vertical mirror planes along the molecule axis
- a horizontal mirror plane
- an inversion center in the *middle* of the molecule

Therefore the molecule belongs to the D_{2h} symmetry group. This is a centrosymmetric symmetry group leading to a certain selection rule, i.e. vibrations are either infrared or raman active. The according symmetry races for the D_{2h} point group are listed in Table 2.2 where only vibrations with B_u -symmetry are infrared active.

If NTCDA is adsorbed on a surface or forms a crystal the symmetry group can be reduced. The possible symmetry groups are listed in table 2.3, where the resulting symmetry races are underlined if they become infrared active.

3.1.1 NTCDA crystal

In [42] the crystal structure of NTCDA is examined (compare. Fig. 3.2). The crystal has a monoclinic unit cell (point group $P2/c$) with the unit vectors $a=7.867(2)$ Å, $b=5.305(1)$ Å, $c=12.574(2)$ Å and $\beta=72.73(2)^\circ$ with two molecules per unit cell. In direction of the b-axis the molecules are stacked with a distance of 3.52 Å between the planes and an angle of 47.9° between the normal to the molecular plane and the stacking axis b.

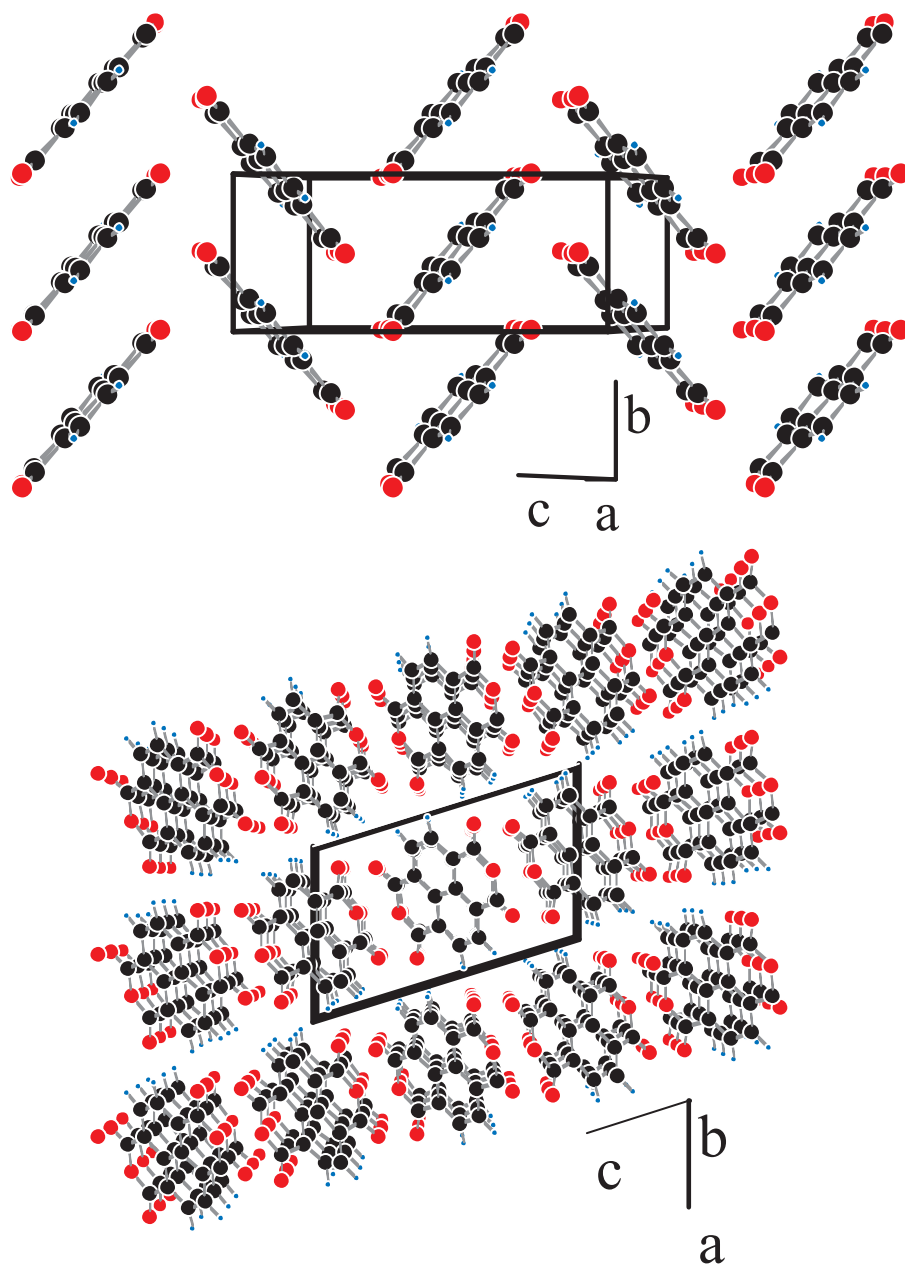


Figure 3.2: NTCDA molecular crystal viewed from $[100]$ (upper part) and $[010]$ (lower part) direction, where both surfaces are natural cleavage planes of the molecular crystal [43].

3.1.2 Monolayer structures on Ag(111)

For NTCDA/Ag(111) three different monolayer structures have been found where two of them can be distinguished straightforward with a conventional LEED optics and the third only with help of a SPA-LEED. The structures depend on the coverage of the surface [44, 45]. There is a low coverage *relaxed monolayer*, which is found at coverages below $\Theta = 0.8$. Between $\Theta = 0.8 - 0.9$ an uniaxial incommensurate structure is found, which in a conventional LEED misleadingly appears to be a superposition of a relaxed and a compressed monolayer. Above this coverage the *compressed monolayer* grows leading to the according LEED pattern.

Relaxed monolayer

The relaxed monolayer (see Fig. 3.3) has a rectangular unit cell with the vectors $|\vec{a}_1| = 11.6 \text{ \AA}$ and $|\vec{a}_2| = 15.0 \text{ \AA}$. The derived superstructure matrix is

$$M_{relax} = \begin{pmatrix} 4 & 0 \\ 3 & 6 \end{pmatrix}.$$

Therefore it is a commensurate superstructure with two molecules per unit cell, which has an area of 174.0 \AA^2 [47].

From STM data it is known that the corner molecules in the unit cell are on *on-top*-sites while in the unit cell centered molecules occupy bridging positions. Due to the symmetry of the superstructure first order diffraction spots cannot be observed [46].

Compressed monolayer

The so called compressed monolayer (see Fig. 3.4) found for higher submonolayer coverages (above 0.9 ML) is about 10 % closer packed. The according unit cell vector values are $|\vec{a}| = 16.45 \text{ \AA}$ and $|\vec{b}| = 9.57 \text{ \AA}$ with an area of 157.4 \AA^2 and an angle of 91.5° between the vectors. The matrix of the superstructure is determined to:

$$M_{comp} = \begin{pmatrix} 3.97 & 6.52 \\ -2.98 & 0.58 \end{pmatrix}.$$

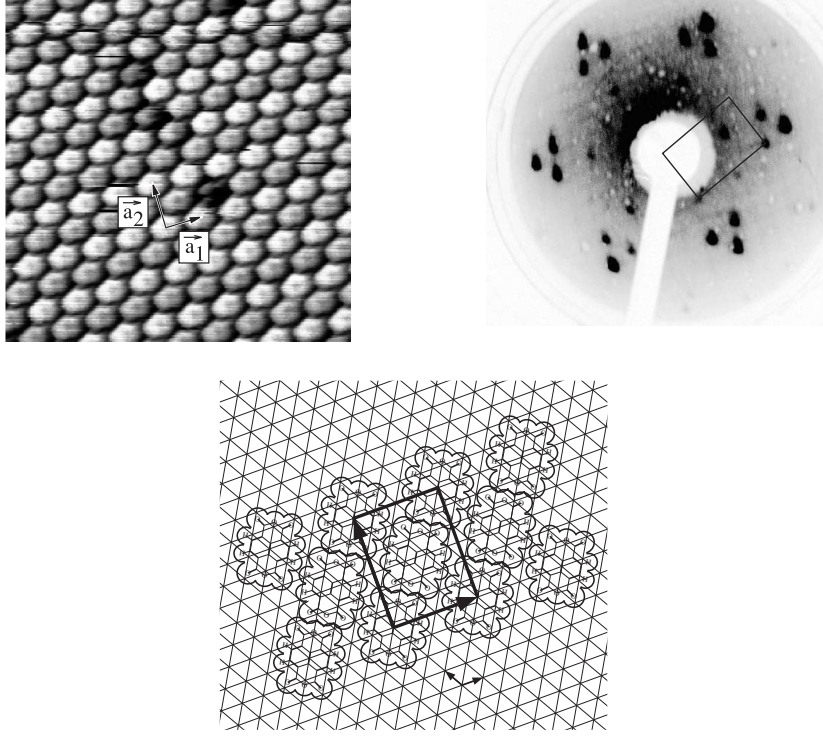


Figure 3.3: Upper left: STM image of a relaxed monolayer (size: $11 \times 11 \text{ nm}^2$) [46] is displayed along with the characteristic (upper right) LEED pattern of that structure ($E_0 = 12 \text{ eV}$) together with a real space structure model (lower picture) [47].

The floating point number entries in the matrix indicate the incommensurate nature of the superstructure.

For completeness the intermediate coverage regime superstructure is mentioned. This third superstructure is defined by the resulting matrix

$$M_{middle} = \begin{pmatrix} 3.85 & 0 \\ 3 & 6 \end{pmatrix}$$

but has no relevance for the further discussion.

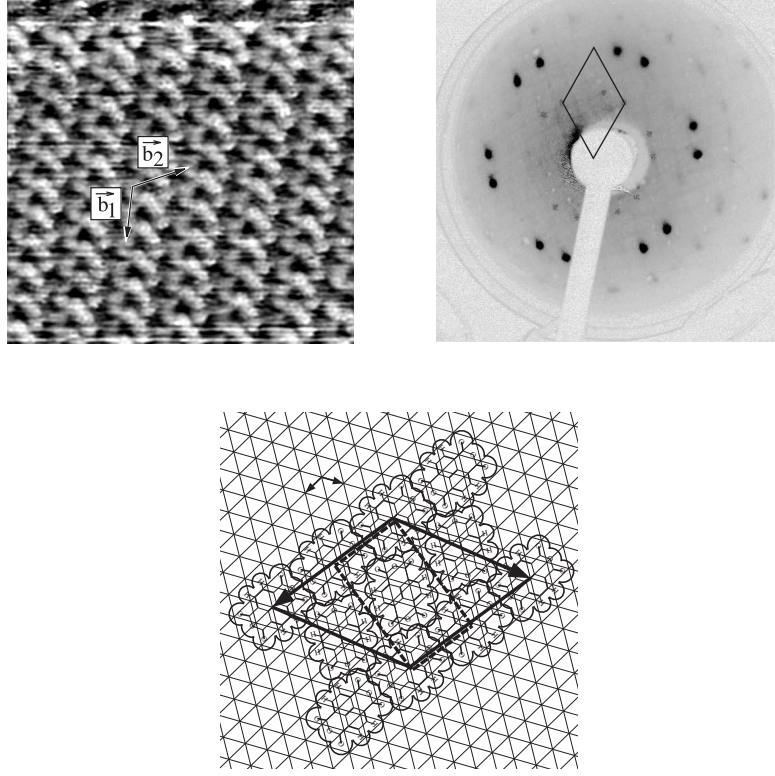


Figure 3.4: Upper left: STM image of a compressed monolayer (11×11) nm^2 [46]; upper right: LEED-pattern of a compressed monolayer ($E_0=12$ eV); lower part: real space model [47].

3.1.3 NTCDA multilayers

NTCDA multilayer films on a Ag(111) substrate have been examined by means of XPS and NEXAFS spectroscopy for different preparation parameters. NEXAFS measurements lead to the conclusion that different molecular orientations can be achieved on a Ag(111) surface [35, 48].

- Evaporation of NTCDA multilayer films onto a 285 K substrate leads to a average tilt angle of $85^\circ \pm 5^\circ$ and is usually referred to as upright standing molecules.
- In [48] thick films deposited below $T < 150$ K are reported with an average tilt angle of $15^\circ \pm 5^\circ$, while in [35] this result could not be reproduced leading to a 45° tilt angle.

Overall the difference is assigned to a temperature dependent adsorption kinetics, where for the low temperature case the interaction between the layers is mediated via π -orbitals leading to almost flat lying molecules. Room temperature substrate films are interpreted as growing molecular crystal with a natural cleavage plane forming the surface. The 45° result might be either due to a mixture of upright standing and flat lying molecules as NEXAFS provides an integral information, or due to differently oriented structures depending on the specific preparation parameters. In [49] for room temperature grown films indeed two types of islands are reported.

3.2 Naphthalene

The molecule naphthalene $C_{10}H_8$, shown in Fig. 3.5 belongs to the point group D_{2h} . There are three chemically different carbon atoms in the planar molecule, which are highlighted in Fig. 3.5. Due to its small size it is a widely used model molecular system with respect to different experimental and theoretical approaches. In the scope of this work it is examined with respect to both, the intramolecular electron vibron-coupling and intermolecular coupling in thin films.

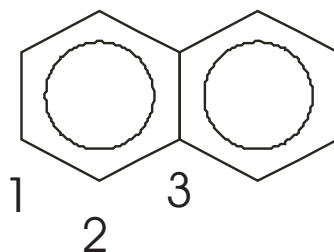


Figure 3.5: Sketch of a naphthalene molecule. Three chemically different carbon atoms are marked.

3.3 ANQ

Acenaphthenequinone (ANQ) $C_{12}O_2H_6$ is a planar molecule with C_{2v} symmetry (2-fold rotation axis and horizontal mirror plane see Fig.3.7). There are 7 chemically different sp^2 hybridized carbon atoms and two chemically identical oxygen atoms. The molecular crystal (see Fig. 3.6) has an orthorhombic structure with the basis vectors $a = 7.81 \text{ \AA}$, $b = 27.0 \text{ \AA}$ and $c =$

3.851 Å (all angles 90°). There are condensed phase NEXAFS spectra published, focusing on the vibrational fine structure at the oxygen k-edge [50]. Due to the multilayer desorption temperature of 300 K the molecule is an ideal candidate to test the new gas cell setup. Therefore photoabsorption spectra of the molecule were taken at the gas phase beamline of ELETTRA and later were compared to data achieved with the new gas cell developed during this thesis. The according results are presented in [51]. Additionally an ANQ derivate has been examined, where some hydrogen atoms have been replaced by chlorine and bromine (see. Fig. 3.7).

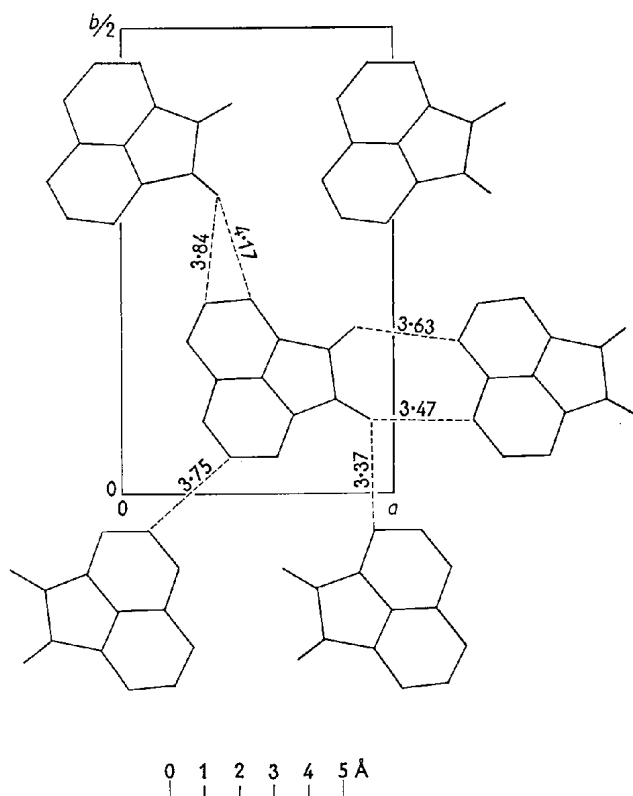


Figure 3.6: Sketch of ANQ molecular crystal shown as projection along [001] direction [52].

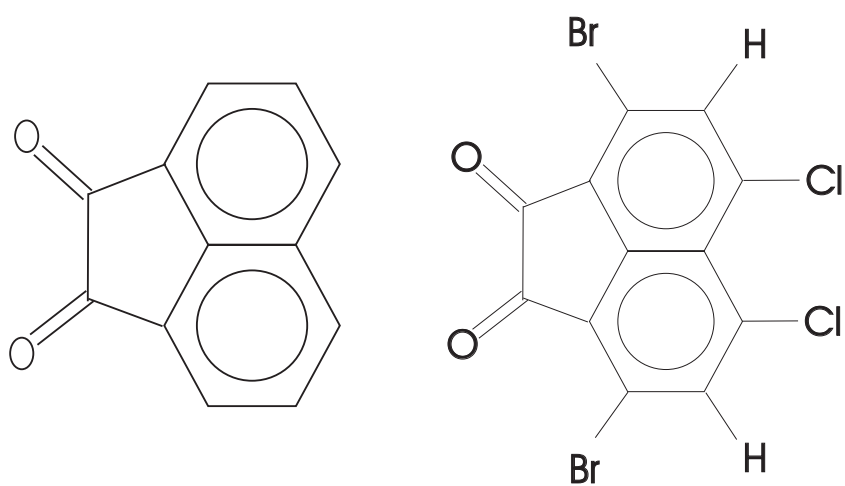


Figure 3.7: A sketch of an ANQ molecule is shown at the left side and an ANQ derivate on the right side.

Chapter 4

Experimental details

4.1 HREELS apparatus

The HREELS (**H**igh-**R**esolution-**E**lectron-**E**nergy-**L**oss-**S**pectroscopy) spectrometer is mounted in a UHV (Ultra High Vacuum) chamber and operated at a base pressure of 5×10^{-10} mbar. The samples were prepared in a preparation chamber separated from the spectrometer by a valve. For preparation and sample characterization a sputter gun, LEED optics, quadrupole mass spectrometer, evaporation cell, and a heatable /coolable manipulator were mounted.

The main experimental method of this chamber is high resolution electron energy loss spectroscopy. As magnetic fields larger than $3 \cdot 10^{-6}$ T influence the HREELS spectrometer, a μ -metal shielding is mounted around it.

The sample is heated with a tungsten filament by radiation and electron impact to a temperature up to 900 K. The sample temperature can be monitored with a Chromel/Alumel-thermocouple mounted near the Ag(111) crystal.

Sample preparation

The Ag(111) crystal was treated by standard sputtering and annealing cycles ($E_{kin} = 500 - 1000$ eV; ion current $I \approx 6 \frac{\mu A}{cm^2}$) and heating up to 850 K until a LEED pattern with sharp spots over a large energy range was observed. Another method to test the perfection of the surface is HREELS. Only on a well ordered surface with large terraces high countrates ($1 \times 10^5 c/s$) along with a low FWHM energy (2 meV) of the elastically reflected electrons can be achieved.

Film growth

Only NTCDA powder cleaned by sublimation was used for the experiments. The molecules were evaporated from a heatable cell onto the sample. Details for the used temperatures and resulting rates are given in the experimental chapters. In case of the SPA-LEED measurements unsublimated material was used which will be discussed in the according chapter 4.2

LEED

To determine the geometric structure a 4 grid LEED optics was mounted (ErLEED 1000-A from VSI), which effectively allowed suppression of inelastically scattered electrons. For documentation LEED patterns were photographed using a digital camera.

HREELS-Spectrometer

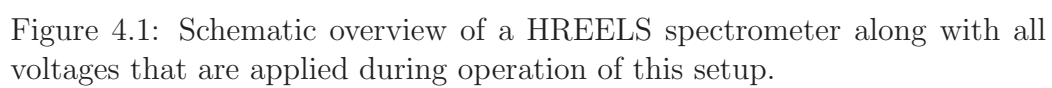
A sketch of the used HREELS spectrometer is shown in Fig.4.1 [53]. The electron source is a sharp LaB_6 -cathode emitting electrons with a full width of half maximum energy of approx. 300 meV. Via the cathode potential and the *Repeller* together with the A-lenses a point source at the entrance slit of the pre monochromator is generated.

The premonochromator is a retarding, two-dimensional focusing 151° cylindrical deflector consisting of an entrance slit EMV, inner/outer shell $VM_{in/au\beta}$, cover plates DVM_{un} and DVM_{ob} .

The main monochromator (entrance slit HM_{ein} , inner/outer shell $HM_{in/au\beta}$, cover plates DM_{un} and DM_{ob} and exit slit $HM_{au\beta}$) is a conventional 127° -cylindrical analyzer which is two dimensional focusing but not retarding.

The lenses B1 ($B1_{un}$ and $B1_{ob}$) and B2 focus the electron beam onto the sample, which is located in the main chamber mounted on a sample holder set on a potential according to the primary electron energy, in order create a potential free space for the electrons. The lenses B3 and B4 ($B4_{un}$ and $B4_{ob}$) focus the electron beam into the analyzer. During the actual measurement the corresponding B lenses should be as symmetric as possible.

The analyzer has the identical design as the main monochromator. After this analyzer, consisting of entrance slit UA_{mi} , inner/outer shell $UA_{in/au\beta}$, cover plates DA_{un} and DA_{ob} , the electrons are focused by the C- lenses into the a channeltron.



The channeltron can be used in the current mode if the spectrometer is in the straight-through mode. The voltage parameter set found for the straight through mode can be used as start parameters for the reflection mode. The electron count mode with applied high voltage is used when an electron beam reflected at a sample is examined.

All parts of the spectrometer are made of copper or of a copper beryllium alloy covered by a graphite layer in order to gain a homogeneous work function along the electron path.

4.2 SPA-LEED

The SPA-LEED experiments were performed in a separate chamber. For the present experiments the following analysis components were used: The SPA-LEED optics itself, XPS, quadrupole mass spectrometer, sputter gun, and a heatable /coolable sample holder.

While for a conventional LEED optics hemispherical grids are used to visualize the diffraction pattern, for SPA-LEED a different experimental setup is applied (see Fig.4.2), first introduced by Henzler et al. [54]. An electron beam with a small focus is emitted by the electron gun and diverted via an octupole electromagnetic field towards the surface. The backward diffracted electrons pass the octopole again and are then counted with a channeltron. The angle between the symmetry axes of the electron gun and the channeltron is fixed and has a value of 7.5° . Scanning of reciprocal space is realized by the electrostatic octopole deflection unit. Due to this setup high transfer widths combined with a high dynamic range (1×10^6 counts) can be achieved, and therefore spot profiles of single diffraction spots can be examined in detail.

The counting of electrons leads to the favorable case that within certain boundaries the electron dose per time on the surface can be reduced. Certainly this leads to a decreased signal which can be compensated by additional measuring cycles. By help of this procedure it is possible to reduce the electron induced beam damage in the film, because less energy per time is inserted and possible dissipation channels are able to dissipate the energy. In order to take possible beam damage into account data was taken in single pattern scans which were individually stored. Therefore in the case of time dependent diffraction patterns an estimate can be made about the time scale of the beam damage. The single (identical) patterns were afterwards aligned and integrated with an igor [55] script routine. This leads to a best possible

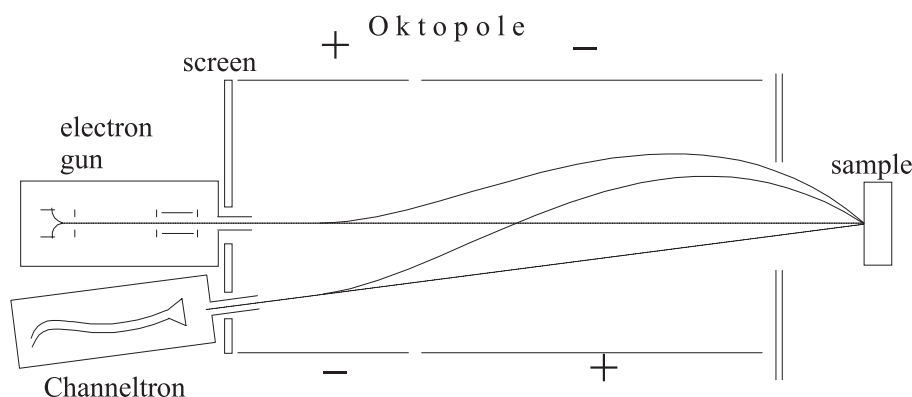


Figure 4.2: Schematic overview of a SPA-LEED setup. On the left hand side the electron gun and the detection via a channeltron are shown.

signal-to-noise ratio and resolution while contributions of beam damage can be excluded.

Sample preparation for NTCDA mono and multilayers followed the same recipe as in chapter 5.4. The sample can be kept at a constant temperature during SPA-LEED data acquisition, as heating/ measurement cycles can be chopped, excluding an influence of the electrons emitted during heating on the measured data. Intermittant heating-cooling cycles have the following advantages: A reduced temperature during data acquisition provides sharper spot profiles due to an improved signal-to-noise ratio via the influence of the Debey Waller factor. Additionally, some superstructures are only present in a certain temperature window which makes heating or cooling to a fixed temperature a mandatory subject.

In addition XPS was used to estimate the film thickness and check the substrate for contaminations before evaporation of organic molecules.

4.3 Gasphase measurements

The gas phase measurements of large organic molecules were preformed at high-brilliant third generation synchrotron sources, partially at the ELETTRA gas phase beamline and partially at the BESSY UE52/PGM beamline using a home made gas cell.

4.3.1 Gas cell

Vacuum chamber

In Fig.4.3 the experimental setup of the gas cell is shown schematically as it was used at the UE52/PGM beamline. The gas cell is mounted centered in a small 100mm "T piece" UHV chamber which is pumped using a turbomolecular pump. After bakeout a base pressure below 5×10^{-9} mbar in the chamber was reached but rises up to 10^{-6} mbar during measurement which reflects the high partial organic gas pressure within the heated cell. Three CF40 feedthroughs are used for the heating power supply and the signal lines. Between the gas cell chamber and the beamline an additional, roughly 50 cm CF40 "T piece" is mounted and pumped separately. It fulfills the purpose of a differential pumping stage with 5 mm diameter apertures mounted on both ends. This is mandatory to avoid organic contamination of the Scienta chamber, where the synchrotron beam is fed through, or of the beamline itself during operation with the pressure in the gas cell chamber as mentioned above. Actually only moderate pressure rises have been noted in the Scienta chamber while heating the cell.

The setup is mounted on a rack that provides full access to all degrees of freedom needed to align the cell with the synchrotron beam. To possibly operate the endstation at different beamlines and for fine adjustment the height can be set by 4 screws attached to the base of the rack. For horizontal adjustment at front and back end a gearing is attached between the chamber and the rack. For alignment it is advisable to start with a total station for determination of proper position of the front and rear window of the cell mounted in the chamber. Fine tuning was done with the synchrotron beam made visible by ZnS covering the frame of the front window and observable through a CF16 viewport facing this window. The signal behind the cell is optimized by the photocurrent measured between an isolated metal foil and ground located behind the rear window.

The Cell

In order to perform the experiment the gas cell is heated above the sublimation temperature of the organic molecules under investigation to achieve a high partial pressure of molecules. The molecules in the gas phase are separated from the outside of the cell by thin aluminium foil windows (0.1-0.2 μm). A X-Ray beam is used to ionize the molecules which are separated from the electrons by an electric field and then detected on metal plates

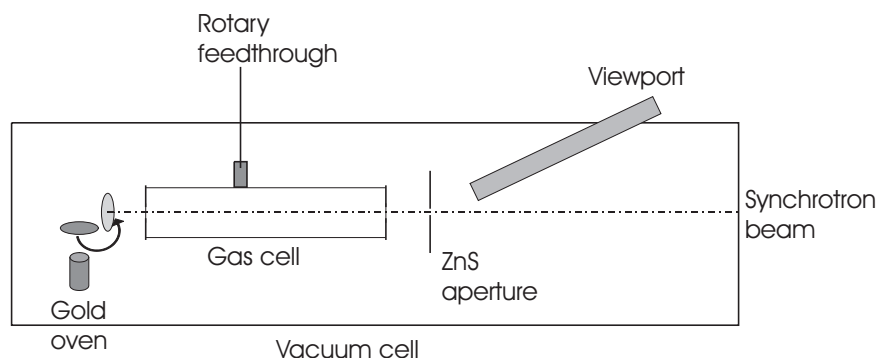


Figure 4.3: Schematic overview of the gas cell vacuum chamber. The synchrotron light enters from the right hand side and can be aligned with the cell by help of the ZnS aperture. A valve is mounted at the gas cell. It can be operated by a rotary feedthrough from outside the vacuum.

leading to a current in the range of picoampere. Measuring the ion/electron current with respect to the energy of the incident photon beam leads to the photoabsorption spectrum.

A detailed drawing of the gas cell is shown in Fig.4.4. It consists of a 20 cm tube, manufactured of V2A stainless steel with an outer diameter of 3 cm. The cell is heated by two core heating elements purchased from the company Thermocoax [56]. Sealed and highly bendable they are wound around the cell fixed with half rings (see Fig.4.4 g), to assure a uniform temperature and avoid cold spots at the closing (e) and current feedthrough (c). With a heating power of 24W for each of the heating elements a temperature of 600K can be achieved. In order to avoid a possible effect of magnetic fields on the experimental result the wire and return wire are mounted parallel around the cell.

First results were achieved with home-made Al windows. The windows were built from purchased [57] Al foils ranging from 0.1 to 0.2 μm thickness. The window Al foil is mounted in a sandwich like structure between two perforated conventional Al foil frames with a copper window plate (see Fig. 4.4.II). However, the price of the raw foil went up strongly accompanied with an unreliable delivery period. Hence completely framed windows were purchased

from Lebow Company [58]. In both cases, windows were stored mounted in rubber tubes for mechanical shock absorbance during transportation and were ideally kept under vacuum to avoid ageing of the thin foil.

Special care was taken to ensure that the aluminium windows (Fig. 4.4 a, b) were heated above the cell temperature, in order to prevent the organic material from being adsorbed on the foil. Thus absorption of beam intensity and therefore an influence upon the measured signal is avoided. Unfortunately such an error cannot be taken into account by normalization, as the pure absorption of the windows in a heated gas cell cannot be measured. Therefore the heater wire is spiral bended around the windows to assure a sufficiently high temperature of the Al windows.

On the inner side two 20x1.5 cm metal electrodes (Fig. 4.4 d) are mounted with a distance of 1.5 cm to collect electrons and ions, with the signal conducted to the outside by ceramic feedthroughs commercially available from FRIATEC AG [59]. Due to the organic contamination it is mandatory to have them demountable after the experiment. The conductivity of the ceramics strongly depends on its temperature, therefore after reaching the desired measuring temperature it is advisable to wait for thermal equilibrium of the whole chamber.

Ions and electrons are separated by a potential applied between the electrodes using a battery box for stability reasons. Best results were achieved by applying a positive voltage to one electrode collecting the total ion current to ground on the other. On the upper part of the cell a valve is mounted which can be operated via a rotary feedthrough from outside the vacuum chamber. To limit mechanical stress on the Al windows when evacuating the chamber it is pumped slowly with open valve. During bakeout it is kept open to allow possible contaminations a path out of the cell, while during operation it is closed to prevent organic contamination of the vacuum chamber.

4.3.2 Beamlines

ELETTRA

The X-Ray beam at the Gasphase Photoemission Beamline at ELETTRA is generated by an undulator. Via two mirrors the beam is fed through a variable entrance slit into the monochromator. This consists of two mirrors and a grating. For high resolution measurements only the grating is moved while the mirrors are fixed (*fixed mirror mode*), which is sufficient, concerning the resolution, as long as the measured energy window is within 2% of the

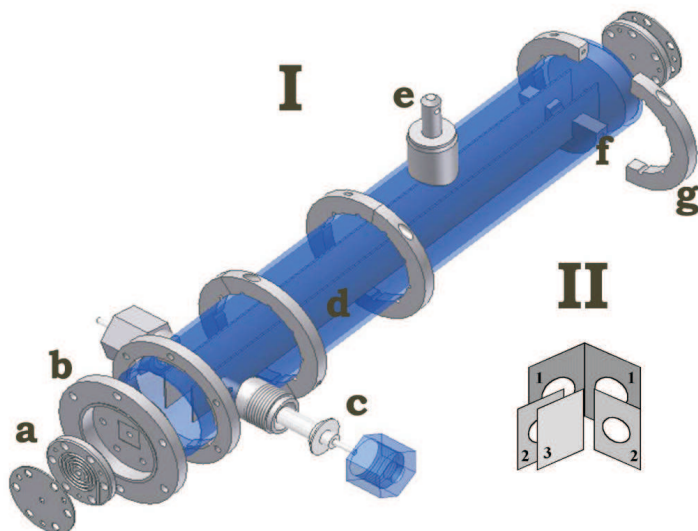


Figure 4.4: Schematic overview of the gas cell, where in I all important parts are labelled (a-g) and in II the idea behind the sandwich Al windows (mounted in (b)) is shown.

photon energy. The undulator gap is also fixed during the measurement which leads to a poor signal to noise ratio for large energy scans as the intensity drastically decreases when the energy is too far off the undulator harmonics. The beamline is characterized by a resolving power of 10.000 at 540 eV, leading to 54 meV at the oxygen K edge and 12.000 at 285 eV leading to 24 meV at the carbon K edge.

The measurements were done in a high vacuum chamber at a base pressure of 2×10^{-6} mbar. The sample molecules were evaporated from an oven onto a liquid nitrogen cooled shield, to avoid chamber contamination. As the ionization path is rather small, because the synchrotron beam is almost perpendicular to the organic evaporator beam a channeltron is necessary to collect the data. On the other hand due to the small absorption of the synchrotron beam, I_0 can be measured on a photo diode behind the experiment. Additionally, absorption of gases, like O_2 , CO or CO_2 , can be measured in order to calibrate the energy scale.

BESSY

The undulator UE52/PGM at BESSY II in Berlin-Adlershof is an APPLE II type with 79 52 mm periods, which provides both elliptically and linearly polarized light with a tunable polarization plane. The beamline uses the

electron beam in the undulator as entrance slit. After a cylindrical mirror the beam is vertically focused into the monochromator, which consists of a plane mirror and a grating with 1200 lines /mm. Depending on the needed energy range the according diffraction order is focused on the exit slit by two mirrors (a cylindrical vertically focusing and a spherical horizontally focusing mirror). The exit slit can be set to 10, 30, 50, 100, and 500 μm . For energy variation, mirror, grid, and undulator gap are moved simultaneously. This leads to a high flux combined with high resolution over a large energy range. The resolution of the beamline is determined by the exit slit and the c_{ff} value, which is a measure for the position of the focal point. Generally a high c_{ff} leads to high resolution with low intensity. The resolving power measured at the N-K-edge with an exit slit of 10 μm and a c_{ff} value of 10 is approximately 10.000 leading to an estimate of 25 meV and 56 meV at C and O-k-edge, respectively. The usually used endstation, the Scienta chamber is separated into experimental and preparation chamber and is bypassed via the experimental chamber to extend the beamline into the gas cell chamber.

Chapter 5

Results and Discussion

This chapter starts with the NEXAFS data from intramolecular interaction in naphthalene followed by a discussion of the effects of intermolecular interaction of condensed naphthalene. The second example for intra and intermolecular interaction is the molecule ANQ.

In the second part, results ranging from monolayer to multilayer films of the NTCDA molecules measured with HREELS and SPA-LEED are presented.

5.1 Naphthalene gas phase

The data and interpretation presented in this chapter are published in Chemical Physics Letters [60] under the title: "Isotope Effects in High-Resolution NEXAFS Spectra of Naphthalene".

Introduction and Motivation

High-resolution near-edge x-ray absorption fine structure (NEXAFS) results of hydrogenated and fully deuterated naphthalene (called h8 and d8 in the further discussion) in the gas phase are presented. The rich fine structure in the C K-edge spectra is identified as coupling of the electronic transitions to various vibronic excitations as supported by ab-initio calculations. The differences in the spectroscopic signatures of the two isotopes strongly indicate significant contributions of C-H (C-D) and C-C vibrational modes. This is

corroborated by a comparison with the similar spectra of (deuterated) benzene, which allows the identification of at least two C-H (C-D) modes and one C-C mode.

Detailed investigations of the electronic properties of large organic molecules have become a major issue in fundamental research. The sophisticated experimental techniques and theoretical concepts available nowadays allow a comprehensive understanding of molecular properties and intramolecular effects. A major source of information are the various electron spectroscopic techniques which can also be utilized to investigate the intermolecular interactions in the solid state and molecular bonding to a different material, e.g. a substrate. However, in these cases it is extremely useful to first understand the molecular electronic structure of the isolated (gas phase) molecule before tackling the more complicated solid state.

In particular, Near-Edge X-ray Absorption Fine Structure (NEXAFS) spectroscopy has demonstrated enormous power for investigating organic substances due to its high chemical sensitivity [34]. This sensitivity arises from the ability of the technique to resolve the influences of the chemical environment on the electronic initial and final state orbitals of the probed system. In addition, NEXAFS supplies interesting information on the reorganization of the electronic system upon core hole creation, which leads to the selective excitation of vibronic modes due to local changes in the molecular orbital system. The electronic reorganization is particularly efficient in conjugated molecules and therefore needs to be properly taken into account in the interpretation of NEXAFS spectra.

Vibronic features in NEXAFS are observed if the electronic excitation is accompanied by the excitation of vibrational modes ν' , such as the C 1s ($\nu=0$) $\rightarrow \pi^*$ ($\nu'=0,1,2,3,\dots$) transition. Since the energy separation between vibrational modes (typically < 350 meV) is small on the energy scale of NEXAFS transitions, vibronic features are most clearly resolved when they accompany narrow electronic transitions. As the intrinsic width is determined by the life time of the core excited state (~ 80 meV for C 1s excitations), there is a lower limit on the vibrational energies that can be resolved by conventional NEXAFS spectroscopy. Thus, for small molecules, several examples of efficient coupling of electronic to vibronic excitations were demonstrated. The data evaluation can be based on a Franck-Condon analysis [61–63]. In favorable cases one may even be able to distinguish the coupling of different vibronic modes [64].

However, for larger molecules the situation is more complicated since various electronic transitions are possible, and these may have a complex coupling to numerous normal modes (44 for the present molecule) which are spread over

an energy range from about 20 to 400 meV. This may lead to a large number of peaks and shoulders that make an unambiguous interpretation of the NEXAFS fine structure very difficult. Thus, there are only few examples of larger molecules where vibronic fine structures were detected in the condensed phase [50, 65, 66]. It is remarkable that in most of these cases, the electronic transition couples predominantly to one vibronic mode. For instance, for the naphthalene derivate NTDCa, predominantly the C=O stretching mode couples to the 1s excitation of the anhydride carbon atom [66]. The vibronic coupling within the styrene subunit of condensed polystyrene [65] was derived from the observation of isotope effects similar to those of benzene [67].

For a complete understanding of complex processes, a full theoretical description is required. Small, highly symmetrical aromatic molecules can be regarded as ideal model systems to investigate the intramolecular interactions in delocalized electronic systems [68]. After benzene [67, 69–71], naphthalene is next in the series of homocyclic ring systems which have been studied extensively by both experimental [71, 72] and theoretical methods [71, 73] in the gas phase as well as in the solid state. Compared to benzene, the larger naphthalene consists of three chemically different carbon atoms, which can be distinguished in NEXAFS from their C 1s \rightarrow π^* -resonances (see present results and, e.g., Ref. [69]).

As part of a systematic high-resolution NEXAFS study of various polyacenes, the C 1s NEXAFS spectra of non-deuterated and perdeuterated naphthalene in the gas phase ($C_{10}H_8$ and $C_{10}D_8$; in the following denoted as h8- and d8-naphthalene, respectively) were investigated. The present chapter focuses on the evaluation of the NEXAFS fine structure and the experimental assignment of the vibronic features in the π^* -resonances. In particular, C-H modes which should not play a significant role according to a recent theoretical investigation [71] were observed. This finding leads to the conclusion that the calculations underestimate the vibronic coupling to hydrogen atoms [71].

Similar vibronic fine structures in the spectra of condensed h8- and d8-naphthalene films were observed, which gives additional information on the intermolecular interactions in molecular condensates. This will be discussed in detail in Chapter 5.2.

NEXAFS experiments on h8- and d8-naphthalene were performed at the Gas Phase Photoemission Beamline at ELETTRA [74]. The photon flux was about 10^{10} photons/s \times 100 mA. The resolving power $E/\Delta E$ was better than 12000 at the C K-edge leading to a spectral resolution of better than 25 meV at 300 eV, thus offering the required resolution to resolve vibrational fine structures in the range of C-H- or C-C-stretching modes. The absorption

signal was detected using two channeltrons counting electrons and ions, respectively, in the total yield mode. A fixed mirror scan was performed with 5 meV steps in order to take advantage of the full monochromator resolution. The photon energy scale was calibrated with respect to the CO_2 π^* -resonance at 292.74 eV [75]. The measured NEXAFS spectra were normalized to the photon flux curve recorded with a Si photodiode directly behind the gas cell. Commercial h8-naphthalene and d8-naphthalene of high purity (99.9 %) purchased from Aldrich were directly used without further purification.

The interpretation of the electronic transitions is based on ab-initio calculations using the GSCF3 program developed by Kosugi [76,77]. The basis set for the calculations was (621/41) for C, (41) for H, and (411121/411) for the C atom with the core hole. An additional polarization function was placed at the atom with the core hole. The ground state geometries were derived from an ab-initio geometry optimisation at the STO-3G level using GAUSSIAN 98. The program SIMILE was used to generate the NEXAFS spectra by convoluting the GSCF3-results with Gaussian functions of 0.3 eV FWHM for orbitals of eigenvalue $\epsilon < 0$ and of 1.2 eV FWHM for $0 < \epsilon$.

Experimental Results

Fig. 5.1 compares the normalized gas phase C K-NEXAFS spectrum of h8-naphthalene (top spectrum) with theoretical ab-initio results (bottom spectrum; note that the “stretching” of the calculated energy scale is well known for this and similar ab-initio methods and originates from an overscreening of the core hole in these calculations). The experimental data show four groups of π^* -resonances (denoted A, B, C, D) with clearly resolved fine structures. According to the GSCF3-calculations (Fig.5.1 bottom), which only consider pure electronic transitions, the resonances in Regime A are due to two transitions from the C1 and C2 atoms into the lowest unoccupied molecular orbital (LUMO), which is in agreement with previous studies [72,73,78]. The $\text{C3} \rightarrow \text{LUMO}$ excitation is symmetry forbidden and therefore not observed.

Resonances in Regime B stem from contributions of the C3 (bridging carbon) and C1 atoms into the LUMO+1. The resonances of Group C can be attributed mainly to excitations from C2 and C3 1s states into the LUMO+2, and two transitions with s-symmetry, $\text{C1} \rightarrow \text{LUMO}+4$ and $\text{C2} \rightarrow \text{LUMO}+5$. This interpretation for the electronic transitions is analogous to the previously mentioned theoretical studies for naphthalene [71,73] and hence will not be considered further. The more interesting questions concern the manifold fine structures besides these electronic transitions. Although the core excitation in the NEXAFS process is localized at a particular atom, the excitation

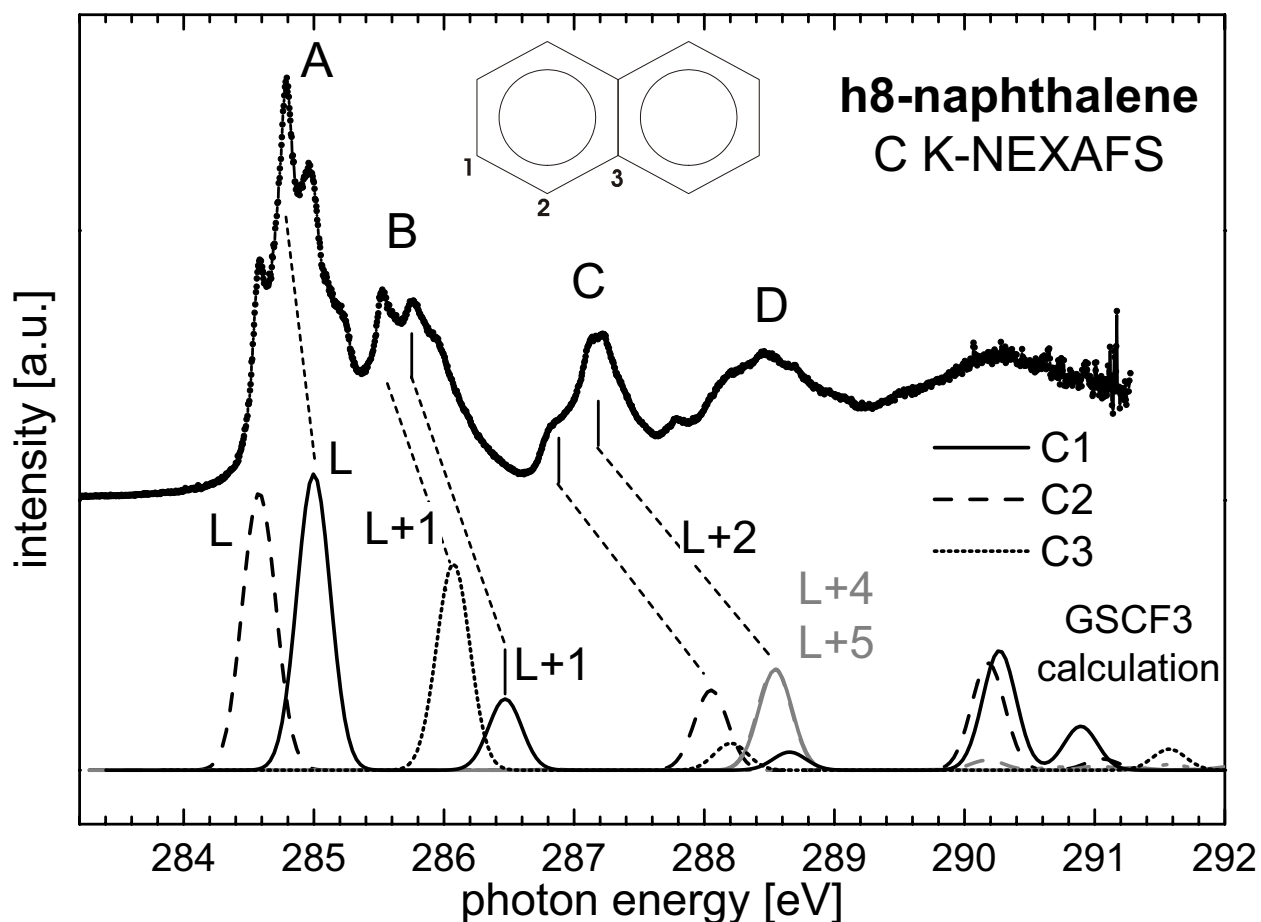


Figure 5.1: NEXAFS spectrum of gas phase h8-naphthalene recorded in the total ion yield mode. Four groups of π^* -resonances (denoted A - D) are compared to ab-initio Hartree-Fock calculations (lower spectrum) [76], [79]. The calculated excitations from the three inequivalent carbon atoms (C1 - C3; see inset) into the unoccupied orbitals LUMO, LUMO+1, LUMO+2, and LUMO+3 are denoted. Transitions with p-/s-symmetry are plotted in black/grey, respectively. The energy scale of the calculated spectrum is shifted by -1.5 eV to align the first transitions. The stretching of the calculated energy scale is a well known effect (see text). The noise of the experimental data at higher photon energies results from lower count rates in the fixed mirror scan mode.

may couple to vibronic modes far from the excited atom, as e.g. suggested for ANQ [50]. Thus, a manifold of different modes has to be considered. Modified DFT calculations in Ref. [71], which explicitly include the coupling to vibrational modes, lead to the conclusion that various C-C modes couple significantly to the different C 1s excitations, and that the Franck-Condon factors for vibronic states $\nu' > 2$ are negligible for all but one mode.

A relatively complex coupling to vibronic modes was also found in our analysis. Fitting the experimental data with Franck-Condon like vibronic progressions was not successful if using a too small number of free fit parameters. Thus, significant contributions of at least three vibronic modes to both electronic transitions for the resonances in regime A had to be included.

To further understand and assign these different vibronic excitations C K-NEXAFS spectra of h8- and d8-naphthalene were recorded, which are compared in Fig.5.2. Distinct differences and differential shifts of fine structure features in particular in regime A are observed: in the energy range of the four prominent peaks in h8-naphthalene (bottom) 5 resonances in the d8-naphthalene spectrum (top) are detected. The shifts are marked by guide lines in the inset of Fig.5.2. Since the fine structures shift to smaller energies they can directly be assigned to isotope effects arising from reduced vibrational frequencies in the deuterated molecule. Thus the first major result of the present paper is that the fine structures of feature A are due to the coupling of vibrations with predominantly C-H and C-D character, respectively. This experimental finding is in contradiction to previous calculations [71].

Similar isotope effects as in the present study have been observed in the C 1s photoabsorption spectra of benzene [67]. Since furthermore the C1 and C2 atoms of naphthalene (contributing to structures A) are relatively similar to the (six equivalent) carbon atoms in benzene, it is straightforward to analyze the vibronic fine structure of the C1 and C2 contributions to the h8- and d8-naphthalene spectra with the help of NEXAFS spectra recorded for benzene and perdeuterated benzene. Thus a weighted sum of two benzene spectra (digitized from Ref. [71]) has been fitted to the resonances in regime A in our naphthalene spectrum, which are, according to the above discussion, due to electronic transitions from the C1 and C2 atoms into the LUMO. The required energy shift of about 0.2 eV between the two benzene spectra (see Fig.5.3) arises from the slightly different energies of the $C1 \rightarrow LUMO$ and $C2 \rightarrow LUMO$ transitions. The fit results are summarized in Table 5.1.

Fig.5.3 shows the result of the analysis of the two substances. For both naphthalene species the spectra are well reproduced by the two energetically shifted benzene spectra. The fits resulted in very clear minima of the χ^2 function as shown by the two insets of Fig.5.3. This and the rather smooth

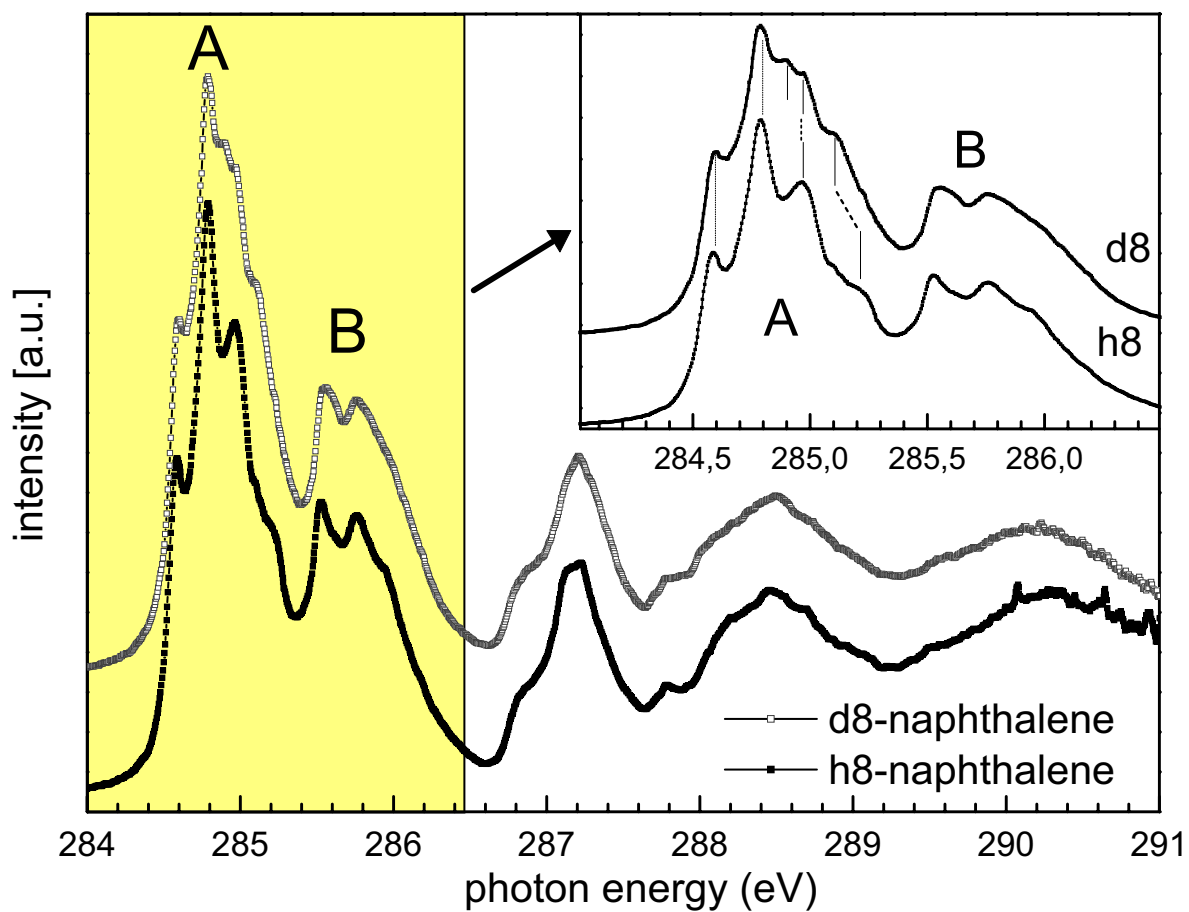


Figure 5.2: Comparison of the high-resolution NEXAFS spectra for d8- (top) and h8-naphthalene (bottom). The step width between data points was set to 5 meV. The inset displays the energetic shifts (isotope effects) of the resonances in the shaded area on an expanded scale.

difference curves (residua; see bottom) allow to have confidence in this approach. The energy shifts between the adiabatic transitions compare very well to those of Ref. [71] (ΔE_{C1-C2} : 200 meV). The very similar ΔE_{C1-C2} values for the two naphthalene species indicate that no significant changes of the atomic distances and hence of the electronic transitions occur upon deuteration (see Table 5.1). The values for the relative intensities C1/C2 also compare well with the intensities derived from our GSFC3-calculations (see Fig.5.1, bottom).

The predominant vibronic features in the benzene and perdeuterated benzene NEXAFS spectra are denoted in Fig.5.3 according to the analysis of Ma et al. [67]: peak α is assigned to a C-H (C-D) bending mode and clearly shifts towards lower energy upon deuteration (180 vs. 105 meV). An analogous shift from 420 meV to 310 meV is observed for peak γ and therefore suggests the classification as a C-H (C-D) stretching mode. In contrast, peak β is not affected by the deuteration (180 vs. 180 meV) and hence can be assigned to a C-C stretching mode [67]. Peaks 0-0 refer to the adiabatic transitions.

On the basis of the detailed understanding of the benzene spectra and the good result of the benzene-fit approach, which reproduces all predominant features of the π^* -resonances A of the h8- and d8-naphthalene data very well, the vibronic contributions to these resonances can be assigned. Thus, peak 1 in the h8- and d8-naphthalene data is due to the adiabatic C1s \rightarrow LUMO transition at the C2 carbon. For both molecules, peak 2 is mainly generated by the adiabatic C1 \rightarrow LUMO transition plus a vibronic loss of the C2 \rightarrow LUMO transition involving the excitation of one C-C mode (denominated β in the benzene spectra). Peak 3 for h8-naphthalene has to be attributed to the superposition of peaks α and β of the C1 transition and peak γ of the C2 transition. This superposition is corroborated by the asymmetric line shape and the relatively large width of peak 3 (as compared to peaks 1 and 2). Peak 4 is dominated by the C1- γ contribution.

Upon deuteration, the spectral signature is strongly changed in the region of peak 3. For d8-naphthalene (at least) two shoulders, denominated 3a and 3b in Fig.5.3 can be observed. Our analysis suggests the assignment of shoulder 3a to the peaks C1- α and C2- γ and shoulder 3b to peak C1- β . Peak 4 is again dominated by the C1- γ contribution as for h8-naphthalene; the shift of peak 4 upon deuteration is well-reproduced.

In summary, the deuteration effect in the naphthalene spectra that can most clearly be observed by the shift and splitting of peak 3 and the shift of peak 4, has to be explained by the reduction of the CH (CD) vibronic energies and the resulting shift of the CH (CD) derived peaks α and γ . It is emphasized that the shift of the C-H(C-D)-derived peak α is also clearly visible as a

“filling” of the dip between peaks 1 and 2 upon deuteration. Note that the slight mismatch of the fits around peak 3 can be explained by differences in the (and the contribution of additional) C-C modes, that must influence peak β and the described features. Also, the mismatch of the fits around peak 4, that assume a sharper shoulder in this region, can be attributed to additional ring vibronic modes in the larger naphthalene molecule, that smear out the structures on the high energy tail of structure A.

Discussion and Conclusions

The isotope effect upon deuteration of naphthalene is of course well-known from ground state vibrational spectroscopies. For instance, IR spectra show significant differences for C-H (C-D) related vibrations between h8- and d8-naphthalene. For non-deuterated naphthalene C-H stretching modes have frequencies in the $2900 - 3100\text{ cm}^{-1}$ regime, and C-H bending modes can be found between $800 - 1000\text{ cm}^{-1}$. These modes shift to about 2300 cm^{-1} and $680 - 800\text{ cm}^{-1}$, respectively, for perdeuterated naphthalene [80]. The influence of the deuteration is reflected by only minor energetic shifts for C-C-vibrations (e.g., C-C stretching mode: 1578 cm^{-1} in h8-naphthalene vs. 1548 cm^{-1} in d8-naphthalene). It is emphasized, that the ground state C-H (C-D) stretching and bending modes in naphthalene are very similar to those observed in benzene [16] which supports the fit approach of Fig. 5.6.

Furthermore, the fact that benzene fits clearly and consistently reproduces all fine structure signatures of the $\text{C1/C2 } 1s \rightarrow \text{LUMO}$ -transitions of h8- and d8-naphthalene imply very similar Franck-Condon parameters for the respective vibrational bands and also allow to identify contributions of C-H(C-D) stretching and bending modes in naphthalene spectra. Consequently, the most prominent spectral features of naphthalene cannot solely be explained by the excitation of C-C modes. Note that further a similar vibronic coupling has been found for biphenyl, where theoretical and experimental investigations suggest that C-H modes strongly contribute to the vibronic fine structure in the high-resolution NEXAFS spectra [81].

In conclusion, the experimental findings show that the theoretical calculations of naphthalene should be refined such that the C-H/C-D modes are properly taken into account. This is an important issue since only then a complete understanding of the vibronic fine structure of many other aromatic compounds would become possible.

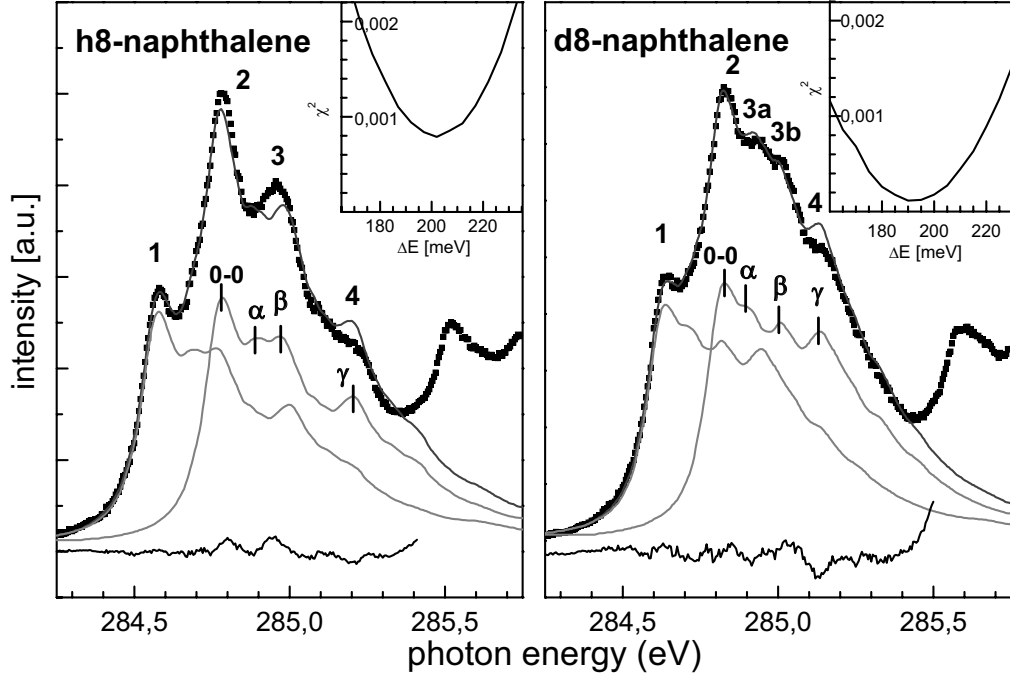


Figure 5.3: Fit of the NEXAFS spectra of non-deuterated and perdeuterated benzene to the first two resonances in the h8- (left) and d8-naphthalene (right) C K-NEXAFS spectra. The benzene spectra were digitized from Ref. [66]. The shift of the benzene spectra corresponds to the energy shift between the C1 and C2 \rightarrow LUMO transitions (fit results see table 5.1). The predominant vibronic features of the benzene and deuterated benzene spectra are denominated α , β , γ and are discussed in the text. The insets show the Chi-square values for different relative energy positions of the two benzene spectra.

Table 5.1: Resulting fit parameters for the analysis of the naphthalene spectra using literature data for benzene and perdeuterated benzene [71]. ΔE_{C1-C2} denotes the energetic shifts between the two benzene spectra, corresponding to the energy difference between the C1 and C2 $1s \rightarrow$ LUMO transitions; their relative intensities are a measure of their relative oscillator strengths.

	ΔE_{C1-C2} (meV)	Relative intensity C1/C2
h8-naphthalene	200(5)	0.942
d8-naphthalene	195(5)	0.914

5.2 Solid state effects in high-resolution NEXAFS spectra of naphthalene

In this chapter, high resolution NEXAFS data of hydrogenated and deuterated naphthalene in the gas and condensed phase will be presented. The detailed comparison allows the identification of subtle differences in the spectra upon condensation, which can be associated with the interaction between the molecules. The observed energy shifts will be assigned to the π - π -interaction and the delocalization of the respective final state orbitals. Moreover, a quenching of σ^* excitation is observed in the condensed phase which is explained by the strong Rydberg character of the respective resonance.

In recent years, much effort has been devoted to the examination of thin films of condensed organic molecules [82–85] due to their potential in complementing inorganic materials in various electronic and opto-electronic devices, such as organic LEDs, thin film transistors, or solar cells. An optimization and tailoring of the device characteristics requires a comprehensive understanding of the fundamental properties such as, e.g., the charge carrier transport within the active material and at its interfaces as well as its interplay with structural and morphological properties. In this respect, a detailed knowledge of the interaction mechanisms involved between the organic molecules and between the molecules and the substrate is highly desirable. The commonly applied picture of relatively weak Van-der-Waals [83] and electrostatic intermolecular interaction can hardly explain recent experimental observations such as relatively strong differential peak shifts of up to 1 eV in various electron spectroscopies. Such relative bonding shifts are far beyond a dispersion of the molecular valence levels in the order of 100–200 meV for some π -conjugated compounds [86, 87]. Especially the bonding shifts indicate a stronger interaction between the molecules. But also the band dispersion indicates a delocalization of the respective electronic wave functions, thus possibly enabling a coherent band-like charge transport which can be related to a higher mobility than the commonly expected hopping mechanism. The fast delocalization of charge within some aromatic aggregates is also indicated by the very recent observation of very small exciton binding energies [88] and of missing surface core level shifts showing that the charge polarization model is not applicable [89].

Near Edge X-Ray Absorption Fine Structure (NEXAFS) spectroscopy will be used again here due to its chemical selectivity [34]. Small spectral modifications indicate a marked influence of the intermolecular coupling on the molecular potential curves [61, 62, 64, 65, 67, 68] thus indicating a significant intermolecular overlap of the respective molecular states.

A straightforward approach to directly probe intermolecular interaction is to compare the data acquired for a free molecule, i.e., in the gas phase, with its condensed counterpart. In practice, however, this experiment requires very stable conditions and very high spectral resolution since the effects, if existent, are expected to be relatively small.

Naphthalene seems to be an ideal model system since it presents a sufficiently large delocalized electronic system with no other chemical subunits which may affect the molecular interactions by a significant electrostatic contribution. The gas and condensed phase data will be assigned and interpreted with the help of theoretical calculations. Particular focus will be placed on the influence of the intermolecular interaction on the molecular electronic structure, which now can be analyzed in quite some detail due to superior spectral resolution. Naphthalene has been the subject of various studies [90,91] including some that contain medium resolution comparisons of the gas and condensed phase [92], which are consistent with our results.

Experimental

The condensed phase data were recorded at the UE52/PGM beamline at BESSY II with an energy resolution of better than 25 meV at a photon energy of 300 eV [50]. Energy calibration and intensity normalization were performed carefully according to Ref. [93]. Gas phase NEXAFS experiments were performed at the Gas Phase Photoemission Beamline at ELETTRA [74,94]. For further experimental details, see Chapter 5.1.

To allow a detailed comparison, particular effort has been devoted to an equivalent energy calibration, since the experiments in the gas and condensed phases use different procedures (a σ^* -resonance in the CO₂-NEXAFS spectrum and the Ag-Fermi edge in a photoemission (PES) spectrum, respectively). In order to be independent of the differing values for the CO₂ π^* -resonance in the literature, this value was determined with a gas cell at the BESSY UE52-PGM experimental station and calibrated with the Ag Fermi edge in the PES spectrum in analogy to the thin film spectra.

Results and Discussion

Fig. 5.4 compares the C K-edge NEXAFS data of gas phase naphthalene (h8, spectrum (a)) and deuterated naphthalene (d8, spectrum (b)) to the molecules in the condensed phase (spectra (c) and (d), respectively). The dominating features are labelled A, B, C, and D. For better comparison

the solid state spectra were shifted by +300 meV in order to align the first resonances (Res. A) with their gas phase counter parts at 284.8 eV.

In the previous chapter already the C K-NEXAFS spectra of h8 and d8 in the gas phase were reported and the dominating spectral features were assigned to the resonant excitation of C 1s electrons into various unoccupied π^* - and σ^* orbitals [60]. The analysis of the spectra was based on results from ab-initio calculations (employing the GSCF3 code [76] in accordance with assignments given in the literature [63,70]. As was discussed previously, the spectral fine structure can be unambiguously interpreted as coupling of electronic transitions to vibronic modes.

At first glance the gas to the solid phase spectra appear very similar, besides a striking deviation in the regime of feature C. In the following the most prominent regimes A – D and their sensitivity to matrix effects will be discussed in detail.

Resonance A: Resonance A consists of two contributions, which are attributed to 1s electron excitations at the C1 and C2 carbon atoms (see inset in Fig.5.4) into the lowest unoccupied molecular orbital (LUMO). The clearly resolved fine structure of this resonance is due to the excitation of molecular vibrations, as discussed in chapter 5.1 and [71]. If the h8 spectra are compared in gas (spectrum (a)) and condensed phase (spectrum (c)) the vibronic signature turns out to be unchanged since no peak shifts occur. However, the resolution is slightly better in the case of the gas phase data. This can be seen much clearer in Fig.5.5, which compares resonances A and B of spectra (a) and (c) on an expanded energy scale.

The present observation of an improved spectral resolution in the gas phase contrasts the experimental findings for some other large organic molecules (e.g., NTCDA [95]), where the spectral resolution was generally better for the condensed phase spectra. This different behaviour is explained by the higher sublimation temperature of NTCDA (e.g., 400 K resulting in a thermal energy of about 35 meV), which leads to an increased population of low-energy molecular bending modes (in the electronic ground state) [95] and consequently to a smearing of the respective transitions in the NEXAFS spectra.

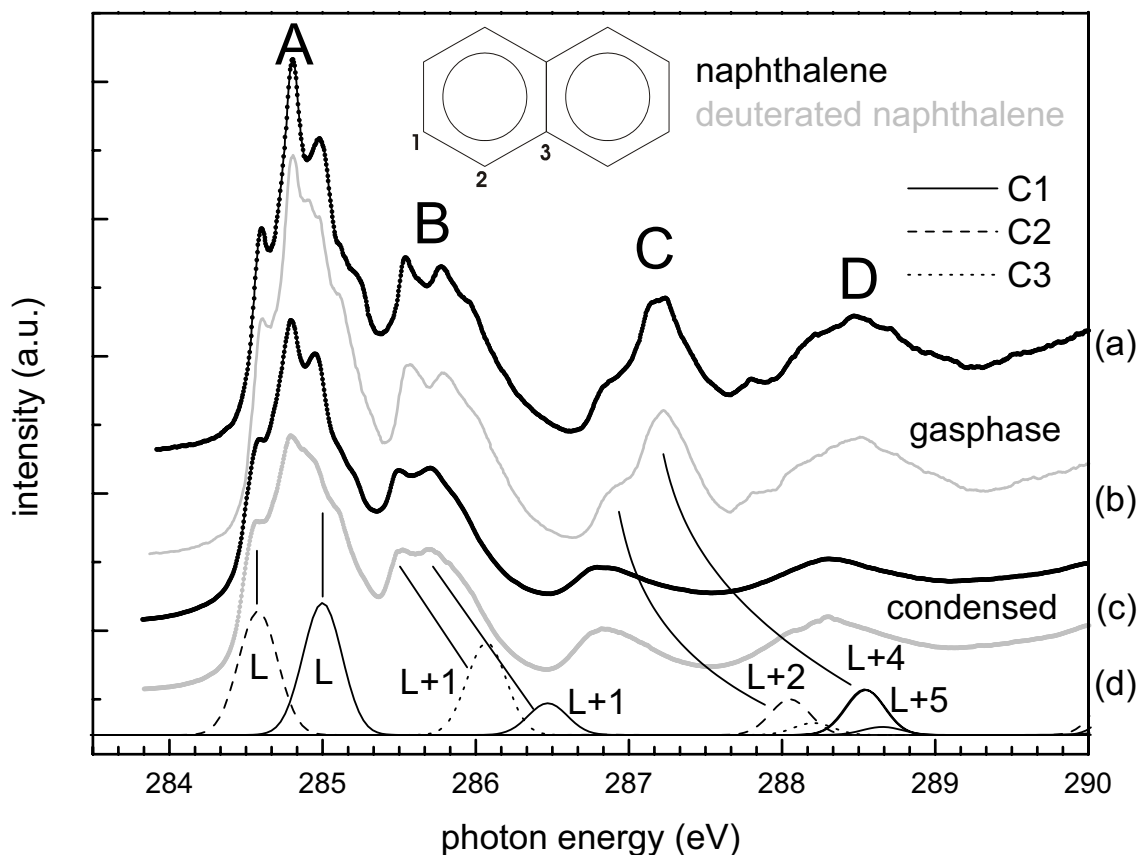


Figure 5.4: Comparison of the high-resolution NEXAFS C-K edge data for hydrogenated naphthalene (denoted h8, spectra (a) and (c)) and fully deuterated naphthalene (denoted d8, spectra (b) and (d)) in the gas (spectra (a) and (b), recorded in total ion yield mode) and condensed phase (spectra (c) and (d), recorded in partial electron yield mode). The condensed phase spectra were shifted by 300 meV to higher photon energy to align the first resonances. The four prominent regimes of resonances/progressions are labelled A-D. On the bottom the results of a GSCF3 calculation are presented (The expansion of the energy scale for the calculated spectra is well-known and is an artefact of GSCF3-calculations.). The calculated energy positions is plotted and the correspondences to the experimental spectra is marked. Different line styles represent the contributions of the inequivalent carbon atoms C1-C3. The final states of the most intense transitions are denominated. The chemically different carbon atoms in naphthalene are labelled C1-C3.

Table 5.2: Comparison of the Lorentzian (ω_L) and Gaussian (ω_G) contributions to the line shapes derived from a fit analysis of the leading edge of resonance A for gaseous and solid h8 and d8, respectively.

	ω_L/meV	ω_g/meV
d8 gas phase	84	73
h8 gas phase	83	71
d8 condensed phase	85	97
h8 condensed phase	84	101

Due to the high vapour pressure at room temperature in the present case of naphthalene no additional heating has to be applied. Therefore the thermal energy of 25 meV (200 cm^{-1}) is significantly smaller than for NTCDA. Moreover, for naphthalene the energetically lowest vibrations are found around 200 cm^{-1} (B_{3u} at 180 cm^{-1} and A_u at 190 cm^{-1}) [80], whereas in the case of NTCDA 8 fundamental vibrational modes are found well below the thermal energy at sublimation temperature (35 meV corresponding to 280 cm^{-1}). For NTCDA the vibronic spectrum starts with modes as low as 46, 79 and 83 cm^{-1} (see chapter 5.4), which consequently have a high population probability in the gas phase.

In order to extract the Gaussian and Lorentzian line widths of the Voigt profiles the leading edge of resonance A was fitted. This leads to a reliable result with respect to line widths while ignoring Franck-Condon factors. Corresponding results are listed in Table 5.2 reflecting the differences for the gas and condensed phase NEXAFS spectra of naphthalene. The core hole life time (i.e. Lorentzian width), is found to be unchanged between gas and condensed phase. The derived value of 83-85 meV is consistent with a theoretical prediction [96, 97] and previous results [63, 95, 98]. The increased Gaussian width in the condensed phase is attributed to inhomogeneous broadening from imperfect crystalline morphology in the naphthalene films. The small intensity differences of the vertical transition, leading to the peak with highest intensity, might be due to problems in normalisation of the solid state spectra, as this resonance is exactly in the carbon dip of beamline optics of the UE52/PGM-beamline.

Resonance B: At first glance gas phase and solid state spectra are similar in this energy regime. In analogy to the observation for regime A the gas phase spectra reveal better resolution. Resonance B has two main contributions from electronic transitions from C1 and C3 sites into the LUMO+1. In Fig. 5.5 the two contributing electronic excitations are labelled as b_1 and

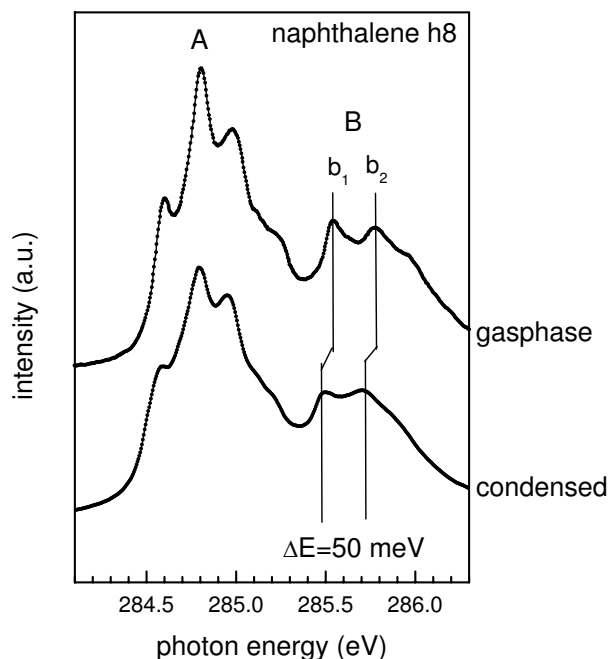


Figure 5.5: Comparison of resonances A and B of h8-naphthalene in the gas phase (a) and in the condensed phase (b). The two spectra are the same as spectra a) and c) in Fig. 5.4) but are plotted on an expanded energy scale. The energy shift of the two sub peaks in resonance B (denominated b_1 and b_2) is illustrated by guidelines.

b_2 . The asymmetric shape on the high energy side of both sub peaks, which can be better observed in the gas phase data, indicates the existence of unresolved vibronic progressions. Taking into account the different peak widths in gas and condensed phase, respectively, the peaks should be at identical positions as it is the case for resonances A. Most important, an energy shift is evident for resonances b_1 and b_2 , which is highlighted by the guidelines in Fig. 5.5. Both peaks simultaneously shift towards lower energy by 50 meV upon condensation. An identical shift occurs in the spectra of deuterated naphthalene.

As being part of a vibronic progression the peak positions of b_1 and b_2 are determined by the Franck Condon factors, i.e. shift and shape of the potential curve, as they correspond to the vertical transitions of the vibronic progression. Within the errorbar the shifts of b_1 and b_2 are identical (50

meV). Therefore a shift or shape change of the ground and excited state potential curves, respectively, can be excluded. The origin of this energy shift will be discussed below after the discussion of regimes C and D.

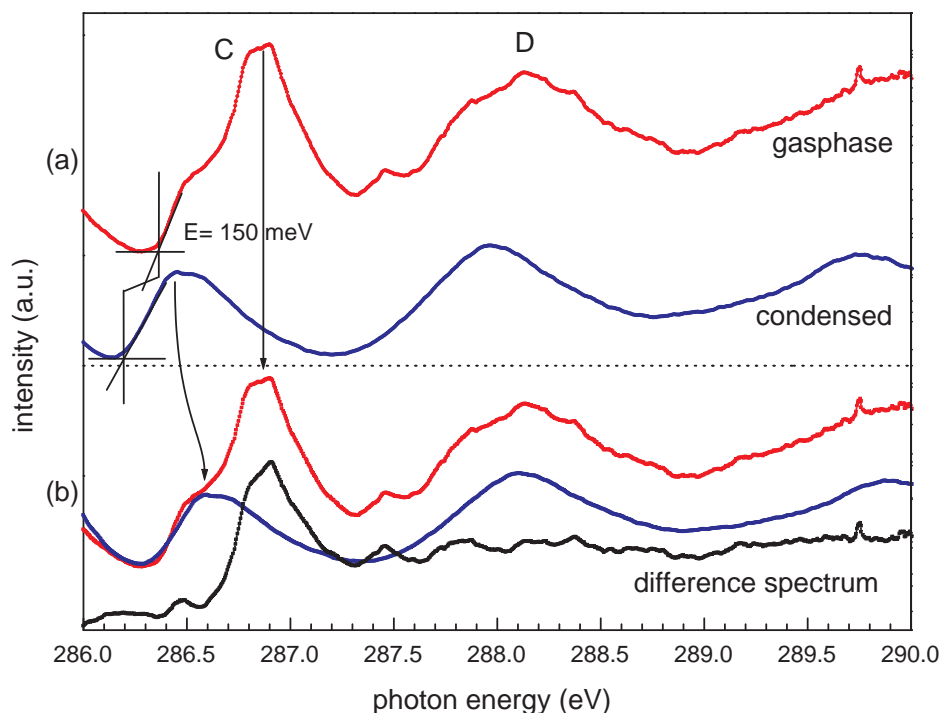


Figure 5.6: (a) Comparison of resonances C and D of h8 in the gas (red) and condensed (blue) phase (spectra (a) and (c) in Fig. 5.4). The energy shift of Res. C (150 meV) is deduced from the peak onsets and illustrated by guidelines.

(b) Difference spectrum (gas – condensed) which was generated after energy alignment of resonances C (the condensed phase spectrum was shifted 150 meV) and proper intensity rescaling to account for vanishing intensity around 286.5 eV.

Resonances C: The most striking difference between the gas and condensed phase data is found in regime C. This is illustrated by the extended plots of the respective energy region of spectra (a) and (c) in the upper part of Fig. 5.6. In the gas phase data resonance C clearly consists of (at least) two prominent structures, the shoulder at 286.5 eV and the prominent peak

at 286.85 eV. In the condensed phase, however, the latter has vanished and only an asymmetric structure around 286.4 eV is found. The shape of the structure can again be attributed to electron-vibron coupling. Moreover, this structure and its onset is obviously shifted towards lower energy by 150 meV in the condensed phase spectrum. This energy shift is indicated by the guidelines to the leading edges in Fig. 5.6.

In order to understand the striking disappearance of the most intense contribution to resonance C at 286.85 eV a correct assignment of the involved transitions is mandatory. According to the GSCF3 calculations (lower spectrum in Fig. 5.4) four electronic transitions are expected in the respective energy regime: two transitions from the C2 and C3 carbon atoms into the LUMO+2, one from a C1 atom to the LUMO+4, and one from a C2 atom to the LUMO+5 orbital. Whereas the first two transitions have π -symmetry, the latter two final states have σ -symmetry. According to theoretical analysis [72], [90] the σ -symmetric states have a mixed σ^* (C-H) and Rydberg character. The substantial Rydberg contribution is also indicated by our GSCF3 calculations, which show a relatively large expansion of the respective final states. On the basis of this spectral assignment the marked condensation effect can be easily understood as suppression of the spatially expanded Rydberg-like orbitals due to steric reasons.

For the expected spectral changes of Rydberg orbitals in the condensed state two controversial suggestions are found in the literature. Robin [99] predicts a broadening and blue shift of Rydberg transitions, while Bagus et al. suggest that the respective states are quenched, i.e. strongly decreased in intensity [100]. In case of the present naphthalene data a quenching of the Rydberg transitions apparently occurs considering the experimental observation of the resonances in regime C. However, it can not be completely excluded that the Rydberg orbitals are strongly broadened and blue-shifted above the ionization limit and thus no longer visible in the spectrum. The assignment to a Rydberg state is also consistent with the one drawn in [92] though there the difference is more general and merely seen for this specific resonance. In order to extract the signature of the Rydberg transition in the gas phase spectrum, the condensed phase spectrum was subtracted from the measured gas phase spectrum. For this purpose the latter was shifted by 150 meV to higher photon energy and properly rescaled. The resulting difference in the spectrum is shown in the lower part of Fig. 5.6. It proves that the resonances in regime C are a superposition of two features with only the low energy one being visible in both gas and condensed phase spectra. Interestingly, this approach yields additional information about resonance D.

Resonance D: is obviously shifted by the same value as resonance C which

becomes evident from the absence of this feature in the difference spectrum. This resonance contains various overlapping contributions from π^* - and σ^* -transitions from C1, C2, and C3 initial states, which are not listed explicitly here.

The difference spectrum is essentially flat in this regime, which leads to the conclusion that resonance D, being assigned to π^* and σ^* (C-H) transitions in the final state orbital, shows only minor contributions of Rydberg character. The origin of the weak structures seen in the gas phase superimposed on resonance D may be of Rydberg character as the condensed phase spectra do not show this fine structure. Note, the differences are not due to measurement artefacts.

Conclusions

High resolution C1s spectra of hydrogenated and fully deuterated naphthalene both in gas and condensed phase have been presented. Depending on the final state distinct differences are found between gas and condensed phase spectra.

Spectral shifts for π^* -resonances as presented here were not yet reported, though various systems were compared in gas and condensed phase, like, e.g., C_2H_4 [34]. For Rydberg resonances there are changes upon condensation reported [65,101] and controversially discussed as mentioned above. In Ref. [102] changes in Rydberg states for high quality n-tetracontane crystal-lites are reported, and it is suggested that an influence of the van-der-Waals interaction on the NEXAFS spectra might be the source of the observed effects. Nevertheless van-der-Waals interaction should only result, according to second-order perturbation theory, in a shift of the whole absorption spectrum [103]. However, in the present case of naphthalene clearly differential shifts depending upon the final state orbital are observed which do not fit in the mere van-der-Waals interaction framework. This is true for both, fully hydrogenated and fully deuterated naphthalene. Within the picture of pure van-der-Waals interaction such differential shifts of π^* -resonances are neither expected nor explainable. One might speculate that the different extension of the excited state orbitals might lead to changed polarizability of the molecules and consequently to the observed energy shift. However, in the present case of naphthalene the LUMO, LUMO+1 and LUMO+2 do not significantly differ in their spatial extension, and thus this effect cannot satisfyingly explain the observed differential energy shifts.

However differential energy shifts are well-known for σ^* -orbitals in NEXAFS spectroscopy as soon as they are involved in chemical bonding as derived

from the comparison of organic monolayer and multilayer films on various metal substrates [34, 104] where the molecules mostly bind to the metal via the π -electron system. Due to the π -symmetry of the involved final states the energy shift of resonances B, C and D is interpreted as a consequence of the π - π -interaction in the condensed phase. This is especially notable for resonance B which is undoubtedly assigned to an excitation into a π^* -orbital. The results lead to the interpretation that for organic molecular crystals more than pure van-der-Waals interaction has to be considered. Future calculations might provide further insight when taking the intermolecular interaction and ordered nature of condensed organic films into account.

5.3 ANQ as example for intramolecular interaction

High resolution O-K edge near X-ray absorption spectra of the organic molecule acenaphthenequinone (ANQ) in the gas and condensed phase will be presented in this chapter. The data is compared with another ANQ derivate having bromine and chlorine substituents at the naphthalene backbone ($\text{Br}_2\text{Cl}_2\text{-ANQ}$). In all cases the O K-NEXAFS resonances exhibit a similar vibronic fine structure which is discussed in the framework of the Franck-Condon picture. It can be concluded that preferentially one single vibrational progression couples to the resonant excitation of oxygen 1s core electrons. The unequal distances of the vibronic levels as derived from the least-square fit analysis of the vibronic progressions allows us to determine the anharmonicity of the involved excited state potentials. The comparison of the two derivatives gives a clear indication that the vibronic modes correspond to C=O stretching modes rather than C-H modes as stated previously for condensed ANQ films.

Introduction

With the advance of third-generation synchrotrons the spectral resolution in the soft x-ray regime has significantly improved and thus vibronic fine structure in near X-ray absorption fine structure (NEXAFS) spectra of even large molecules can be observed [60, 66]. In case of oxygen K-edge spectroscopy up to now the coupling of vibronic excitations to electronic transitions is usually reported for small molecules only (e.g., O_2 [105], CO [106, 107], or CO_2 [106, 108]. Vibrational resolution in NEXAFS investigations of polystyrene has been identified from an isotope effect in the C K-edge spectra of h-polystyrene/d-polystyrene [108]. In this particular case, the excitation is located on the respective functional group only, thus the polymer backbone is not involved in the excitation. Molecules like formaldehyde were investigated only recently [109, 110].

With increasing molecular size both an increasing number of electronic transitions and molecular vibrations ($(3N-6)$ normal modes with N being the number of atoms) will contribute to the spectrum leading to overlapping electronic transitions and a large number of vibrational modes. Therefore, only in cases where the electronic transition preferentially couples to one or only few vibrational modes the fine structure can experimentally be resolved and can thus be analyzed in detail. For condensed acenaphthenequinone (ANQ,

182 amu) vibronic progressions were detected in O K-edge NEXAFS [111]. ANQ so far was the largest organic molecule where vibronic fine structure has been observed for O 1s excitation. In Ref. [50] it was concluded that the excitation of O 1s electrons preferentially couples to C-H stretching modes since the vibrational energies correspond well to the C-H-modes detected in IR spectroscopy [57]. However, such coupling would require a strong interaction via the delocalized electronic system of the aromatic core which seems on first glance unlikely.

In this chapter high-resolution O K-edge NEXAFS investigation of acenaphthenequinone ($C_{12}H_6O_2$, ANQ, structural formula see Fig. 3.7) recorded in the gas phase for direct comparison with ANQ in the condensed phase will be reported. In addition, the ANQ derivate 3,8-dibromo-5,6-dichloro-ANQ ($C_{12}H_2Br_2Cl_2O_2$, in the following called Br_2Cl_2 -ANQ, structural formula see Fig. 3.7) will be examined. The latter substance has been chosen to unambiguously identify the origin of the observed vibrational mode in ANQ discussed previously in Ref. [50]. The vibrationally resolved C K-edge spectra of these substances will not be addressed here.

Experimental and fit details

Details about preparation of ANQ multilayer films (10-20 layers) on a Ag(111) surface deposited at 150 K are found in Ref. [50]. Br_2Cl_2 -ANQ films were prepared using the same routine. O K-edge absorption spectra of the condensed materials were recorded at the former U49/1-PGM undulator beamline [111] (now UE52-PGM beamline) at the high-brilliance synchrotron radiation source BESSY-II (Berlin, Germany). The spectral width at 530 eV is 56 meV yielding a resolving power $E/\Delta E$ of about 10.000. The energy calibration for condensed ANQ and Br_2Cl_2 -ANQ films using Ag substrate lines, is leading to an energy position of 530.08 eV and 530.5 eV, respectively, for the vertical transition E_v , which is the intensity maximum of the Franck-Condon envelope. Normalisation of the NEXAFS spectra of the organic films was performed with respect to I_0 spectra taken from sputter-cleaned Ag(111) surfaces [93].

The gas phase data were recorded at the Gas Phase Photoemission Beamline [74] at the synchrotron source ELETTRA (Trieste, Italy), which also has a high spectral resolution ($E/\Delta E=10000$ at 540 eV photon energy [94]). The ANQ powder was sublimated at 430 K in a high vacuum chamber (base pressure $1 \cdot 10^{-6}$ mbar). Thus a sufficiently high and stable flux of ANQ was achieved to obtain a good signal-to-noise ratio. The absorption signal was

monitored by detecting the total counting yield mode for (secondary) electrons and ions, respectively using two channeltrons opposite to each other. In order to take full advantage of the monochromator resolution spectra were recorded in the fixed mirror mode (i.e. only the monochromator grating is moved with 5 meV steps). For energy calibration the absorption from O₂ was simultaneously recorded with ANQ in an absorption chamber behind in the ANQ gas cell. A value of 530.8 eV for the first O₂ NEXAFS resonance [94] was used for energy calibration. The I₀ signal used for intensity normalization was recorded in parallel.

Commercially available ANQ was purchased from Sigma Aldrich and has been used without further purification. Br₂Cl₂-ANQ was provided by Prof. J. Siegel (ETH Zürich) [112]. The organic material was evaporated from a home-made Knudsen cell in a separate ultrahigh-vacuum preparation chamber. The pressure during evaporation did not exceed 5×10^{-9} mbar. In all preparations of organic multilayer films the Ag substrate was cooled to about 200 K. X-ray photoemission (XPS) of thus prepared films only showed very weak intensity of the 3d lines from the Ag substrate thus proving the homogeneity of the organic films.

The energy calibration of the gas phase spectra was performed by using the maximum of the oxygen π^* -resonance envelope. Different reference values are reported in the literature ranging from 531.06 [63], 530.8 [94] to 530.521 eV [113]. A value of 530.8 eV was chosen because the resulting value for gas phase ANQ of 530.14 eV is quite close to the solid state calibration (530.08 eV) in [50] which was done very accurately using calibrated Ag substrate lines. This is justified since the overall differences between gas phase and solid state spectra of ANQ are only minor.

The fine structure of the O K-edge NEXAFS spectra was analyzed by fitting Voigt peaks to the experimental data. In all cases, the energy position and the respective intensity of each Voigt line was fitted. The Lorentzian and Gaussian contributions of the Voigt lines can be determined best from the low-energy edge of the NEXAFS resonance profile. Thus derived parameters for the Gaussian and Lorentzian width were assumed to be valid for all Voigt profiles in the corresponding progression which is justified since the results of determining core-hole lifetimes should be identical in all cases.

DFT calculations using the B3PW91 functional (6-311G(d,p) basis set) within the GAUSSIAN 98 program package were used to calculate the ground state vibrations of ANQ and the ANQ derivate (see below). The DFT calculation is done on the basis and with the identical justification for basis and functional as described in chapter 5.4.

Experimental results

High-resolution O K-edge NEXAFS spectra of condensed multilayer ANQ film (a) and ANQ in the gas phase (b) are shown in Fig. 5.7. The peak-fitting results for the gas phase spectra and the resulting residuum (multiplied by a factor 4, spectrum c) are also plotted. In the lower part (Fig. 5.7d) the difference of condensed and gas phase spectra is shown together with the energy positions derived from the fit of the gas phase spectrum (b). In the difference spectrum a weak but nevertheless clear structure is observed, which will be discussed in detail below. Both O K-edge spectra in Fig. 5.7 show a pronounced fine structure. According to ab-initio calculations using the GSFC3-code [76,79] previously presented and discussed in Ref. [94] only one electronic transition is predicted for ANQ at the O K-edge. Therefore, the fine structure of this resonance must be attributed to excitations other than pure electronic transitions. For the investigated molecules no others than vibronic excitations are plausible.

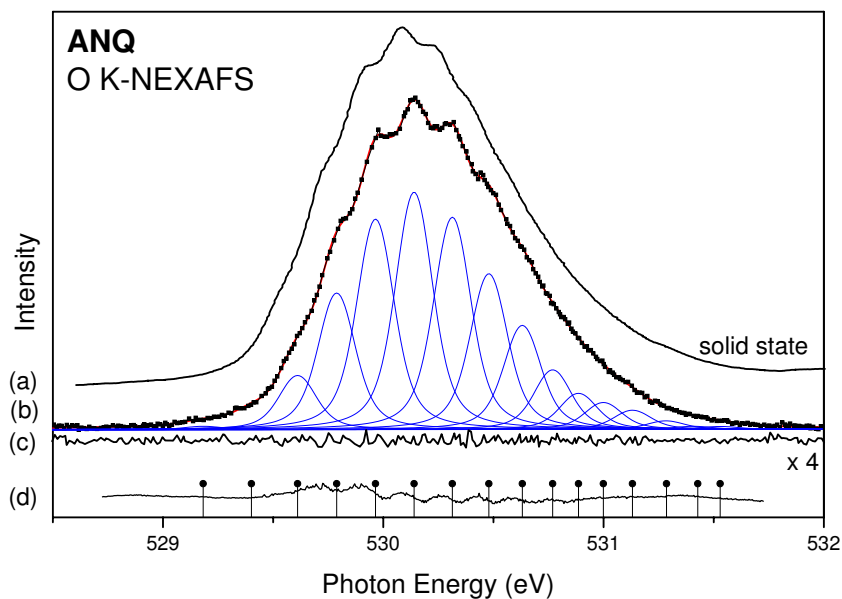


Figure 5.7: Comparison of the O K-edge NEXAFS spectra of (a) ANQ in the condensed phase (solid line) and (b) gas phase (black dots). A progression of Voigt profiles is fitted to the gas phase data (for details, see text). c) Residual spectrum comparing the experimental and fitted data (scaling factor: $\times 4$). d) Difference spectrum of gas phase and condensed phase spectrum together with energy positions of the Voigt profiles indicated as bars.

Therefore the spectra were analyzed in terms of a conventional Franck-Condon fit. In a first analysis harmonic potentials for ground ($V_{pot} = \alpha (R-R_E)^2$) and core excited state ($V_{pot}' = \alpha' (R-R_E')^2$) were applied (α is the harmonicity, R the normal coordinate of the observed vibrational mode, R_E describes the equilibrium distance and the apostrophe indicates parameters in the electronically excited state) to fit the gas phase data. However, the assumption of harmonic potentials (i.e. equidistant spacing of vibrational modes) did not result in satisfying fit results. Instead, an anharmonic potential had to be considered. The data was fitted with 16 identical Voigt profiles but free parameters for the intensity and energy position. The fit result is included in Fig. 5.7 – the derived data are listed in Table 5.3. The deviation from the experimental data (plotted on an enlarged scale in Fig. 5.7 c as residuum) underlines the very good agreement of the experimental and fitted data.

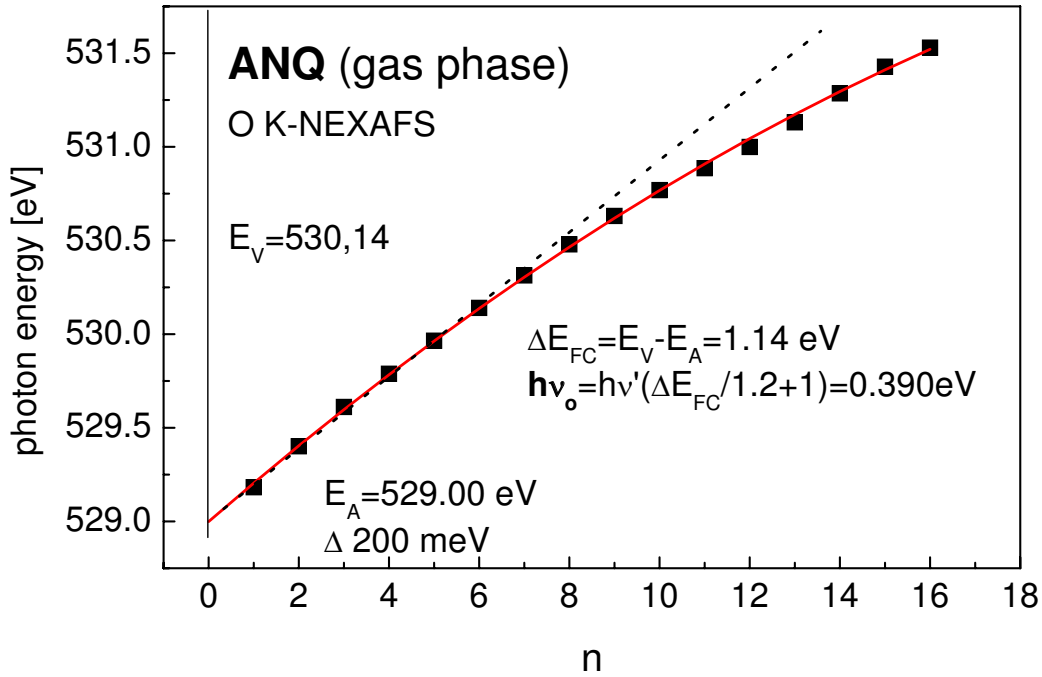


Figure 5.8: Energetic positions of the fitted ANQ resonances plotted versus the term value n . From the fitted curve $E_n = h\nu' (n+1/2) - \chi h\nu' (n+1/2)^2$ the parameters E_0 , $h\nu'$, the anharmonicity term $\chi h\nu'$ and the value of E_A can be deduced (see Table 5.3). The comparison with the straight dotted line reflects the deviation from the equidistant behaviour expected for harmonic potentials.

For better visualization, the energy positions of the fitted Voigt profiles are plotted in Fig. 5.8. There is a clear deviation from a linear behavior, which indicates the existence of an anharmonic potential in the electronically excited state. Considering a Morse-type potential

$$E(R) = E_D [1 - e^{-a(R-R_E)}]^2$$

the respective energy eigenvalues can be derived from perturbation theory using Laguerre polynomials. According to Ref. [114] the progression of energy eigenstates is described by $E_n = -D + h\nu' (n+1/2) - \chi h\nu' (n+1/2)^2$ [115], with $\chi = \frac{h\nu'}{4D}$ as anharmonicity, $h\nu'$ the ground state energy and n the vibrational level. The anharmonicity factor $\chi h\nu'$ can be deduced from a fit see Fig. 5.8.

The corresponding analysis leads to an anharmonicity factor of $\chi h\nu'$ of 3.2 meV, which is comparable to those found for other molecules like, e.g., CO with an anharmonicity factor of 1.7 meV [105]. This finding definitely justifies the assumption of an anharmonic potential.

The peak-fitting result for the NEXAFS spectra of condensed ANQ is also listed in Table 5.3 (previously reported in Ref. [50]) for direct comparison. In the excited states $h\nu'$ the vibrational energies do not differ at all. Both Lorentzian and Gaussian widths are in accordance with theoretical predictions [114]. The derived Gaussian widths are in both cases larger than the beamline resolution. Therefore the larger Gaussian widths is attributed to unresolved (low-energy) vibronic excitations.

The asymmetry of the Morse potential is slightly larger in the gas phase experiment which may be an indication that intermolecular interactions in the solid phase affects the excited state potential as well. The smaller Gaussian width for the gas phase ANQ indicates stronger contributions from inhomogeneous broadening and/or phonons in the solid state spectra, however, the differences are only minor and shall therefore not be overstressed in the present context. Strong intermolecular interactions in the solid state would affect both, the energetic positions of the resonances and the vibronic excitations. Therefore one may conclude that O K-edge NEXAFS is not sufficiently sensitive to probe the intermolecular interactions or that the intermolecular interactions in condensed ANQ are negligibly small.

Since NEXAFS probes the vibronic excitations in the electronically excited state it is difficult to compare the obtained results with those from ground state vibrational spectroscopy (e.g., IR spectroscopy or HREELS). In photoemission, an empiric formula $h\nu_o = h\nu' (\Delta E_{FC}/1.2 + 1)$ was derived, which allows to estimate the ground state vibronic excitations [38]. The lowest vibrational level ($n' = 0$) of the excited state is found at $E_A = 529.0$ eV, and the

Table 5.3: Comparison of peak fit results for the ANQ (in gas and solid phase, respectively) and ANQ-Br₂Cl₂ (solid phase only) O 1s \rightarrow LUMO resonance, in detail: Lorentzian (Γ_L) and Gaussian (Γ_G) line width of the Voigt profiles, energy of the adiabatic (E_A) and vertical (E_V) transition, Franck-Condon shift (ΔE_{FC}), anharmonicity (χ), and vibronic energy in the core-excited state ($h\nu'$). The vibronic state in the ground state ($h\nu_0$) was derived from the values given before. The error bar of the derived values is indicated in parenthesis.

Γ_L [meV]	Γ_G [meV]	E_A [eV]	E_V [eV]	ΔE_{FC} [eV]	$\chi h\nu'$ [meV]	$h\nu'$ [meV]	$h\nu_0$ [meV]	
97(5)	144(5)	529.00(4)	530.14(2)	1.14 (2)	3.2 (2)	200(2)	390 (2)	ANQ gas phase
97(5)	156(5)	528.98(1)	530.08(1)	1.10(2)	2.6(1)	200(2)	383(10)	ANQ condensed phase(data from Ref. [50])
97(5)	155(5)	529.39(1)	530.5(2)	1.1 (2)	2.0(1)	190(2)	366(10)	Br ₂ Cl ₂ -ANQ condensed phase

vibronic energy in the electronically excited state is 200 meV. The energy of the so called vertical transition (i.e., the maximum of the measured envelope of the vibronic progression) is $E_v = 530.14$ eV in the gas phase and 530.08 eV in the condensed phase, respectively. From $\Delta E_{FC} = E_v - E_A$ the Franck-Condon shifts $\Delta E_{FC} = 1.14$ eV (gas phase) and 1.1 eV (condensed phase) are derived, respectively. Applying these values to the above mentioned empiric formula the energy of the vibronic ground state can be estimated to 390 meV for the gas phase and 383 meV in the condensed phase, which we may consider identical within experimental uncertainty.

Note, that the above formula is derived for photoionization processes to derive ground state vibrational data. Only in few cases of small molecules like H₂CO, CO, NO and O₂ [109], the formula has been applied in NEXAFS spectroscopy to obtain accuracies below 10% compared to ground state vibrations of the respective molecules. This finding is encouraging enough to apply it to larger molecules as well. Within the error bar gas and condensed phase results lead to an almost identical ground state vibrational energy of 390

meV. This value fits best to a C-H stretching mode found between 381-386 meV as derived from FTIR data [38].

DFT calculations for isolated ANQ molecules using the B3PW91 functional (6-311G(d,p) basis set) within the GAUSSIAN 98 program package result in vibrational energies for the C-H stretching modes ranging from 3182 to 3208 cm^{-1} and for the C=O stretching modes from 1828 and 1845 cm^{-1} , respectively. The large deviation of the above derived values from the ground state C=O modes has previously lead to the conclusion that the O 1s excitations preferentially couple to C-H stretching modes. This discussion will be continued below.

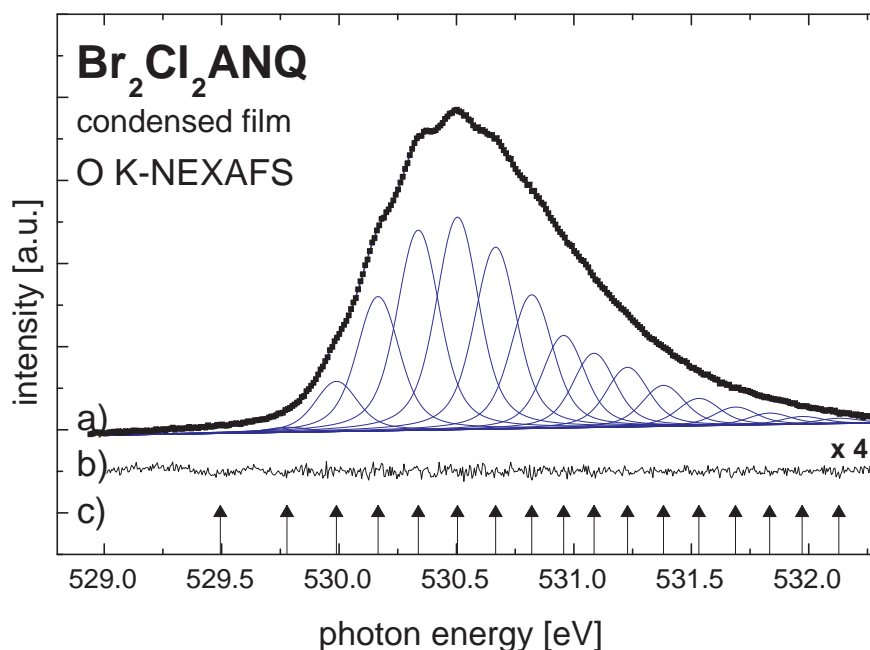


Figure 5.9: a) O K-edge excitation spectrum recorded for a condensed film of $\text{Br}_2\text{Cl}_2\text{-ANQ}$ together with the fitted progression of Voigt profiles. The energy scale was calibrated using Ag substrate lines leading to an absorption peak maximum at $h\nu = 530.5$ eV. b) Residual spectrum comparing the experimental data with the fit result on an enlarged scale (scaling factor: x 4). c) Energy positions of the fitted resonances.

In order to shine more light on this astonishing finding for ANQ the investiga-

tions were extended to a related molecule. In 3,8-dibromo-5,6-dichloro-ANQ (structural formula, see inset Fig. 3.7) four of the six hydrogen atoms of the naphthalene backbone are replaced by the electronegative halogen atoms Br and Cl. Thus, the vibronic coupling of O 1s excitations to hydrogen modes is expected to be significantly reduced if the interpretation given in Ref. [50] is valid. Since no significant differences for condensed and gas phase ANQ were observed, the high-resolution NEXAFS experiments for the ANQ derivate were performed for the condensed phase only. Thick films of the partially chlorinated and brominated ANQ derivate were prepared on sputter-cleaned and annealed Ag(111) substrates. The corresponding O K-NEXAFS spectrum is shown in Fig. 5.9.

The overall difference between condensed ANQ and its derivate is astonishingly small. As for ANQ, the chemically still identical oxygen atoms lead to a single electronic transition. Again, a vibronic progression is observed in the ANQ derivate. The most striking difference is an energy shift of about 400 meV to higher energies regarding E_v which is attributed to a chemical shift upon the replacement of four hydrogen atoms by bromine and chlorine atoms, which have a much higher electron withdrawing character compared to hydrogen. In addition, there is slightly higher intensity on the high energy tail of the vibronic progression which can most likely be attributed to a different shape and shift of ground and excited state potentials. Least-square fit analysis of the progression considering Voigt lines (Gaussian width: 155 meV; Lorentzian width: 97 meV) with variable energy position and intensity leads to the progression depicted in Fig. 5.9. The residuum plotted on an enlarged scale underlines the perfect quality of the fit with energy positions marked on the bottom of Fig. 5.9.

In order to visualize the energy positions and their deviation from the linear behavior, they are plotted in Fig. 5.10. The same functions as in Fig. 5.8 were fitted to the data points leading to parameters, which are listed in Table 5.3. As clearly seen from visual inspection, the deviation of the energy positions from linear behavior (dotted line) is slightly smaller than for ANQ (see Fig. 5.8). Thus, from the presented data, the anharmonicity in the ANQ derivate is less pronounced which is reflected in a 25% reduced anharmonicity factor.

The derived vibrational energy for the core-excited state of Br₂Cl₂-ANQ is slightly smaller than for ANQ. The DFT calculations (using B3PW91/6-311g(d,p) functionals) yield vibrational energies with wave numbers at 1852 and 1869 cm⁻¹ (both C=O character) and two modes at 3245 cm⁻¹ (both C-H character) for symmetric and antisymmetric modes, respectively.

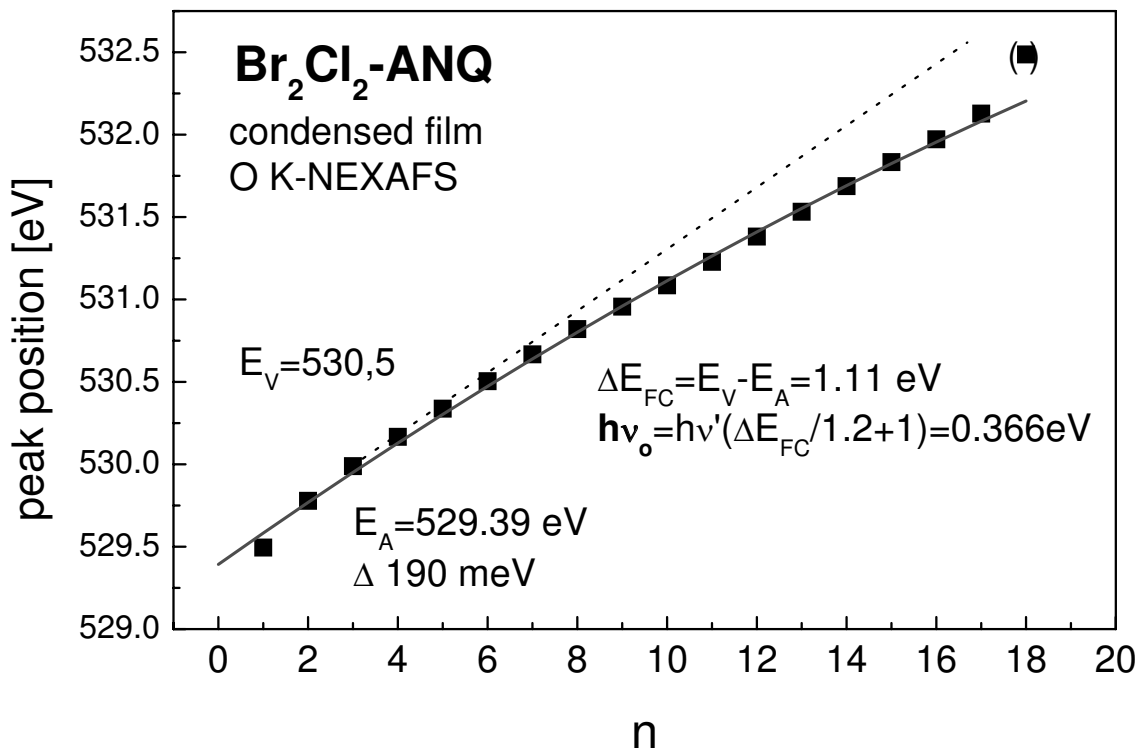


Figure 5.10: Energetic positions of the fitted resonances (compare Fig. 5.9) plotted versus the term value n . The solid curve is fitted to the empiric formula $E_n = h\nu' \cdot (n+1/2) - \chi h\nu' \cdot (n+1/2)^2$, from which the parameters E_0 , $h\nu'$, the anharmonicity factor $\chi h\nu'$ and the value of E_A are deduced. The parameters are listed in Table 5.3.

Discussion and Conclusion

A normal mode analysis indicates that the higher energy C-H modes are localized at the naphthalene rings and the C=O stretches are localized at the C(O)-C(O) structure. Judging from animations of the electronic ground state vibrations, C-H modes have no C=O contribution and vice versa for both ANQ and its derivate. Nevertheless, the redistribution of charge and the change of intramolecular distances which accompany the electronic excitation are the factors that influence the vibrational coupling and are not properly taken into account in the ground state picture. Therefore bonds distant from the excitation can become involved in the process leading to expectationally high overlap and hence Franck Condon factors for particular vibronic modes.

Especially reduction of symmetry upon creation of a core hole, located at an oxygen atom, may lead to some coupling to a C-H mode, whereas in a pure ground state picture the excited mode is expected to be of C=O character with C-H contributions.

In comparison, the high resolution O 1s NEXAFS spectrum of ANQ exhibits a very similar series as seen for O 1s NEXAFS spectra of carbon monoxide [116] and formaldehyde [109]. This might suggest a similar source of these common features, i.e., coupling to a C=O stretch. In the case of carbon monoxide [116], the fine structure of the O 1s π^* C=O is assigned to the carbonyl stretch mode. The resulting values for the vibrational energies are 166 meV for the electronic excited state and 269 meV for the ground state. Formaldehyde high resolution O 1s NEXAFS data [109] lead to the 217 meV (O 1s π^*) vibrational energy in the ground state and 136 meV in the electronically excited state. For both, the decreased vibrational energy of the vibrational levels in the electronically excited state indicates that the vibrational force constant is smaller in the excited state, which is consistent with an excitation into an anti-bonding molecular orbital leading to a destabilization of the C=O bond due to the O 1s core hole. Therefore the straightforward conclusion would be to assign the experimental findings in the case of ANQ and Br₂Cl₂-ANQ also to a coupling to a C=O mode. Nevertheless, one has to consider again that in the case of both examined molecules, a delocalized electronic system is involved. Thus one can conclude that an excitation into an anti-bonding orbital leads to decreased vibrational energy, but this cannot be unambiguously linked to excitation of a C=O mode.

The empiric formula used to achieve an estimation for ground state vibrational energy was originally derived by XPS data and has been applied in NEXAFS spectroscopy up to now only in small molecules. Generally no difference for this formula between XPS and NEXAFS is expected as the physics behind the dipole transition and the coupling is the same. The origin of this formula is the following: the more the electronic system is changed by the electronic transition, the more the potential curve in the excited state differs from the ground state. This change affects the equilibrium distance, the shape of the potential, and its anharmonicity. This leads to the observed shape of the Franck-Condon envelope, Franck-Condon factors and the vibrational frequencies in the excited state. Reference [50] shows that the formula works for the NEXAFS process for several large organic molecules within $\pm 5\%$. Thus it is encouraging to extend this idea to ANQ, but one has to take an increased error range into account.

So far when only taking ANQ condensed and gas phase data into account,

the previous assignment of the electronic excitation being coupled to a C-H vibration is still a possible and plausible interpretation. When the experimental results achieved for Br₂Cl₂-ANQ are included, the interpretation needs to be checked for consistency with these findings. Regarding the results for the vibrational excitation in the electronic ground state, both molecules are similar when only taking the numerical (DFT) values into account. In the case of the C=O modes, a moderate increase from 1828-1845 cm⁻¹ (ANQ) to 1852-1869 cm⁻¹ (Br₂Cl₂-ANQ) is found. The two remaining high energy C-H modes for Br₂Cl₂-ANQ are found at 3245 cm⁻¹, which is also an increased value compared to the six modes in the range between 3182-3208 cm⁻¹ for ANQ. The ground state energetic difference for both C-H and C=O is therefore, with a maximum energy difference of 4-5 meV, considerably smaller than the error margin for the ground state levels derived by the empirical formula. Nevertheless, the experimental findings indicate the different direction, i.e., the vibrational energy in the electronic ground state for ANQ is derived to be higher. In order to address this properly, the real vibrational levels need to be measured rather than to be calculated, as the expected error resulting from DFT calculations is not well established when atoms like Cl and Br have to be considered, though still included in the basis set used (B3PW91 functional; 6-311G(d,p) basis set).

Nevertheless, from the DFT calculations one can deduce that from the original six modes only two C-H modes, a symmetric and the asymmetric stretch vibration, are found in Br₂Cl₂-ANQ. Thus the delocalized electronic system, which has to be taken into account for the excitation process, has only two remaining C-H bonds to which the excitation may couple. Thus regarding the involved dipole matrix elements for the electronic excitations, a decreased value is expected in the case of Br₂Cl₂-ANQ as here only two C-H modes may contribute to an electron-vibron coupling. As the experimental findings do not indicate a change in the dipole matrix element, the assignment to an excitation of a C-H vibration becomes less likely. Nevertheless, a coupling to C-H modes cannot be excluded as a possible interpretation of the experimental results. In the case of vibrational coupling to C=O modes, the conditions are hardly different between the two examined molecules.

Summarizing this discussion, the results of the reported experiments are three-fold. First, ANQ and its derivate are so far the largest molecules revealing a vibronic progression for O K-edge excitations. The analysis of the energetic positions allows the anharmonicity of the potential in the electronically excited state to be deduced, which is more pronounced for ANQ compared to its partially halogenated derivate. Secondly, the similarity of the O K-edge spectra of ANQ in the gas phase and solid state clearly indicates

that in this particular system, the electron-vibron coupling is almost unaffected by neighboring molecules. Thirdly, the detected vibrational modes do not significantly differ for the two investigated molecular systems. However, the previous assignment of the vibronic modes to a very efficient coupling of the O 1s excitations to C-H stretching modes seems to be no longer clearly straight forward and both options coupling to C-H and C=O have to be taken into account.

5.4 Vibrational properties of condensed NTCDA films on Ag(111)

Highly ordered NTCDA (1,4,5,8 naphthalene-tetracarboxylic acid-dianhydride) thin films deposited on Ag(111) substrates have been investigated by means of high-resolution electron energy loss spectroscopy (HREELS) and Fourier-transform infrared spectroscopy (FTIR). DFT calculations using GAUSSIAN 98 reproduce the experimental data very well and allow a detailed assignment of the various vibronic modes. The evaluation of IR active modes furthermore allows the identification of the molecular orientation showing an essentially upright orientation with the molecular long axis parallel to the substrate for the used preparation.

Due to their various actual [83, 117, 118], and potential applications [6, 119, 120] in organic electronic devices, the adsorption and growth of large organic molecules on inorganic surfaces has been investigated intensively in the last two decades. However, many details regarding the influence of the substrate interface, such as surface morphology, steps and defects, and preparation conditions on the electronic, optical and structural properties of the organic film are still barely understood. Only a detailed knowledge of the interplay between the various parameters that can be adjusted in thin film preparation will allow the fabrication of devices with tailored properties. Thus by a proper choice of the substrate, growth rate, substrate temperature, carrier gas and dopant, the resulting film structure and morphology and hence the electronic and optical properties can be optimized [82, 121]. High-resolution electron energy loss spectroscopy (HREELS) has already successfully been applied to study vibrational and electronic properties of thin organic films [122, 123]. Taking particular advantage of the high surface sensitivity of this technique it is possible to investigate films in the coverage range from the submonolayer regime to multilayers by probing the topmost few layers.

This chapter focuses on the vibrational excitations that occur in condensed NTCDA films with particular emphasis on a detailed mode assignment and the correlation between vibronic excitations and film thickness. Previously HREELS has already successfully been applied to study vibrational and electronic properties of organic adsorbates and thin organic films [123–125] taking advantage of very high surface sensitivity of low-energy electrons. NTCDA is an ideal model system since it allows very different molecular arrangements to be prepared in multilayer films by only a small variation of the preparation conditions. For Ag(111) substrates, the molecular plane in the NTCDA monolayer films is coplanar with the substrate due to the covalent bonding between the molecular π -system and the metal surface [126]. In multilayer

films, however, the molecular plane is either coplanar with the surface for preparations with relatively high growth rate and substrate temperatures below 200 K or perpendicular for preparations with low growth rate at room temperature [48,127]. Recent NEXAFS experiments have demonstrated that a molecular orientation with an average inclination angle of about 45 degrees can be obtained in the temperature range in between these two regimes or for flat-oriented films upon annealing at room temperature [66,128,129]. This chapter is focused on multilayer film assignment of the various vibrational modes and the determination of the molecular orientation.

The inset of Fig. 5.11 displays the molecular structure of a single NTCDA molecule, which belongs to the symmetry group D_{2h} (mmm). The molecule has 66 vibrational degrees of freedom. Twenty-eight of these are IR-active (B_{1u} , B_{2u} , B_{3u}), 33 are Raman-active (B_{1g} , B_{2g} , B_{3g} , A_g) and 5 are silent (A_u) modes. The IR-active modes can be divided into modes for which the direction of the nuclear motion is out-of-plane (B_{3u}) or in-plane (B_{1u} , B_{2u}) with respect to the molecular symmetry plane. In the case of the B_{1u} modes, the vibrations are mainly polarized along the long molecular axis (x-axis in inset of Fig. 5.11), whereas for B_{2u} modes, the polarization occurs along the short axis. According to the so-called surface selection rule, infrared active modes, i.e., vibrations resulting in a dynamic dipole, will induce an image dipole in a metal surface. If the dipole is parallel (perpendicular) to the surface dipole, an image dipole will cancel (sum up) when the low-energy electron is scattered. Thus parallel modes are invisible, while perpendicular modes are visible, hence allowing the molecular orientation to be determined provided the assignment of the observed modes is known. Note that the surface selection rule is strictly valid only for molecules in the monolayer regime on a metal surface, while it is relaxed depending on the distance of the molecule from the surface and on the dielectric constant of the molecular layer.

The NTCDA molecular crystal grows in a monoclinic C_{2h}^5 (P2/c) [42] crystal structure with two molecules per unit cell and a lattice plane distance of 3.52 Å. The formation of a crystalline structure may induce two types of changes [130] of the molecular vibrations which are due to static and dynamic effects. The so called static field effects can lead to a frequency shift with respect to a single molecule. The point group of the molecule may be reduced leading to different selection rules since some previously forbidden modes become IR-active. The second effect is of dynamic nature and occurs when there are two or more molecules in the unit cell as is the case for NTCDA molecular crystals. This so-called Davydov splitting leads to a splitting of the signals of non degenerated modes and is expected to be in the range of

10-15 cm⁻¹ for molecular crystals which are bound by weak forces [131].

Experimental details and calculations

The NTCDA layers were grown from a home-made Knudsen cell by sublimation in ultrahigh vacuum (UHV) (base pressure $< 5 \cdot 10^{-10}$ mbar) on a Ag(111) surface. The NTCDA was purified by sublimation before loading the Knudsen cell. The utilized evaporation temperature was 480 K, corresponding to a growth rate of approx. 1 layer/min. The growth rate was calibrated by two well-known LEED patterns for monolayer coverage (the so-called relaxed (< 0.8 ML) and compressed monolayer (> 0.9 ML) [46]) and by XPS (using the same evaporator in a second chamber with similar geometry). A coverage of 1 monolayer (1 ML, saturation coverage) will be referred to a closed compressed monolayer of flat lying [48] molecules in the following. In contrast upright standing molecules with the long axes parallel to the substrate have an effective film thickness reduced by a factor of 2.7. The substrate temperature was set to 300 K in order to examine mostly upright standing molecules [48].

The Ag surface was cleaned in-situ by the conventional procedure of sputtering with Ar⁺ ions (HV = 500 V, sputter current 2.5 μ A, 15 min) and subsequent annealing to 800 K (30 min). The surface was checked for lateral order by low-energy electron diffraction (LEED) and for contaminations by HREELS. Once a clean surface with a sharp Ag(111) LEED pattern was achieved, the NTCDA film preparation was started. Directly after preparation of the thin film, the vibrational spectra were recorded. In order to keep possible beam damage as low as possible, the primary energy was set to 2.3 eV. All spectra were taken in specular geometry with an angle of incidence of 60° with respect to the surface normal. The samples were checked thoroughly for possible beam damage by comparing various single scans taken on a time scale of several hours and by repeatedly monitoring the LEED patterns but no damage, aging effects, or contaminations could be detected.

Subsequently, a spectrum with an excitation energy of 20 eV was taken in order to examine electronic transitions. Also, after this electron exposure, the vibrational spectra were checked thoroughly for beam damage or aging effects, but none could be detected. After the HREELS experiment, the LEED patterns of the NTCDA films were checked using primary energies below 15 eV. Even after using LEED for more than one hour (at significantly higher beam currents compared to HREELS) at energies below 15 eV, no signs of beam damage could be observed by LEED or HREELS. However, in high resolution SPA-LEED experiments, a decomposition of the multilayer

LEED pattern after several hours exposing the sample with 23 eV electrons could be detected (see Chapter 5.7).

FTIRRAS measurements were performed in a different UHV analysis chamber under very similar conditions. This chamber allowed XPS to be used to check for surface cleanliness and growth rate. The achieved vibrational resolution in FTIR was 2 cm^{-1} . Previous experiments in this chamber are described elsewhere [43].

It has already been shown for similar molecules, e.g., PTCDA 3,4,9,10-perylene-tetracarboxylic dianhydride [123], that the utilized DFT-calculations, though performed for an isolated molecule, are in good agreement with multilayer data as long as the interaction between the molecules is relatively weak. In this work DFT calculations for the vibronic spectrum were also performed for an isolated NTCDA molecule using Gaussian 98 A.7 [132, 133] with the B3PW91-functional to the basis cc-pVDZ. Note that for PTCDA, the B3LYP and B3PW91 functionals were used leading to good results [122, 123], but the energies tend to be overestimated for B3LYP, thus making complicated scaling routines necessary [134]. A combination of Beckes B88 [135, 136] and Perdew-Wangs PW91 [137] leads to the BPW91 functional which has been applied successfully to organic molecules with an energy accuracy of better than 2 % without scaling [138, 139]. This functional has therefore been favored in this work, and no scaling factor has been applied to the calculated results. The calculated frequencies are underlined in the following.

Results and discussion

For NTCDA on Ag(111) there are three known ordered superstructures in the monolayer regime which lead to distinct LEED patterns [47]. In all cases the NTCDA molecules are flat-lying on the surface, and the structures are not related to the NTCDA molecular crystal phase, which consists of two molecules with inclined molecular planes per unit cell. For thicker films in many of the previous studies, no distinct long range order was detected. During the present studies, reproducibly good quality LEED patterns confirming the existence of well-ordered multilayer films could be recorded, which will be presented in Chapter 5.7.

Vibrational properties

The first focus will be on the assignment of the various vibronic features in the experimental data supported by quantum-chemical calculations.

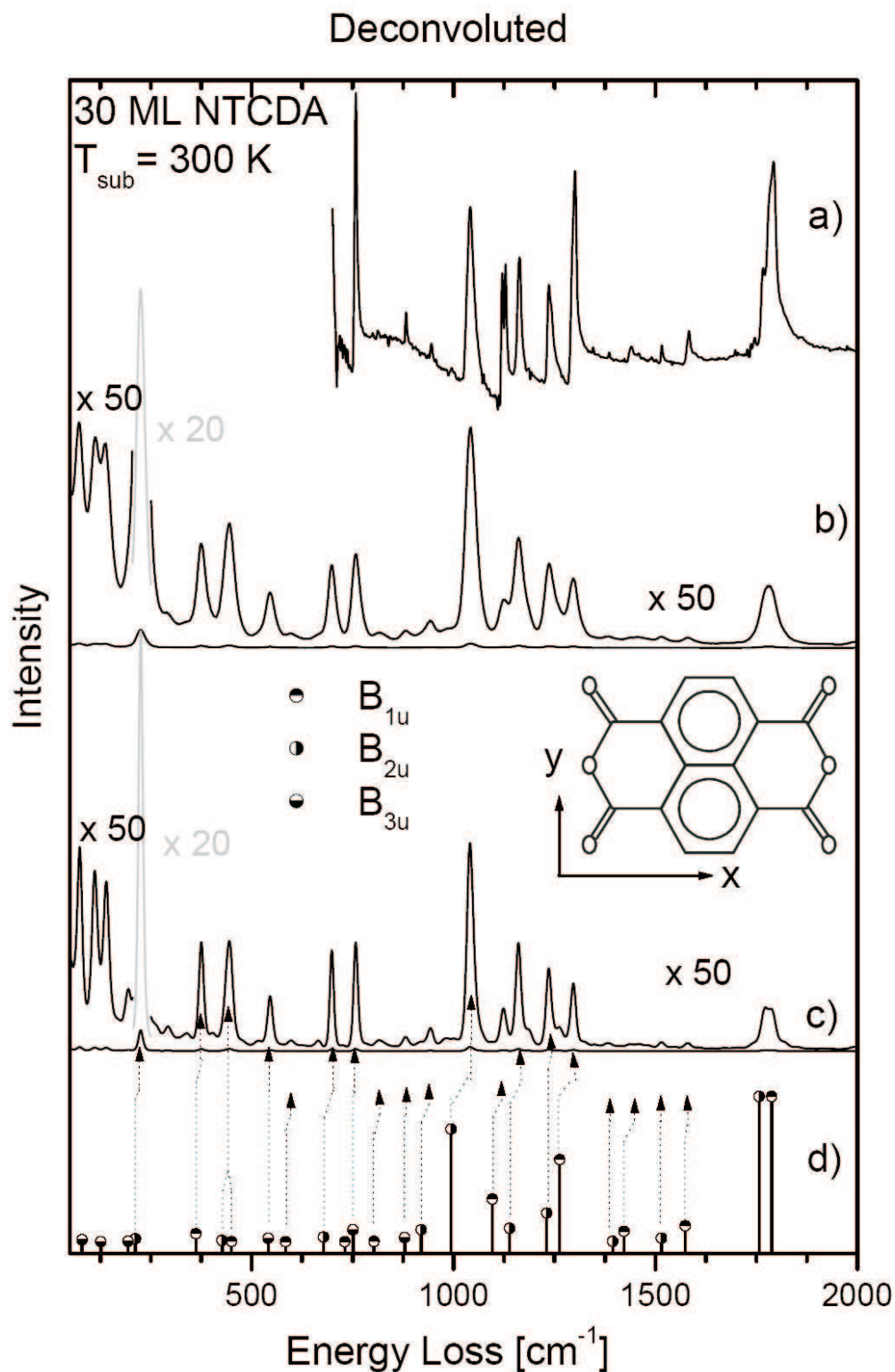


Figure 5.11: Vibronic spectra of various NTCDA multilayer films adsorbed on Ag(111) a) FTIR spectrum of a 20 ML NTCDA film [43], b) HREELS spectrum of 30 ML NTCDA, c) deconvolution of spectrum (b), and in the lower part of the figure results of DFT calculation are shown. The heights of the bars indicate the calculated intensities.

In Fig. 5.11 the result of a DFT calculation (spectrum (d)) is compared with the experimental HREELS spectrum (resolution 18 cm^{-1}) of a 30 ML NTCDA film (spectrum (b)). Spectrum (c) represents the HREELS spectrum after deconvolution with the spectrometer function (employing a routine as described in Refs. [139, 140]). In addition, a FTIR (Fourier Transformed Infrared Spectroscopy) spectrum is displayed (spectrum (a), from Ref. [43]) in order to identify IR-active modes, since FTIR strictly provides information only about modes with a dynamic dipole moment. As the Ag(111) surface is known to provide large terraces no SEIR (Surface Enhanced Infra Red) has to be taken into account, and therefore no activation of Raman active modes due to quadruple excitation.

There is a very good overall agreement between the deconvoluted experimental HREELS spectrum (c) and the calculations. The calculations reproduce the energy positions quite well, whereas the intensity of the peaks does not match that well. But this is expected as the measured intensity strongly depends on cross section, coupling effects, and the molecular orientation due to the selection rules.

The deconvoluted spectrum (c) reveals additional details without major artifacts as one can conclude from the comparison with the FTIR data and by the fact that each additionally revealed peak can be explained by the DFT calculations. The quasi-elastic peak has been used as instrument function for the deconvolution. The deconvolution leads to a resolution enhancement by a factor 3, thus resulting in a final resolution of 6 cm^{-1} . This allows, e.g., the distinction of symmetric and asymmetric C=O stretch modes at about 1780 cm^{-1} , which are separated by 31 cm^{-1} according to the calculations. Even for some very small features a counterpart in the FTIR spectrum can be found, as, e.g., the peaks at 882 cm^{-1} , 943 cm^{-1} , 1516 cm^{-1} , 1583 cm^{-1} . However, the split peak at 1120 cm^{-1} (split $\sim 8\text{ cm}^{-1}$) in Fig. 5.11a cannot be reproduced by the deconvolution (Fig. 5.11c).

For frequencies above 700 cm^{-1} one observes an excellent agreement between HREELS (spectrum (c)) and FTIR data (spectrum (a)) with respect to peak positions, as expected in specular geometry where IR-active modes dominate the spectrum. For every loss in the HREELS spectrum above 700 cm^{-1} a counterpart can be assigned in the FTIR spectrum. The fact, that the relative intensities are comparable indicates, that all peaks are due to dipole scattering, since in this case the intensity is proportional to the square of the dipole matrix element. For higher energies the loss intensity seems to be weaker for the HREELS data which is due to the decreasing transmission of the HREELS spectrometer. The different intensities of the modes at 758 cm^{-1} (B_{3u}), 1297 cm^{-1} (B_{1u}) and 1800 cm^{-1} (C-O stretch) are attributed

to slightly different preparation conditions leading to a different molecular orientation.

Dominant peaks

All losses can be divided into two groups: out-of-plane and in-plane modes. Out-of-plane modes, with B_{3u} symmetry, should only appear below 900 cm^{-1} according to the calculations. Modes with B_{3u} symmetry can be found at 74, 136, 194, 544, 759, and 884 cm^{-1} . The rest of the spectrum can be assigned to in-plane modes which have either B_{1u} or B_{2u} symmetry. A detailed peak assignment together with the experimental frequencies derived from FITR and HREELS, respectively, can be found in Table 5.4. Note, that this assignment is also in good agreement with previous infrared results from Aroca et. al. for NTCDA in KBr pellets [141]. The prominent features of the experimental spectra can be explained well by comparison to the calculations with only few exceptions in the low energy regime.

One of the strongest loss peaks is a B_{2u} in-plane mode at 1040 cm^{-1} (994 cm^{-1}) which is assigned to a δ -type HC-CH vibration. For this peak the calculations show the biggest misfit in energy position. A small peak at 991 cm^{-1} , however, would fit perfectly to the calculation. In this case, though, the observed strong peak can also be interpreted as multiple or combination loss which is, however, unlikely due to the low intensity of the vibrations that would contribute to this loss feature (eg. $(225 + 818)\text{ cm}^{-1} = 1043\text{ cm}^{-1}$ or $(291 + 758)\text{ cm}^{-1} = 1049\text{ cm}^{-1}$). Another explanation would be a breakdown of symmetry for the molecules in the film, thus leading to additional IR-active modes and therefore to a peak, but there is no infrared inactive vibration with a matching frequency near the losses. The by far strongest loss peak at 225 cm^{-1} will be explained when talking about the thickness dependent development of the spectra.

Multiple losses

After the assignment of all calculated IR-active modes (see Table 1) there are still some unexplained weak excitations, namely the losses at 291 cm^{-1} , 339 cm^{-1} , 515 cm^{-1} , 665 cm^{-1} , 991 cm^{-1} and 1997 cm^{-1} . Some of these features, e.g. the peaks at 339 cm^{-1} , 403 cm^{-1} , 515 cm^{-1} , 665 cm^{-1} and 991 cm^{-1} , are only visible as shoulders in spectrum (b), but are resolved in the deconvoluted spectrum (c). All these peaks can be explained by combination and multiple losses, which are well-known effects in electron energy loss spectroscopy [15]. Multiple losses should be observed with a frequency

that equals the sum (or a bit less than the sum in case of an anharmonic potential) of single loss channels present in the spectrum. This is not the case for combination losses, which are not IR-active themselves, but become IR-active due to their combined symmetry. E.g. the loss at 291 cm^{-1} may be due to a combination $A_u \circ B_{2g} = B_{2u}$ ($46\text{ cm}^{-1} + 237\text{ cm}^{-1} = 283\text{ cm}^{-1}$, according to the DFT calculations). The small deviation from the calculated value is within the error bar of the theoretical method. Note, that the calculations in this case can not give information about the expected intensities. However, a multiple loss of the modes at $74\text{ cm}^{-1} + 225\text{ cm}^{-1} = 299\text{ cm}^{-1}$ can also be a possible explanation which is particularly reasonable since one participant, the 225 cm^{-1} loss, is the strongest in the whole spectrum, thus indicating a significant intensity for its double excitation. The loss feature at 665 cm^{-1} matches very well to the sum of the two intense IR-active modes at 225 cm^{-1} and 445 cm^{-1} which is thus very likely the correct assignment for this loss. The other weak features in the experimental spectrum can be explained by various different multiple and combination losses thus making an unambiguous assignment impossible.

Thickness dependence

In Fig.5.12 the HREELS data obtained for three NTCDA films on Ag(111) with nominal layer thicknesses of 3, 6 and 30 ML, respectively, is shown. At first glance there is a very good overall agreement between the spectra, with the exception of some low-energy losses. However, a closer inspection provides two main changes for increasing coverage, the formation of additional energy losses below 200 cm^{-1} and an increase in intensity for the losses at 375 cm^{-1} , 544 cm^{-1} , 758 cm^{-1} and 1297 cm^{-1} .

First we focus on the low-energy losses below 200 cm^{-1} (grey box in Fig. 5.12). Some low-frequency modes in the DFT spectrum, e.g., three B_{3u} modes at 80 , 126 , and 193 cm^{-1} , do not fit to the experimental data as well as those in the higher energy regime. This is, however, not surprising since for condensates one would expect external modes in addition to internal modes in this energy range, particularly for a well ordered film. These so-called frustrated translations and rotations can couple to internal modes of the single molecule thus leading to new modes in the spectrum which can not be reproduced by the calculations for the isolated molecule. The relative changes in intensity for reduced coverage are different for the loss features at 52 , 74 , and 112 cm^{-1} in comparison to other peaks in the spectrum. While these peaks can clearly be observed in the 30 ML spectrum, they become less distinct at 6 ML coverage, where they can still be observed as

shoulders. At 3 ML, however, the peaks are smeared out into a broad feature which can hardly be distinguished from the background. According to group theory for C_{2h}^5 ($P2_1/c$) for external modes there are 12 phonons of which 3 modes are IR-active and thus observable for us (2 A_u and 1 B_u optical), 6 are Raman-active (3 A_g + 3 B_g librations), and 3 modes are due to the frustrated translation of the molecules in the crystal. This perfectly fits to the experimental observation of 3 IR-active losses and makes it very likely to assign these peaks to the respective phonon branches of the organic crystal. This finding is corroborated by the observation of ordered multilayer films by LEED.

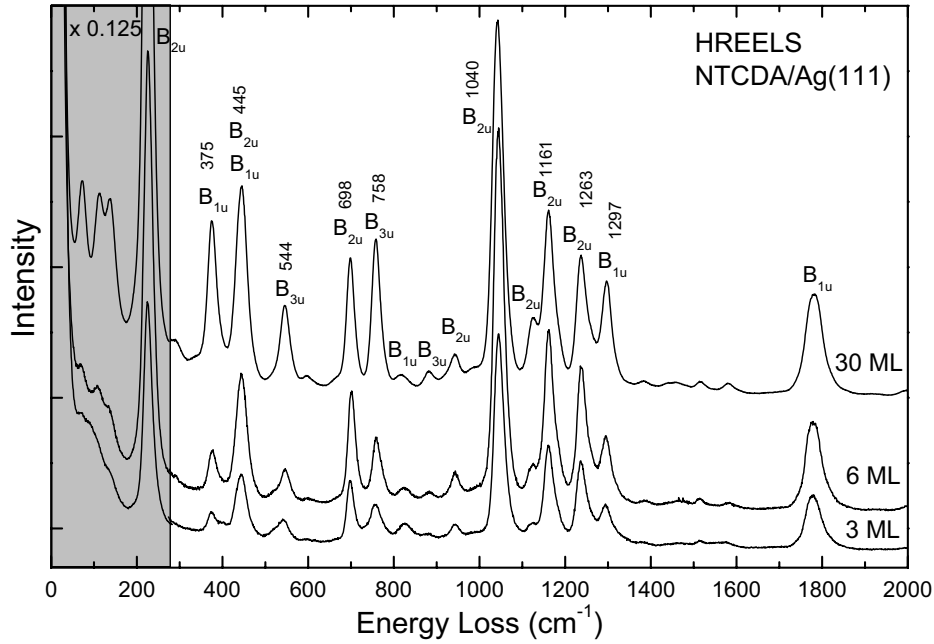


Figure 5.12: 3, 6 and 30 ML NTCDA films on Ag(111). All films were grown with 1 ML/min at $T_{sub}=300K$. Within the grey box the magnification of the spectra is decreased by a factor of 8.

With increasing film thickness the FWHM decreases from 28 to 18 cm^{-1} and the count rate increases by a factor of 3. This behaviour is most likely assigned to an increased lateral order in the films with increasing film thickness.

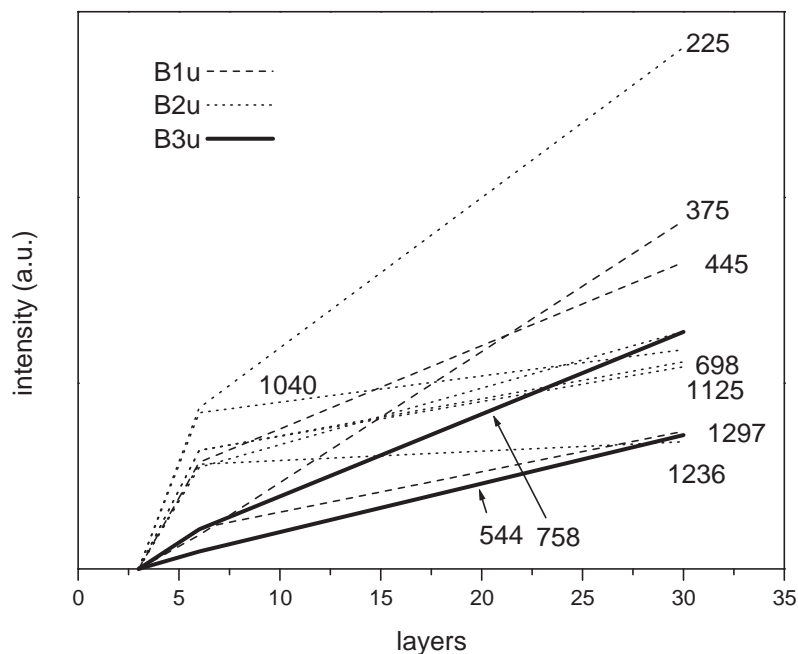


Figure 5.13: Experimental intensity of selected peaks as function of film thickness as derived from the HREELS spectra in Fig. 5.11 normalized to the respective intensity of the 3 ML film. Intensities for vibrations with B_{1u} and B_{3u} symmetry grow from 6 to 30 ML whereas B_{2u} modes hardly change.

Another group of peaks with similar intensity behavior consists of the B_{1u} modes at 375, 445, 1297 cm^{-1} , mentioning only the strongest peaks. In Fig. 5.13 the intensities of the different vibrations (normalized to the intensities at 3 ML coverage) are plotted as function of film thickness. A trend for intensities is observed. Some modes grow strongly with increasing film thickness whereas other modes do not show this behavior. The intensity of B_{2u} modes (dotted lines in Fig. 5.13) merely changes for films thicker than 6 ML. This is consistent with a growth model with upright standing molecules with the anhydride axis parallel to the surface, since for this configuration the B_{1u} modes are parallel to the surface as well as the B_{3u} modes. This model is consistent with other results, e.g. the LEED data (see chapter 5.7), the findings of Aroca et al. [141] and NEXAFS results [48].

The by far strongest loss peak in the spectrum is that at 225 cm^{-1} . A

straight forward assignment is the B_{2u} mode calculated to be at 212 cm^{-1} . Nevertheless the intensity of the peak clearly depends on the film thickness in the same way as the low energy losses (see Fig. 5.13). The frequency for this mode is rather high for a phonon, thus this peak is most likely related to the film structure. The validity of this interpretation is corroborated by the discussion in Chapter 5.5 since for a different molecular orientation this peak disappears. Therefore this mode is assigned to a coupling of an internal to an external mode, which in this case is only possible due to the upright orientation of the molecules on the RT substrate.

Conclusion

The growth of NTCDA multilayer films on Ag(111) prepared at room temperature have been investigated. The vibrational data in FTIRRAS and HREELS are consistently explained by DFT calculations. From symmetry arguments it is found that the molecules are almost standing upright with their long axis (C=O bonds) essentially parallel to the surface. The relative intensities of B_{1u} and B_{3u} modes on the one and of the B_{2u} modes on the other hand strongly indicate the on edge orientation of the molecules.

Table 5.4: Assignment for NTCDA room temperature multilayers

HREELS $T_{sub}=300K$ (cm^{-1})	FTIRRAS (cm^{-1})	Theory BPW91/ cc-p VDZ (cm^{-1})	Assignment	race	FTIR KBr Pellet Aroca (cm^{-1})
52		46		Phonon	
74		80 (z)	anhydrid butterfly	Phonon or B_{3u}	
112				Phonon	
136		126 (z)	naphthalene butterfly + $\tau_{Dianhydrid}$	B_{3u}	
194		193 (z)	naphthalene butterfly + $\tau_{Dianhydrid}$	B_{3u}	203
225		212 (y)	$\rho_{Dianhydrid}$	B_{2u} +Phonon	221
291		278		combination	
375		362 (x)	$\delta_{C-O-C} + \rho_{C=O} + \rho_{C-H}$	B_{1u}	374
445		427 (y) 450 (x)	$\delta_{C-O-C} + \delta_{Ring}$ $\delta_{C-O-C} + \rho_{C=O} + \delta_{Ring}$	B_{1u} B_{2u}	474
544		541 (z)	naphthalene butterfly	B_{1u}	545
597		584 (x)	$\delta_{C-O-C} + \delta_{Ring}$	B_{1u}	
698		678 (y)	$\rho_{C=O} + \delta_{Ring}$	B_{2u}	698
725		731 (x)	$\rho_{C-H} + \delta_{Ring} + \delta_{C-O-C}$	B_{1u}	
758	759	751 (z)	$\omega_{C-H} + \omega_{Dianhydrid}$	B_{3u}	758
818	812	803 (x)	$\rho_{C-H} + \delta_{Ring} + \delta_{C-O-C}$	B_{1u}	
884	882	879 (z)	ω_{C-H}	B_{3u}	882
942	945	920 (y)	$\nu_{C-O-C} + \delta_{C-H} + \delta_{Ring}$	B_{2u}	944
1040	1048 1053	994 (y)	$\nu_{C-O-C} + \delta_{C-H} + \delta_{Ring}$	B_{2u}	1035
1125	1121 1128	1096 (x)	$\delta_{C-H} + \nu_{C-O-C} + \delta_{Ring}$	B_{1u}	1120
1161	1167	1139 (y)	$\delta_{C-H} + \nu_{C-O-C} + \delta_{Ring}$	B_{2u}	1161
1236	1244	1231 (y)	$\delta_{C-H} + \nu_{Ring} + \nu_{C-O-C}$	B_{2u}	
1297	1302	1263 (x)	$\nu_{C-O-C} + \delta_{C-H} + \delta_{Ring}$	B_{2u}	1292
1383		1394 (y)	$\nu_{Ring} + \delta_{C-H}$	B_{2u}	
1438,52	1438	1422 (x)	$\nu_{Ring} + \rho_{C-H}$	B_{1u}	1438
1513	1515	1515 (y)	$\nu_{Ring} + \delta_{C-H}$	B_{2u}	1516
1579	1583	1574 (x)	$\nu_{Ring} + \rho_{C-H}$	B_{1u}	1583
1773	1747 1771	1757 (y)	$\nu_{C=O}$ asymm	B_{2u}	1762
1785	1784 1810	1788 (x)	$\nu_{C=O}$ symm	B_{1u}	1779

5.5 Preparation effects on the vibrational properties in NTCDA multilayer films

The vibrational properties of NTCDA (1,4,5,8 naphthalene-tetracarboxylic acid-dianhydride) multilayer films have been investigated by means of high-resolution electron energy loss spectroscopy (HREELS) in the previous chapter. In a next step depending on the preparation, different morphologies and molecular orientations can be prepared which can be distinguished in the HREELS spectra by identification of specific vibrational modes and their symmetry. This chapter examines the influence of different growth parameters (film thickness, sublimation rate, temperature). The detection of monolayer-related excitations and the observation of external vibrational modes (bulk-like phonons) indicate a Stranski-Krastanov mode for NTCDA multilayer film growth. In addition, electronic excitations were examined to deduce preparation effects on the HOMO-LUMO gap.

Introduction

In order to improve the properties of organic devices, well-defined organic thin films are required. Organic-inorganic heterointerfaces have therefore received considerable attention in fundamental and applied research. However, many details regarding the influence of the preparation conditions during film growth on the electronic, morphologic and structural order in the organic adlayer are still lacking comprehensive understanding.

This chapter addresses the question of organic thin film preparation using medium-sized planar and functionalized aromates. NTCDA is an ideal model system for this study since it allows strongly different molecular arrangements in multilayer films to be prepared by only small variations of the preparation conditions.

The present chapter extends a previous high-resolution electron energy loss spectroscopy (HREELS) study of NTCDA (1,4,5,8 naphthalene-tetracarboxylic acid-dianhydride, molecular structure see inset in Fig. 5.14) multilayer films prepared on Ag(111) at room temperature (298 K), see Chapter 5.4.

Two additional aspects will be addressed here. First, the effect of film preparation at different substrate temperatures (180 K versus 298 K, in the following denoted as LT (low temperature) films and RT (room temperature) films, respectively) during deposition of the molecules will be investigated. In addition, growth rates were varied to monitor the influence of the adsorption

kinetics. The second aspect concerns electronic excitations in the differently prepared films. This may give insight into the intermolecular interactions, which are governed by the overlap of the π -orbitals. As will be demonstrated, variation of the preparation conditions results in different molecular arrangements and thus in significantly different π -interactions between the molecules.

Experimental details

The experimental details described in Chapter 5.4 also apply here; specific details are outlined hereafter. The growth rates were varied by changing the temperature of the Knudsen cell from 450 K to 480 K resulting in a rate of 0.1ML/min and 1ML/min, respectively. The substrate temperature during deposition was varied between 298 K and 180 K in order to examine two well-known multilayer growth regimes, i.e., mostly upright standing (for the substrate held at room temperature (RT)) and flat lying molecules (for substrate temperatures below 200 K) [48].

For vibronic excitations in specular geometry, predominant dipole scattering is expected, i.e., HREELS probes infrared active modes. Note that surface selection rules apply. Thus, a dynamic dipole will induce an image dipole within the metal surface and the approaching electron will detect the sum of both. If the dipole is oriented perpendicular (parallel) to the surface, the sum of dipoles can (cannot) be observed. However, this rule is strictly valid only close to the surface. If there is an intermediate dielectric layer, the rule will be weakened and parallel modes may also become visible in the spectrum. It is emphasized that the samples were kept either at room temperature (for preparations at 298 K) or at about 100 K for preparations at 180 K during the HREELS experiments.

Results and Discussion

Influence of the substrate temperature during film growth

In Fig. 5.14 the HREELS spectra for two different NTCDA multilayer films prepared on Ag(111), recorded for an electron kinetic energy of 2.3 eV are compared. The nominal film thickness in both cases was around 30 ML. In order to compare the two layers, both spectra were normalized to the intensity of the elastic peaks. In the upper spectrum, the films were prepared at a substrate temperature of 180 K, whereas the lower spectrum was recorded after room temperature preparation. Individual sections of the spectra were

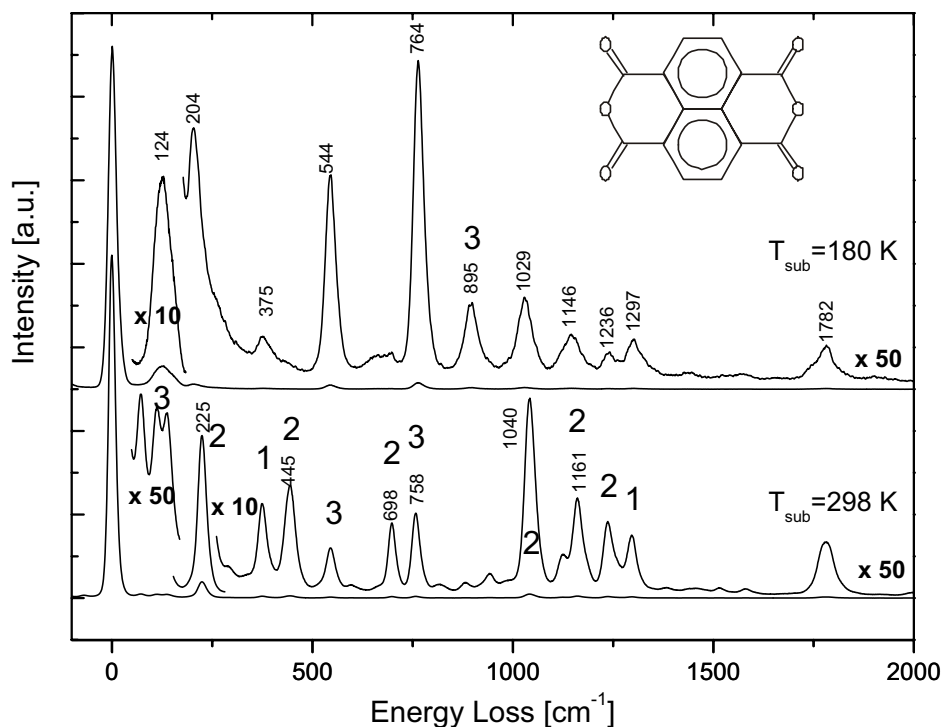


Figure 5.14: HREELS spectra for NTCDA multilayer films prepared on Ag(111) at two different substrate temperatures (electron kinetic energy: 2.3 eV). Upper spectrum: substrate temperature 180 K (film thickness: 15 ML). Lower spectrum: substrate temperature kept at room temperature (298 K), film thickness: 30 ML. Different sections are plotted with the given magnifications. Arabic numbers 1-3 are an eye guide to distinguish between B_{1u} , B_{3u} and B_{2u} modes according to the assignment based on DFT calculations (see table 1), other numbers refer to the loss energy in cm^{-1} . The inset shows the structural formula of NTCDA.

amplified by the given factors for better recognition of the fine structures. It should be mentioned that the intensity of the elastic peak for the films prepared at lower temperature is smaller by about a factor 3 compared to the RT films.

Before discussing the differences between the two spectra previous results on a detailed peak assignment of vibrational excitations in NTCDA films prepared at room temperature (lower spectrum in Fig. 5.14) is briefly reviewed. The assignments given in Chapter 5.4 are based on a comparison with DFT calculations (using the BPW91 functional to the cc-pVDZ basis). The results are summarized in Table 5.5 (compare columns b - e in table 5.4).

All major peaks above 250 cm^{-1} are straightforwardly assigned to infrared active modes (for more details see below). Below 200 cm^{-1} the peaks are assigned to infrared active phonons which are expected for thicker films, since these condense in the structure of the NTCDA crystal (point group C_{2h} ⁵). The peak at 225 cm^{-1} was assigned to a coupling of an internal B_{2u} mode to an external mode because it clearly depends on film thickness. In addition, this resonance seems to be energetically too high to be only due to external motion. The other three low energy peaks ($52, 74, 112\text{ cm}^{-1}$) showed a similar behaviour as a function of film thickness. Thus their attribution to phonons is plausible. These findings from the HREELS spectra together with a well-defined electron-diffraction pattern recently observed for RT multilayers (see Chapter 5.7) lead to the conclusion that in room temperature substrate films the molecular plane is oriented almost upright (82°) with the anhydride-anhydride axis parallel to the surface.

The comparison of the two spectra in Fig. 5.14 reveals a wealth of differences. Some peaks have almost completely vanished in the upper spectrum, some are new and some peaks have drastically increased in intensity. The intensities of the B_{3u} (out-of-plane) modes at $204, 544, 764$ and 895 cm^{-1} , respectively are enhanced for the LT film compared to the RT layer and virtually no shift in frequencies is observed. Only the peak with the highest loss energy is shifted from 884 cm^{-1} (RT film) to 895 cm^{-1} (LT film) which is attributed to the strong C-H character of this molecular vibration. The change in intensity is supposed to be due to a different molecular orientation. For flat lying molecules (LT film) the dynamic dipole is perpendicular to the surface and thus the surface selection rule is satisfied.

For all B_{2u} modes one generally finds a decrease in intensity for LT films (upper spectrum). In particular the features at 445 and 698 cm^{-1} become very weak so that they almost merge with the background intensity. Other B_{2u} modes (namely $1040, 1161$ and 1236 cm^{-1}) also decrease strongly but are still observable. The assignment of the mode at 1236 cm^{-1} is straightforward since there is no shift for this loss for the differently prepared films. The loss peak at 1161 cm^{-1} (RT film), at first glance, seems considerably shifted to 1146 cm^{-1} for the LT film. However, this peak is interpreted as the unresolved superposition of the merely changed B_{1u} intensity 1125 cm^{-1} with the intensity decreased B_{2u} mode at 1161 cm^{-1} . The scissoring H-C-C-H mode at 1040 (994) cm^{-1} is shifted to 1029 cm^{-1} . This loss has the largest perturbation when comparing DFT calculation for a free molecule and a condensed film. In [141] this mode is found at 1037 cm^{-1} also being assigned to a B_{2u} mode with comparable shift with respect to calculations. This shift and accordingly the shift between the different orientations might be due to

a large contribution of C-H modes to this vibration. In the molecular crystal the shift can be understood, since in-plane C-H bending modes are hindered due to the vicinity of the oxygen atoms of the neighboring molecules [42].

The B_{1u} modes found at 375, and 1297 cm^{-1} show a small decrease in intensity which is, however, not as strong as for B_{2u} modes. B_{1u} modes have the same orientation with respect to the surface for both upright-standing and flat-lying molecules, if the long molecular axis is assumed to be oriented parallel to the substrate surface. They are supposed to be forbidden by the surface selection rule for both orientations but become visible due to the intermediate dielectric layer of molecules which weakens this rule. In addition, the decreasing intensity might be a hint that the long molecular axis is not perfectly parallel to the surface plane for RT films as an angle with respect to the surface will lead to nonzero dynamic dipole moment perpendicular to the surface.

Also for losses below 250 cm^{-1} the signature in the LT film changes drastically. Instead of the three low energy phonon bands in the RT film (at 52, 74, 112 cm^{-1}) there is a broad loss feature centered at 124 cm^{-1} . This peak is the most intense loss peak throughout the whole spectrum. The changes can be understood in terms of different phonons which associated with the different molecular orientation for the two preparations. Independent of the orientation for both cases phonons are expected in the same energy range. Nevertheless, also for flat-lying molecules one would expect to observe the three low-frequency B_{3u} modes at 80, 126, and 194 cm^{-1} since they should now fulfil the surface selection rule. The loss at 124 cm^{-1} is assigned to an unresolved superposition of the 80 and 126 cm^{-1} peaks since it is clearly asymmetric and rather broad (FWHM = 60 cm^{-1}). The 204 cm^{-1} loss peak in the LT spectrum is assigned to the third B_{3u} mode which was assigned in the RT films to a loss at 194 cm^{-1} (193 cm^{-1}) only in the deconvoluted spectrum. The by far strongest loss peak in the RT films is found at 225 cm^{-1} (it is only magnified by a factor of 10). In LT films this feature vanishes which corroborates the interpretation of a coupling from an internal B_{2u} to an external mode in RT films.

The above findings for the intensities of the different symmetry groups perfectly fit to the model of upright standing and flat lying NTCDA molecules in the RT and LT films, respectively. However, since surface selection rules are not strictly applicable HREELS cannot exactly derive molecular orientations from the symmetry arguments given above. In contrast to the previous NEX-AFS study, however, it can be concluded that in the upright standing phase, the long molecular axis is not oriented perpendicular to the Ag substrate.

Influence of different growth rates

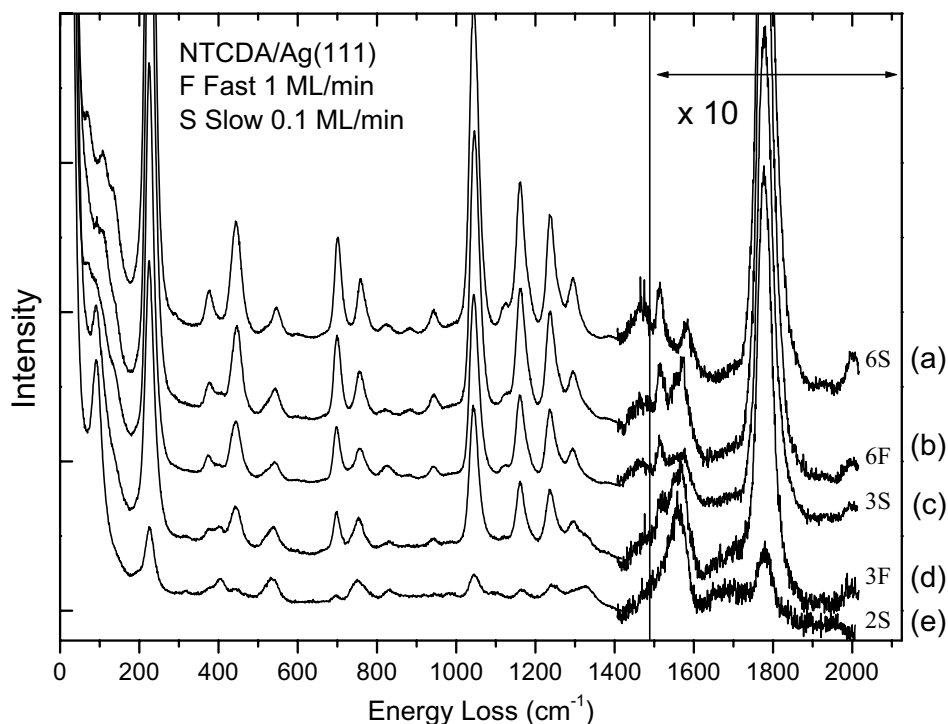


Figure 5.15: HREELS spectra of NTCDA multilayer films with nominal thicknesses of 6 (a, b), 3 (c, d) and 2 ML (e) grown with two different rates. Samples (a), (c), and (e) were grown at a rate of 0.1 ML/min whereas samples (b) and (d) were grown at a rate of 1 ML/min (1 ML refers to one saturated layer of flat-lying NTCDA molecules). The Ag(111) substrate was kept at room temperature during film growth. The spectral differences are most obvious for the low-energy phonon losses ($< 200 \text{ cm}^{-1}$) and for the loss feature around 1550 cm^{-1} , which is restricted to the monolayer (see text).

Whereas in the previous section the temperature during deposition was varied, now the influence of the growth rate for RT films in the intermediate thickness range will be examined. In Fig. 5.15 the HREELS spectra for differently prepared NTCDA multilayer films are shown. Coverages of 2, 3 and 6 monolayers were prepared at growth rates of 0.1 ML/min (spectra a, c, and e) and 1 ML/min (spectra b, and d).

There are two regions in the spectra where one can observe clear differences. First we turn our attention to the low energy losses below 150 cm^{-1} . There is a strong B_{3u} loss at 90 cm^{-1} (80 cm^{-1}) due to an anhydride mode (so-called

butterfly motion) in the submonolayer range which is observable in the 2 ML film (spectrum e) and also for the 3 and 6 ML film grown at 1 ML/min (spectra d and b). In spectrum c. (3 ML at 0.1 ML/min) the shoulder in this energy range develops to the above discussed phonon band in spectrum a (6 ML film at 0.1ML/min) whereas these features are smeared out in the films which are prepared at higher rate. This finding indicates that the lower growth rate of 0.1ML/min leads more to a signal, that is related to an ordered film (see lower spectrum in 5.14) than the 1ML/min growth regime.

The second interesting region lies in the range between 1400 and 1600 cm^{-1} . The asymmetric peak in spectrum e (2 ML) is assigned to a mode with A_g symmetry. This Raman-active mode, which is normally symmetry forbidden in HREELS, is activated due to interfacial charge transfer. In a simple picture vibrations of the flat-lying NTCDA molecule lead to a charge redistribution between molecule and surface leading to a dynamic dipole moment perpendicular to the surface [142]. Thus, a loss peak becomes observable in dipole scattering. The same mechanism was found for the very similar molecule PTCD (3,4,9,10-perylene tetracarboxylic acid dianhydride) on Ag(111) where this loss is also only observed in the monolayer regime [143–145]. Thus, this asymmetric peak may well be attributed to the presence of NTCDA monolayers in the samples and therefore it can be concluded that the films preferentially grow in the Stranski-Krastanov mode. This is also consistent with the other observations, e. g., that the intensity around 1550 cm^{-1} in the 3 (6) ML film is clearly stronger for higher growth rates. The latter observation can be explained by a higher nucleation density of smaller bulk-like islands. Lower growth rates result in a smaller number of larger islands. Both situations fit to the appearance and intensity of the low-energy losses attributed to bulk phonons.

Note, that the unexpected overall intensity ratio of the two 3 (6) ML films could be due to either small deviations from the exact 1:10-ratio in the evaporation rate or to different sticking coefficients. It should also be mentioned that for LT film no similar influence of the growth rate on the vibronic excitations was detected.

Electronic excitations

In Fig. 5.16 the electronic excitations are compared from the Ag(111) substrate (a) with those from different NTCDA RT films (b – f) and a 10 ML film prepared at 180 K (g). For an electron kinetic energy of 20 eV the surface plasmon of the pure Ag(111) surface is observed at 3.88 eV. The difference to the reported value of 3.9 eV [146] is due to the chosen scattering

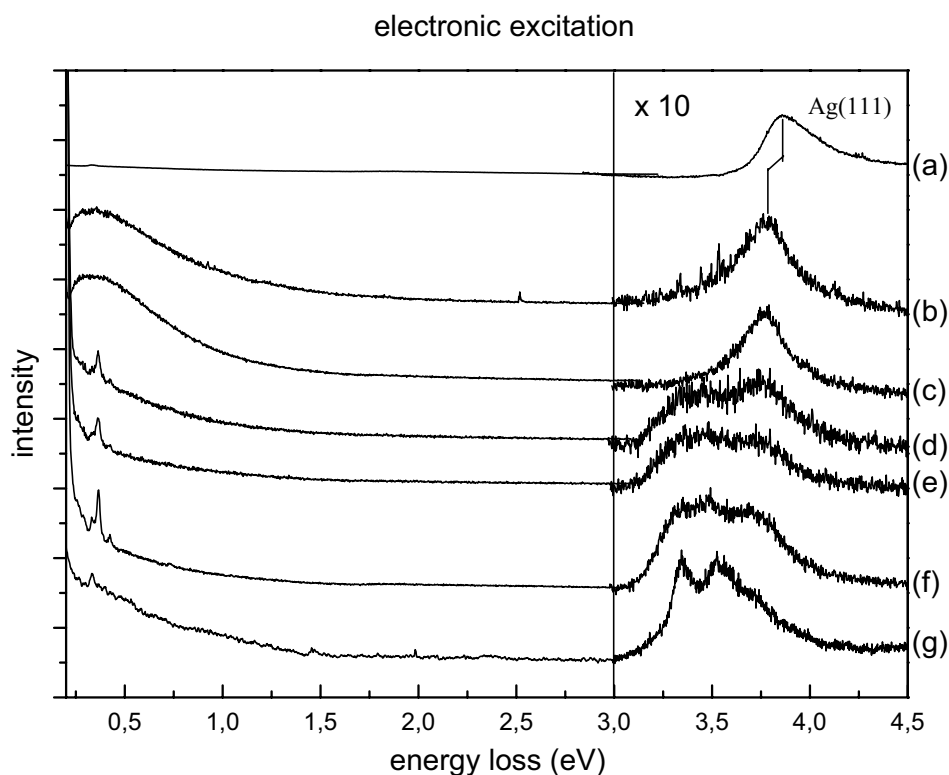


Figure 5.16: Electronic excitations from a pure Ag(111) surface (a) and for NTCDA films recorded by HREELS (primary electron kinetic energy: 20 eV). The thickness of the room temperature grown film was varied from 0.4 ML (b), 3 ML (c), 6 ML (d), 18 ML (e) to 30 ML (f). The lower spectrum (g) was recorded for a 10 ML film grown at 180K.

condition which leads to a parallel component $q_{||}$ of the scattering vector. Therefore a shift in the dispersion of the plasmon by 0.02 eV occurs. Upon NTCDA adsorption the Ag surface plasmon is attenuated as expected. Its energy is shifted by 0.2 eV to lower energies for which two explanations can be offered. First reason could be a change of the dielectric constant upon absorption of the NTCDA molecules. Second reason could be a reduction of the surface charge density due to a charge transfer to the chemisorbed NTCDA molecules.

With increasing NTCDA film thickness additional loss features appear near the still visible plasmon loss. For all NTCDA multilayer spectra a resonance

at 386 meV (3114 cm^{-1} , corresponding theoretical value (see table 5.5): 3150 cm^{-1}) is visible. This is a C-H stretching mode which is only weakly sensitive to dipole scattering. Therefore it is not visible in the 2.3 eV spectra but for 20 eV excitation. Again the in-plane vibration leads to lower intensity for the LT films due to the surface selection rule (spectrum g).

In Fig. 5.16 f (30 ML RT film) a broad structure at 3.5 eV which has some poorly resolved fine structure peaks (Peak A at 3.33 eV, Peak B at 3.49 eV, and Peak C at 3.78 eV – A, B and C) is shown. These features correspond to HOMO to LUMO excitations of NTCDA. A value of 3.95 eV is reported from the combination of ultraviolet photoemission (UPS) and inverse photoemission (IPES) using peak onsets to deduce the HOMO-LUMO gap [147]. The optical gap was reported to be at a value of 3.3 eV in literature [148]. DFT calculations yield excitation energies for the free molecule at 3.40, 3.43, 3.58, 3.78, 3.96 and 4.21 eV, however only the 3.40 and 3.78 eV excitations have a non-vanishing intensity [149].

The spectrum of the LT film (spectrum g) shows much clearer peaks compared to the thicker RT films (spectra d – f). Since at 298 K low-energy eigenmodes in NTCDA are already populated, RT films have thermally broadened structures in the electronic excitation spectra. In addition, a blue shift of the excitation energies is observed for flat-lying molecules in the LT film. In spectrum (g) peaks A and B are detected at 3.37 eV and 3.55 eV, which corresponds to energy shifts of 0.04 and 0.06 eV, respectively.

These variations are most probably due to different molecular orientations and conformations. For RT films the molecules crystallize in a herringbone-like crystal structure of upright-standing molecules. In LT films the relative geometry as well as interlayer distances of the flat-lying molecules is unknown. Therefore, one may only speculate on the effect of intermolecular π -overlap which affects the electronic structure. This in turn affects the electronic band structure. The band width in NTCDA RT films is estimated to be in the order of about 0.4 eV [86]. Since furthermore the measured signal is integrated over the at least 6 symmetry-equivalent domains the observed broadening becomes plausible. For LT films no dispersion is expected due to the lack of long-range order and therefore one observes molecular orbitals which are just perturbed by the interaction with neighbouring molecules.

Conclusions

In the present section the assignment of vibronic excitations has been used to determine the orientation of NTCDA molecules in differently prepared multilayer films. Since HREELS is extremely surface sensitive, only the outermost layers are probed. The symmetry of the vibrational modes gives an unambiguous indication for the molecular orientation. The present HREELS experiments give a clear indication, that the NTCDA molecules in RT multilayer films have their molecular plane almost perpendicular to the substrate, which is consistent with previous NEXAFS results [66]. In addition, the present HREELS data give clear indications, that the molecules are oriented with their long axis parallel to the substrate. Since NEXAFS only probes the orientation of unoccupied molecular orbitals (either π^* - or σ^* -orbitals), NEXAFS cannot distinguish between the short or long molecular axis.

For LT films flat-lying molecules are detected. Moreover, HREELS gives information about the external vibrational modes, i.e., phonons. The related low-energy bands vary for differently prepared films. RT multilayer films with bulk-like conformation of the NTCDA molecules show more pronounced phonon bands, whereas in LT films these modes are smeared out. This finding, together with substantially suppressed reflectivity and larger FWHM of the reflected electron beam for LT film indicates less structural order. This is also in accordance with the fact, that no structural order is observed for LT films in low-energy electron diffraction (see Chapter 5.7). In addition, the observation of features which should only be present in monolayer films (see 5.15) indicates Stranski-Krastanov type growth mode for high deposition rates. It seems to be more pronounced in RT films than in LT films. From the investigation of the electronic transitions a stronger π -overlap in the RT prepared films resulting in a lower energy gap can be deduced.

Table 5.5: HREELS resonances measured for NTCDA multilayers prepared on Ag(111) at different substrates temperatures in comparison and their assignment and symmetry. The first and second column list the resonances measured for preparations at 300 K and 180K, respectively. The assignment is based on the comparison with DFT results obtained for the free NTCDA molecule.

HREELS $T_{sub}=300K$ (cm^{-1})	HREELS $T_{sub}=180K$ (cm^{-1})	assignment
74		Phonon or B_{3u}
112	124	Phonon
136	124	B_{3u}
194	204	
225		B_{2u} +Phonon
291		combination
375	375	B_{1u}
445	435	B_{1u}
544	544	B_{1u}
597		B_{1u}
698	698	B_{2u}
725		B_{1u}
758	763	B_{3u}
818		B_{1u}
884	896	B_{3u}
942		B_{2u}
1040	1029	
1125		
1161	1146	B_{2u}
1236	1241	B_{2u}
1297	1302	B_{2u}
1383		B_{2u}
1438,52		B_{1u}
1513		B_{2u}
1579		B_{1u}
1773		
1785	1782	

5.6 HREELS investigations of NTCDA/Ag(111) monolayers

In the previous chapters, the physics of multilayer NTCDA films was addressed, where in Chapter 5.5, first monolayer measurements were introduced. The present chapter is dedicated to the monolayer results achieved for NTCDA/Ag(111).

Organic bulk crystals are known to exhibit relatively large charge carrier mobilities, which are often anisotropic with preference in the direction of the π system and have interesting optical properties like complete tunability and very high efficiency. Both properties strongly depend on the crystal quality [150, 151]. For high quality organic thin films, an epitaxial growth is highly desirable in most cases. However, organic thin films do not usually grow in crystalline structure directly on an inorganic substrate because the properties of substrate and organic material are too different. Moreover, in most cases, an intermediate layer forms at the interface which has different properties.

For commensurate monolayer superstructures, an epitaxial film growth may occur [82, 121]. This interface may also have a pronounced influence on the charge carrier transport when the film is used in a device. Therefore a detailed knowledge of the structural and electronic properties of the interface layer is an important piece of information. For the present study, high resolution electron energy loss spectroscopy (HREELS) was chosen. In particular, it is well suited for monitoring vibronic and electronic excitations of identical sample preparations and can cover the whole range of questions from submonolayer to multilayers.

NTCDA (1,4,5,8 Naphthalene-TetraCarboxylic acid DiAnhydride) monolayers on Ag(111) are investigated in this chapter as example for the interaction of large organic molecules with a metal substrate. The monolayer spectra discussed in this chapter reveal a rich structure which cannot be interpreted by only taking the expected infra red active vibrations into account. A detailed analysis of special, symmetry forbidden vibrations that are observable due to certain boundary conditions will be given together with the electronic excitation of the films. Additionally, the influences of a phase transition will be discussed in detail with respect to vibronic and electronic features of EEL spectra.

For known details about NTCDA monolayers, see Chapter 3.1.2. These monolayers have been extensively studied with various methods like SPALEED, XPS, NEXAFS, and STM [47, 66, 129, 152]. Independent of the

coverage, a fourth completely disordered phase was found in SPALEED upon cooling the sample to 150K [47, 128, 153]. The focus of this chapter will be on the vibronic and electronic excitations of the known relaxed monolayer (RM), the compressed monolayer (CM), and the low temperature phase.

Experimental details

For details about the sample preparation and the measurement setup, see Chapter 5.4. The NTCDA monolayer can be achieved in two different ways: either by direct deposition of a given amount of molecules or by thermal desorption of multilayer films. For the preparation of the relaxed monolayer a multilayer sample was annealed 15 min at 430K and for the preparation of the compressed monolayer, for 10 min at 430K.

In specular geometry, HREELS detects predominantly infrared active modes, and the surface selection rule has to be taken into account. Dynamic dipoles oriented parallel to the surface are screened by an image dipole within the metal substrate leading to a drastic reduction of the corresponding loss peaks in HREELS spectra. In contrast, perpendicular orientation of the dynamic dipole is accompanied by increased intensity of the loss peaks, as the image dipole enhances the dipole far field.

Results and discussion

The two different monolayer preparation methods mentioned above lead to identical spectroscopic results. Therefore all spectra presented here were measured from monolayer films prepared by annealing. The preparation of the relaxed monolayer (up to 0.8 ML) is straightforward. As soon as the appropriate LEED [46] pattern of the monolayer is visible, the annealing can be stopped. The compressed monolayer (0.9-1 ML) needs additional care when the LEED pattern becomes visible. The reason is that multilayers grow in the Stranski Krastanov mode and hence the monolayer diffraction pattern is already observable when multilayer islands are still found on the sample.

In the following, first the focus will be on the electronic excitations in a monolayer and compare them with those of the clean Ag(111) surface. Then the vibrational excitations in a monolayer are addressed. The observed vibrational modes will be assigned with special emphasis on normally forbidden totally symmetric modes. Finally, the influence of an interesting phase transition upon vibronic and electronic spectra will be discussed.

Electronic excitation of the monolayer

In Fig. 5.17 spectra taken at 20 eV primary electron energy are plotted. The clean Ag(111) surface (a) reveals the Ag surface plasmon at 3.88 eV which is here shifted by 20 meV with respect to the known literature value of 3.9 eV. A reason for this very small difference could be that the actual scattering conditions do not allow to measure at the gamma point but at a different point in the plasmon dispersion curve ($q_{||} = 0.2 \text{ \AA}^{-1}$). The asymmetry of the peak is known and is attributed to either multipole plasmons or interband transition according to Ref. [154].

A 0.5 ML NTCDA film induces several changes in the electronic spectrum. The surface plasmon peak is attenuated, as expected, and shifted by 80 meV to lower energies (3.80 eV). This might be due to a change of the dielectric constant in the upper half space due to NTCDA adsorption or to a reduction of the surface charge density due to a charge transfer between Ag surface and molecules.

In the low energy range a structure is found at 0.35 eV which is completely new also when compared to known multilayer features (see chapter 5.5). The multilayer peaks assigned to HOMO-LUMO excitations cannot be observed in this case. In order to explain the feature at 0.35 eV with its unusual intensity reference to results achieved by other methods will be used. NTCDA is known to chemisorb on the Ag(111) surface as derived from UPS, XPS and NEXAFS [47, 48, 128] measurements. Photoemission and NEXAFS reveal strong spectroscopic changes leading unambiguously to the conclusion that chemisorptive bonding occurs mainly mediated by the molecular π system, located at the naphthalene core, to surface orbitals.

As the work function is known to remain almost unchanged [49] the peak shifts in the XPS and NEXAFS are explained by the chemical bonding (initial state effect) and by a dynamic charge transfer into the molecule (charge transfer screening) [155]. By UPS an electronic state near the Fermi level was found [47], which is cut by the Fermi level. This has also been shown by recent high-resolution measurements [156]. UPS furthermore leads to the conclusion that this molecular orbital is mainly derived from the LUMO but has a contribution from Ag 4s states leading to a partially filled molecular orbital [145]. Since the LUMO is mostly on the naphthalene part, this means a direct bonding between Ag and naphthalene core. And since this orbital is only partially filled this means a metallic molecular interface. Already for graphite as substrate a shifted LUMO has been observed in STM for a NTCDA monolayer [152]. These findings are consistent with our measured data if we interpret the peak at 0.35 eV as follows: If the $C P_z$ derived

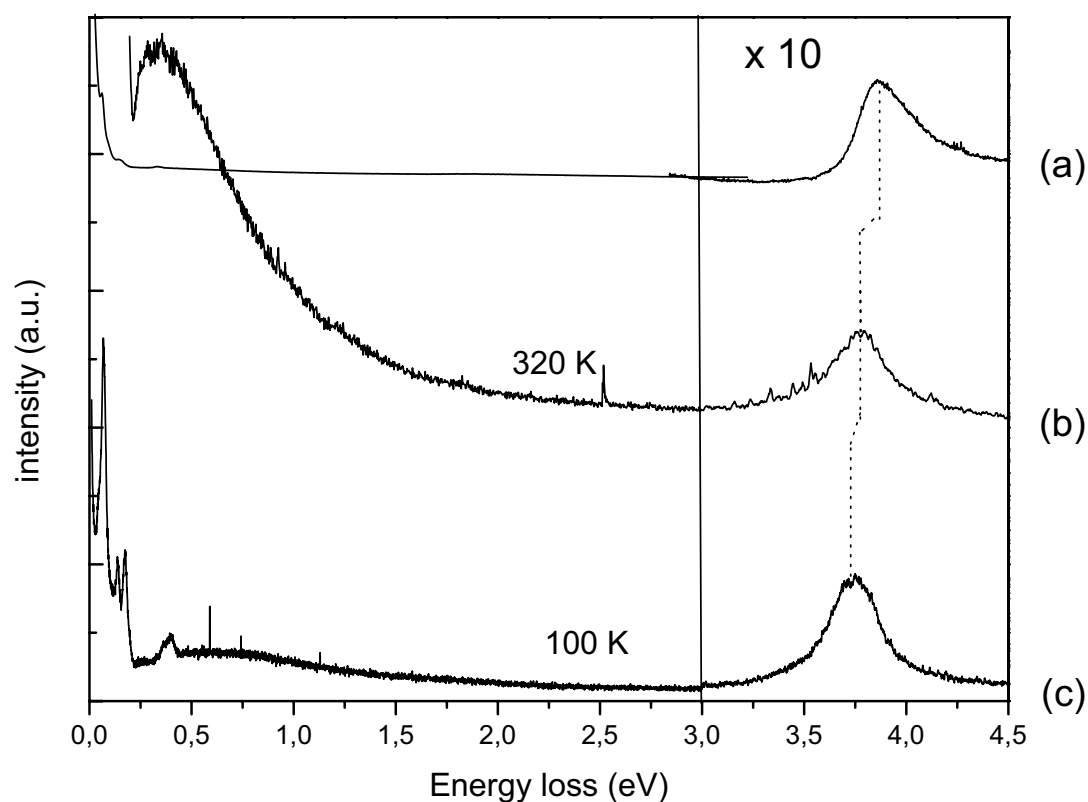


Figure 5.17: Electronic excitation spectra measured with 20 eV primary electron energy. Above 3 eV the intensity is enhanced by a factor of 10 for all spectra. (a) Spectrum of the clean Ag(111) surface with a surface plasmon at 3.85 eV, (b) spectrum of a 0.8 ML NTCDA/Ag (111) film with pronounced features at 3.78 eV and 0.35 eV, in (c) spectrum of a 0.8 ML film after the low temperature phase transition has occurred.

LUMO hybridizes with the Ag 4s states, a bonding and antibonding orbital are formed. UPS and NEXAFS measurements yielded intensity, right at the Fermi level indicating that the bonding part of this hybrid orbital is below E_F and the antibonding above. The peak at 0.35 eV is thus interpreted as transition between these two orbitals showing that they are just 0.35 eV apart (and hence overlap) and that they have different symmetry character. It is likely that the lower is predominantly derived from s-states while the upper from p-states.

Thus the peak at 0.35 eV is found there because of the chemisorptive bonding. Thus the Ag(111) surface provides a static charge transfer, i.e., doping, of the molecules in the interface. Furthermore, as will be pointed out below, the electron reservoir provided by the Ag surface is the origin for dynamic charge transfer between molecules and Ag surface.

Vibronic excitation of the monolayer

The comparison of a relaxed and a compressed monolayer spectrum (not shown), did not reveal obvious differences (2.3 eV primary electron energy, resolution 23 cm^{-1} , normalized to the elastic peak). Both spectra show identical loss features at the same energy positions. Only the intensity is slightly different which can be attributed to the different coverage of the surface as it is expected to be proportional to the intensity [15]. According to the surface selection rule only vibrations leading to a dynamic dipole perpendicular to the surface should be visible in specular geometry. As NTCDA belongs to the D_{2h} symmetry group and is known to adsorb flat on a Ag(111) surface the out-of-plane modes with B_{3u} symmetry (calculated at 80, 125, 193, 541, 751, 879 cm^{-1} , see chapter 5.4 for details) are expected in the spectrum, and some of them are indeed observed at 89 (80), 205 (193), 540 (541) and 751 (751 cm^{-1}) (see Fig. 5.18). However, some losses with high intensity are found above 900 cm^{-1} while the calculation predicts no infra red active out-of-plane modes at higher energy. Therefore the question for the origin of these losses arises.

Due to the adsorption on the surface some bonds may be twisted out of the molecular plane (i.e. C-H or C=O bonds) which could lead to a dynamic dipole perpendicular to the surface. According to NEXAFS measurements the adsorption of the molecule is flat. XSW (X-ray Standing Waves) [157] studies indeed reveal a small bending of the anhydride groups which might result in observable C=O vibrational modes. Nevertheless, this angle is too small for a considerable resulting dynamic dipole moment perpendicular to the surface, and the observed asymmetric modes do not fit to known infra

red modes when peak profile and energy positions are taken into account. Therefore intensity induced by the distortion of the molecules is neither expected nor observed. Upright standing molecules at surface steps might be another explanation for the observed loss peaks. But energy positions and peak shapes for upright standing molecules are known (see chapter 5.4) and do absolutely not agree with the measured asymmetric peaks. An additional experiment with short annealing periods after sputtering to produce defect/step richer surfaces did not lead to significant spectral changes as long as diffraction patterns could be observed. Therefore it is unlikely that the observed high energy losses are due to molecules at steps or defects.

Due to the absorption of the molecules, the symmetry group D_{2h} should be reduced to D_2 or more likely to C_i as there is no longer a 2 fold rotation axis perpendicular to the molecular main axis. This leads to additional infrared active modes as group theory predicts that formerly B_{ig} ($i=1,2,3$) and $A_{u/g}$ modes can become infra red active. Therefore the out-of-plane modes B_{1g} , B_{2g} and A_u could become visible in the HREELS spectrum. The predicted energies for B_{1g} (80, 433, 719, 879 cm^{-1}) and B_{2g} (131, 237, 463, 693, 837, 988 cm^{-1}) are also plotted in Fig. 5.18 as triangles. Within this framework the loss at 984 cm^{-1} fits well to the B_{2g} mode at 988 cm^{-1} in D_{2h} symmetry. But overall hardly any intensity is found near the calculated B_g modes which makes them unlikely as an explanation. Additionally the B_g are often very close to active B_{3u} modes. Above 1000 cm^{-1} only parallel polarized vibrational modes are expected as result of DFT calculations. Therefore no vibrational losses resulting from out-of-plane modes are expected above that energy, and hence another mechanism must be responsible.

Discussion of the forbidden A_g modes and their lineshapes

For PTCDA/Ag(111) an almost identical behavior was already found, the losses were proposed to be detectable by an activation of A_g modes [145]. The physics responsible for this activation and the adaptability of this model for the NTCDA/Ag(111) monolayer will be explained briefly now.

A coupling between the totally symmetric in-plane molecular A_g vibrations and a charge transfer perpendicular to the surface, between molecule and substrate, leads to the activation of these modes. Such an effect is known as interfacial dynamic charge transfer [158]. In Ref. [145] a detailed theoretical explanation is given leading to a formula describing the high energy asymmetric loss peaks. It is based on former work where already for dimerised linear chains in condensed material [159–161] an infra red activation of totally symmetric modes with asymmetric line shapes was observed [162]. The

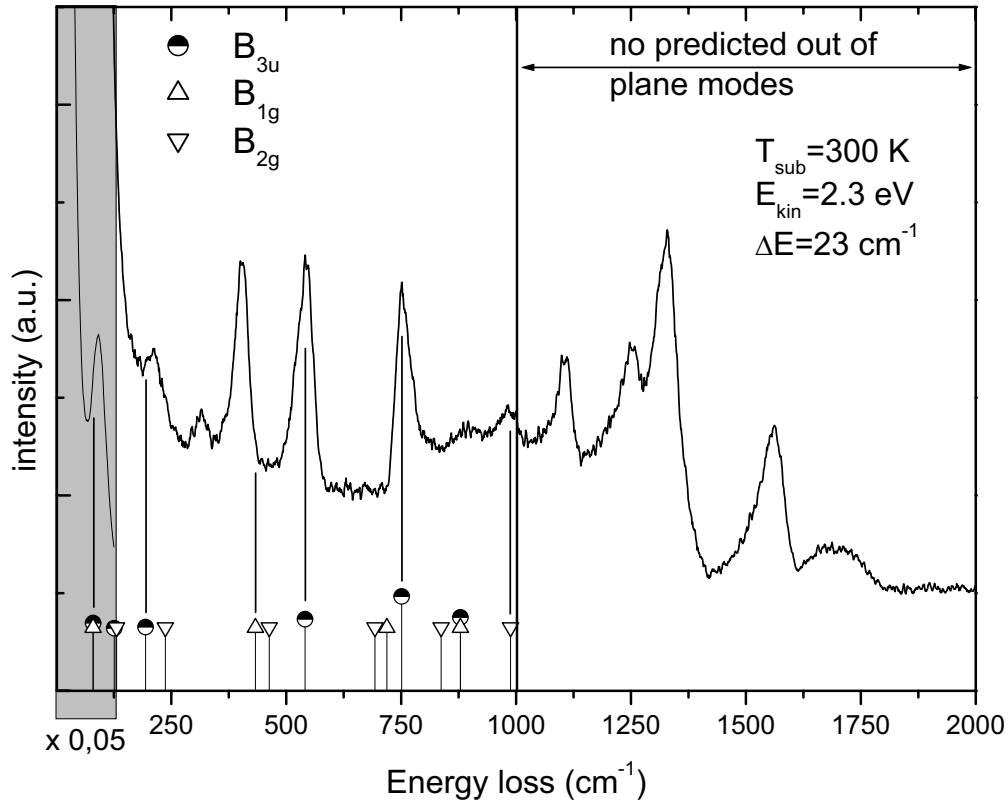


Figure 5.18: HREELS spectrum of a 0.8 ML NTCDA/Ag (111) monolayer film measured with 2.3 eV primary electron energy and a resolution of 23 cm^{-1} . For flat orientation, B_{3u} modes are expected to be HREELS (IR) active; these are marked by half filled circles. Due to symmetry breakdown possibly observable B_{1g} and B_{2g} modes are highlighted by empty triangles. Above 1000 cm^{-1} no out-of-plane vibrations and therefore no intensity is expected.

model is based on linear response theory for a discrete oscillator (the vibrational level) being coupled to a continuum of states (the low energy electronic state). The derived formula for the dielectric response function is

$$\epsilon(\omega) = \epsilon_{\infty} + \frac{4\pi\xi_1(0)\omega_{CT}^2edN}{\omega_{CT}^2[1 - \lambda_{\alpha}D_{\alpha}(\omega)] - \omega^2 - i\omega\gamma}$$

with

$$D_{\alpha}(\omega) = \frac{\omega_{\alpha}^2}{\omega_{\alpha}^2 - \omega^2 - i\omega\Gamma}$$

being a dimensionless phonon propagator and

$$\lambda_{\alpha} = \frac{2g_{\alpha}^2}{\omega_{\alpha}}\rho(E_F)$$

a dimensionless coupling constant. $\xi_1(0)$ is the susceptibility at $\omega=0$, $\rho(E_F)$ the density of states at the Fermi level, g_{α}^2 the coupling constant between molecular vibration and charge transfer, ω_{CT}^2 the frequency of the charge transfer oscillations, d the spatial amplitude of the dynamic charge transfer, e the electron charge, N the electron density, and ω_{α} the frequency of the Ag modes “for the undisturbed free molecule”. γ is the FWHM of the electronic background peak and can be extracted from a fit of the electronic background by a damped Lorentzian peak.

Within this model non infrared active modes become activated via the coupling of the dynamic charge transfer to a molecular vibration. After excitation there is a self interaction between charge transfer and vibration, i.e., a charge transfer excites a vibration and vice versa. The resulting self interaction series, which has to be summed up, leads to a Fano like lineshape. Using these results an analysis of the observed peaks within this framework by fitting the experimental data with Fano profiles is given. Detailed information can be drawn from the fit results regarding the coupling at the NTCDA/Ag interface. If the cited model is indeed a good description of the physics leading to the observed peak the model should also apply for the NTCDA/Ag case. A model function is used to reproduce the prominent features in the spectrum focusing on a good overall agreement and not focusing on details to avoid an overestimation of the model. In order to actually achieve the measured line shape, $\text{Im}(-1/\epsilon)$ has to be calculated [152].

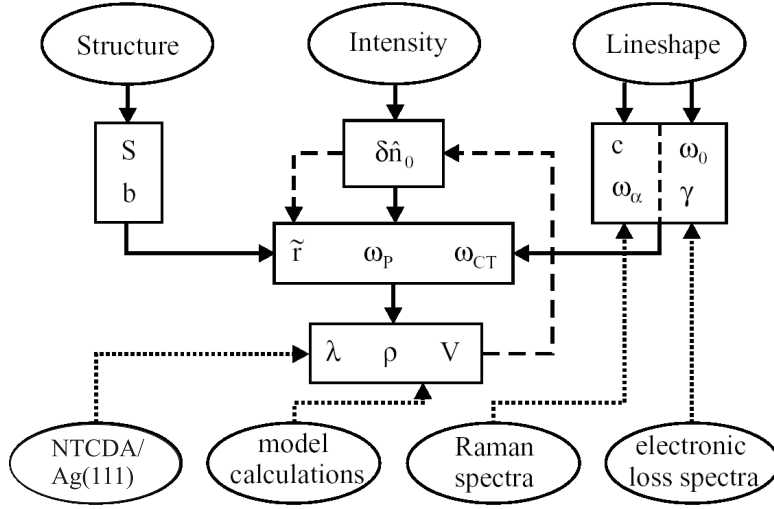


Figure 5.19: A simplified scheme of calculation and fitting of the A_g modes. ω_0 , γ , ω_α and c result from the fit of the vibronic and electronic spectra. S and b are independent results from LEED and XSW data. [164]

To fit the data, a background function (see Fig.5.21) has been taken into account. The elastic peak was extrapolated and subtracted from the spectrum where the region around 300 cm^{-1} is used as a fix point for the background function. All 5 resonances are fitted with Fano profiles using a self written root [163] script. The focus is set on resonances that clearly exhibit an asymmetric line shape. The remaining infra red peaks are fitted using a Lorentzian peak profile. For $\text{Im}(-1/\epsilon)$ an appropriate Γ was chosen as the elastic peak is much sharper than all peaks to be fitted.

In Fig. 5.19 a flow chart giving a general overview of the fitting process is displayed [164]. Extracting the parameters γ , ω_α , ω_0 and c is a crucial step when comparing the model function and the experimental spectrum. It turns out that the pair (c, ω_α) is a line shape invariant which is determined by the slope of the high energy side of the fano resonances. The parameter c is defined as $c = \lambda_\alpha \omega_\alpha^2 \omega_{CT}^2$. c is invariant to the exact shape of the electron-hole pair continuum.

The frequency ω_α can be extracted very reliably from the fit procedure as the fit result is very sensitive to its variation. It has an error bar of $\pm 5 \text{ cm}^{-1}$ with respect to the resulting value.

The parameters γ and ω_0 are determined by the low energy tail of the asymmetric modes. The spectral function of the electron-hole excitation which

Table 5.6: A comparison of the values for ω_α with the actual peak positions and energies for the A_g modes as predicted by DFT calculations. The resulting coupling constant λ_α is also included.

ω_α -fitted cm^{-1}	DFT cm^{-1}	peak position cm^{-1}	λ_α
1160	1022	987	≈ 0.22
1260	1223	1103	≈ 0.19
1287	1287	1254	≈ 0.13
1456	1461	1330	≈ 0.34
1621	1652	1562	≈ 0.19

results from the values of γ and ω_0 , is displayed in Fig. 5.20. The displayed curves cannot be compared quantitatively as the vibrational modes are fitted for 2.3 eV primary energy whereas the actual spectrum displayed was taken with an energy of 20 eV in order to be able to collect the spectrum up to 8000 cm^{-1} including vibrational losses below 2000 cm^{-1} . It shows the broad electronic background which is centered around 0.35 eV. Extrapolating the electronic background yields the information that the vibronic losses are superimposed on it. The shape of the curve suggests that it can be modelled with a strongly damped Lorentzian peak centered at 0.35 eV. The resulting values for FWHM and peak maximum are $\gamma=0.2 \text{ eV}$ and $\omega_0=0.35 \text{ eV}$, respectively. Energy-dependent cross sections and the spectrometer transmission function are the reason why the 2.3 and 20 eV spectra can only be compared qualitatively, since they cause deviations in intensity for the electronic transition state as seen in Fig. 5.20. Moreover it is obvious that the experimental ω_0 loss is more complex than a Lorentz profile. Nevertheless for the sake of simplicity a Lorentz peak profile is a good approximation.

The result of the fit procedure is shown in Fig. 5.21 which has been achieved with the parameters discussed above. It is in good agreement with the experimental result. The Fano profiles are well reproduced with respect to both, the asymmetric line shape and the dip on the high energy side of the profile, as especially seen around 1430 and 1610 cm^{-1} . The dips are due to the non-adiabaticity of the self interaction series for the electron vibron coupling. The sum of the Fano profiles as achieved is additionally plotted under the spectrum. The losses at 402 , 541 and 754 cm^{-1} were fitted using Voigt peak profiles after all A_g modes were fitted.

The limitations of the applied model can be seen in the model spectrum around 1030 and 1160 cm^{-1} where the dip on the high energy side of the

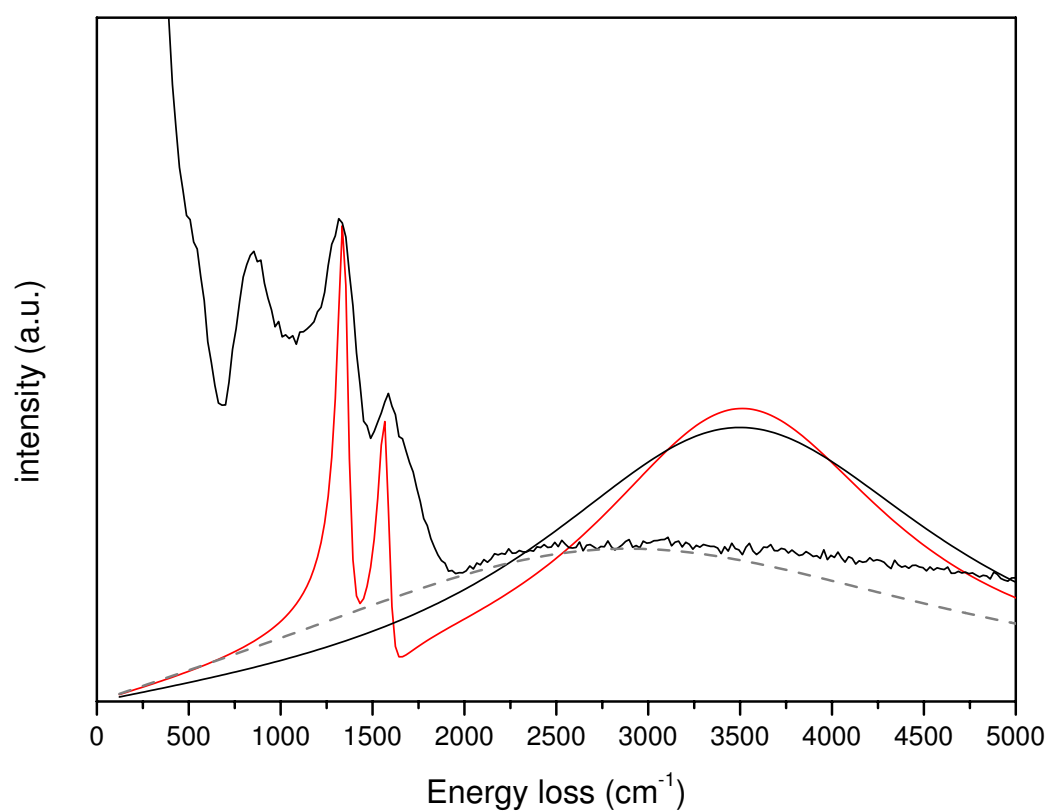


Figure 5.20: Comparison of a specular EELS taken at 20 eV with a calculated spectrum. The background used in the quantitative analysis is also plotted (black line) and can be compared to the actual background for this energy plotted as dashed line. The result for two Fano profiles including the background is also shown (red line)

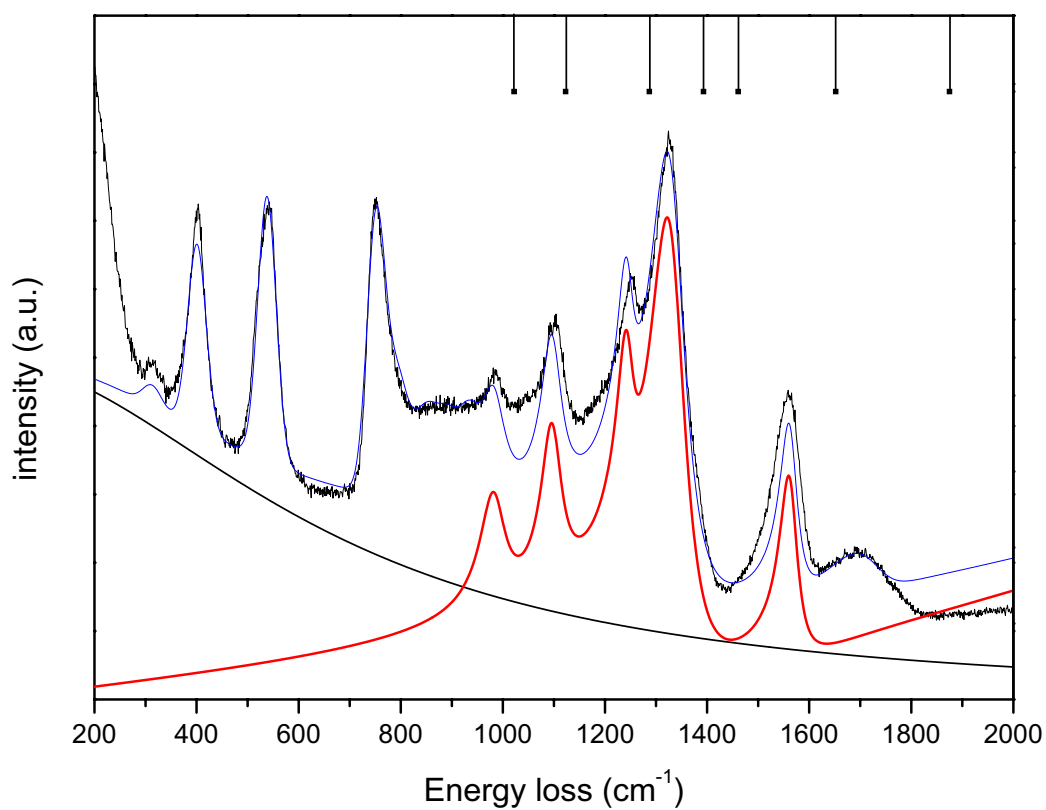


Figure 5.21: The resulting calculated spectrum (blue) compared with the experimental HREELS spectrum (black). In addition the applied background for the elastic peak (smooth black line) and a sum of all Fano profiles (red) is plotted. In the upper part the energy positions of calculated A_g modes is included as bars.

Fano profile is overestimated. Also the Fano profile at 1560 cm^{-1} has some deviations from the measured spectrum. This is the result of both the constraints that all profiles share and of the boundary condition to still achieve a reasonable model function for the electron-hole pair continuum (see Fig. 5.20).

The according to DFT highest energetic A_g mode at 1875 cm^{-1} has no obvious counterpart in the spectrum. It is most likely contributing to the broad feature at about 1700 cm^{-1} , but can not be modeled with a reasonable parameter set. Therefore it is assumed that the coupling of this mode is out of the scope of the applied model.

Turning back to the flowchart in Fig. 5.19 we can start to use the derived parameters γ , ω_0 , ω_α and c to obtain the further parameters λ , ρ . This will lead to the intramolecular coupling constant V_α defined as $V_\alpha = \lambda/\rho$. In order to achieve this, the charge transfer frequency ω_{CT} and the plasma frequency ω_p are needed. They are related to ω_0 by $\omega_0^2 = \omega_p^2 + \omega_{CT}^2$. Therefore further input parameters are necessary, which are the area of the surface unit cell $S = 157\text{ \AA}^2$ (taken from LEED or STM data [46, 47]) and the distance b between the Ag substrate surface and the first molecular layer. This value was derived by XSW measurements that result in a distance of 3.02 \AA of the molecules above the surface for the relaxed monolayer [157]. The dynamic dipole moment $\delta\hat{n}_0$ can be estimated from the relative intensity of the loss peaks using dipole scattering theory [15]. Some additional assumptions with respect to the dynamic charge transfer amplitude d need to be done to achieve the dynamic charge transfer $\delta\hat{n}_0$.

As mentioned, in order to determine $\delta\hat{n}_0$ an independent value for d is mandatory. Moreover uncertainties regarding the intensity ratio I_{inel}/I_{el} and the high background of the profiles complicate this issue. Additionally the analyzer acceptance angle, which also affects the measured intensity is difficult to be quantified exactly. With all these uncertainties $\delta\hat{n}_0$ is consistent with values in a range of 0.1 to 1.0. In order to achieve a better estimate without all these difficulties an alternative way is chosen. $\delta\hat{n}_0$ and d are both varied as input parameters to calculate λ_α , $\rho(E_F)$ and V_α . The resulting molecular bandwidth $W = 1/\rho(E_F)$ is restricted to $0.5\text{ eV} < W < 1.5\text{ eV}$ and $V_{total} < 170\text{ meV}$ (for $0.7 < \delta\hat{n}_0 < 0.9$). The lower limit of W is reasonable as it follows from the observation of the maximum electronic excitation spectrum, while the higher value is given by the weak intermolecular wave function overlap in molecular crystals. The limit for V_{total} is consistent with calculations for electron phonon coupling energies of organic molecules [165]. With $\delta\hat{n}_0$ fixed in this range the experimental intensity can be used to derive the charge transfer amplitude as $d = 0.4\text{ \AA}$. This finally yields to the desired coupling

constant λ_α for electron phonon coupling and the Fano profiles, which is included in table 5.6 and lies between 0.13 and 0.34.

The applied theory function leads to both the asymmetric lineshape and a shift of the peak energy to lower energies. In table 5.6 the results comparing the derived energies for ω_α with peak positions and results of DFT calculations are collected. The shift of the frequencies of the non-interacting modes relative to the observed ones is directly linked to the coupling strength λ_α . The values for the non-interacting frequencies ω_α that were independently derived from external input correspond not only very good to the calculation but also to results from Raman measurements [141].

The coupling constant for electron-phonon coupling should be correlated with the actual vibration of the molecule. The more the naphthalene core, which is predominantly involved in the bonding to the surface, is participating in a vibration the more charge will be squeezed out of the molecular plane. This correlation can be seen in appendix B, where the A_g modes are plotted in their extremal positions. Especially the modes at 1461 and 1652 cm^{-1} exhibit strong contributions of the naphthalene core to the vibrations, whereas for the modes 1022, 1123 and 1287 cm^{-1} the vibrational elongations are considerably smaller.

In this subsection the electron-phonon coupling was quantified spectroscopically due to the observation of the usually symmetry forbidden A_g modes. The theoretical model used originally to interpret PTCDA/Ag(111) monolayer experimental findings was successfully applied to the system NTCDA/Ag(111).

From monolayer to multilayer films

In Fig. 5.22 a multilayer HREELS spectra along with bilayer and monolayer spectra are plotted for both, room (RT) and low temperature (LT) films. Please remind that multilayer NTCDA/Ag(111) films are known to form islands, i.e. have a Stranski Krastanov growth mode, therefore the spectra (b)(ii) do not represent completely closed bilayers but are the result of the superposition of monolayer and starting island growth. The multilayer spectra in Fig. 5.22(a),(i) were discussed in detail in Chapter 5.5.

The discussion will start with peaks typical for the submonolayer. The strong A_g modes at 1330 and 1560 cm^{-1} are also observed in the bilayer, where in the case of peak 1330 cm^{-1} already a superposition with a B_{1u} multilayer peak at 1297 cm^{-1} is observed for both, RT and LT films. The A_g mode at 1560 cm^{-1} has a reduced intensity and on the high energy side around 1800

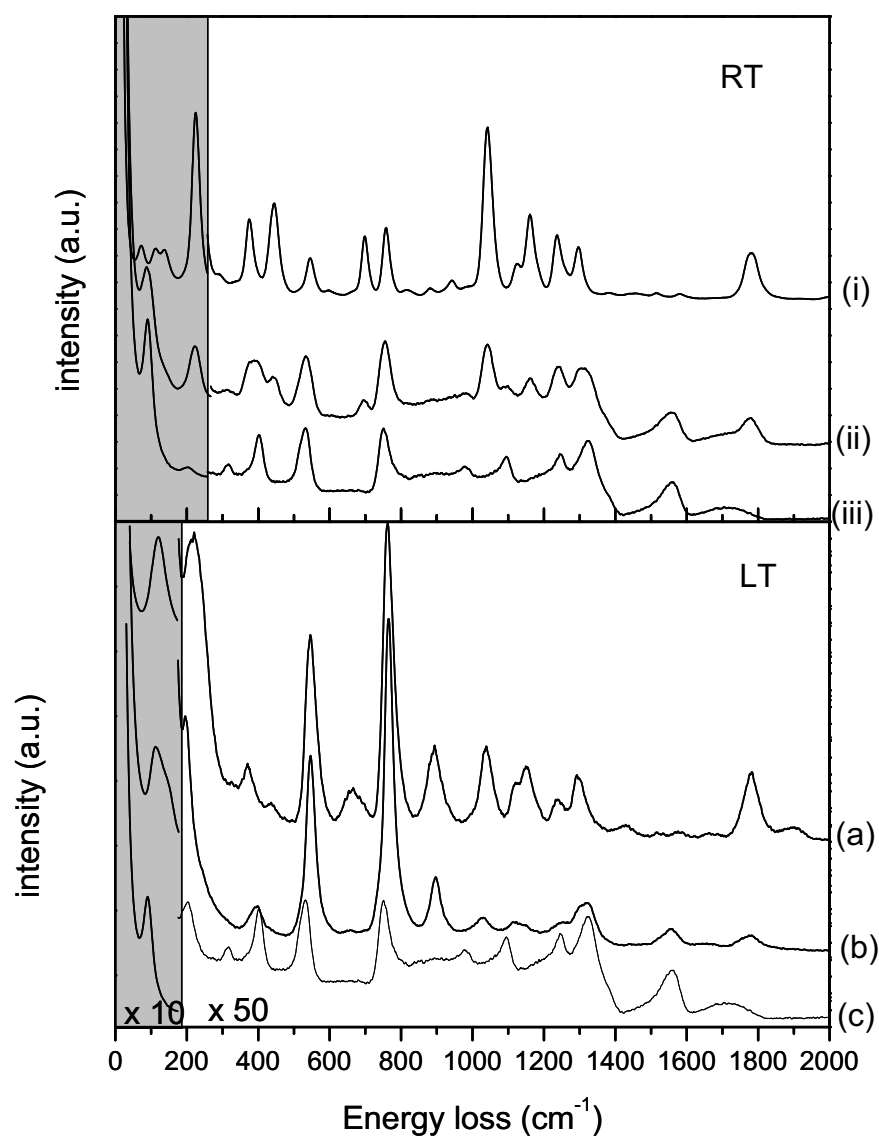


Figure 5.22: Comparison of multilayer (a,i), bilayer (b, ii) and monolayer (c, iii) spectra for preparation at room (i-iii) and low temperature (a-c). The lower spectra (a-c) represent vibronic spectra of films grown at 200K, the upper spectra (i-iii) at room temperature.

cm^{-1} the C=O stretch mode is already observed in spectrum (b)(ii). The weak A_g modes at 980 and 1100 cm^{-1} are still observed in the RT bilayer but not in the cold bilayer where they are already below the detection limit. This can be taken as an indication for a reduced mobility when growing thin films leading to a more closed film in the case of the low temperature substrate. The monolayer peak at 1251 cm^{-1} , previously assigned to an A_g mode, also seems to be observed in the RT multilayer spectra though slightly shifted, which contradicts this assignment. But the multilayer peak can be assigned unambiguously to a B_{2u} mode, which is symmetrically forbidden in the monolayer. Moreover, the monolayer assignment is assisted by peak fitting and by the asymmetric peak shape. Therefore, a superposition of mono and multilayer features is most likely observed here. A similar case is found for the mode at 404 cm^{-1} , which is also restricted to the monolayer since the multilayer modes observed at 375 and 445 cm^{-1} in the bilayer have B_{2u} symmetry and are therefore predicted to be invisible in the monolayer due to the surface selection rule. Some modes start to be visible in the bilayer spectrum like 375, 445, 698, 1040, 1161, 1263, and 1297 cm^{-1} (the numbers here are for the RT film). Their appearance and different intensities regarding RT and LT films can be explained in the framework of the surface selection rule and are addressed in detail in Chapter 5.5.

A third category of modes are those which are found in mono- and multilayer spectra. The B_{3u} modes at 544 and 758 cm^{-1} (RT film) are observed and symmetry allowed in both, the mono and multilayer films. In the monolayer they are shifted by about 10 cm^{-1} to lower energies due to the influence of the A_g surface. Low energy B_{3u} molecular bending modes are found at 90 and 205 cm^{-1} in the monolayer spectrum. In the case of room temperature films, the observed low energy features are due to the formation of ordered islands (see Chapter 5.4). For the low temperature multilayer films, the B_{3u} mode at 90 cm^{-1} is no longer observed but another B_{3u} mode not visible in the monolayer at 119 cm^{-1} is observed in the spectrum. So overall, the bilayer is in both cases a superposition of mono and multilayer spectra which can be clearly assigned.

Low temperature phase transition

Upon cooling of the monolayer for both the relaxed and the compressed monolayer, a new phase is found which is, from a spectroscopic point of view independent of coverage. Cooling down to 155K within 15 min yields drastic changes within the vibronic and electronic excitation spectra (see Fig. 5.17 and 5.23). Additionally, there are changes which are not straightforward

seen in the spectra. The count rate for the elastically scattered electrons is decreased by a factor of 50 for the low temperature monolayer (i.e. the highest achieved count rate of elastically scattered electrons was 6000 counts/s, as compared to 300000 counts/s for the well-ordered monolayer structure). Also the resolution (FWHM) was reduced to a best value of 36 cm^{-1} after the phase transition, while in RT monolayer films 23 cm^{-1} was achieved. The phase transition is reversible: upon annealing the film known RT HREELS spectra and diffraction patterns reappear. It is emphasized that in order to achieve the transition, the according temperature has to be set precisely. For example, the room temperature phase also remains unchanged at low temperature when cooling rates are too high. Together with the reported hysteresis [35], this suggests that an activation barrier exists between the room and the low temperature bonding regime. Cooling a room temperature film fast to 100K while measuring for over 24 h (i.e., pumping energy into the system via the electrons) did not show any change in the spectroscopic features, i.e., no phase transition occurred.

The electronic excitation spectrum shows several changes due to the phase transition (see Fig. 5.17c). The peak of the Ag surface plasmon is shifted by 50 meV to lower energies, which according to the comparison of the clean and the monolayer surface, leads to the conclusion that the surface charge density has been further reduced. Therefore more charge is transferred from the surface into the molecules or is localized in the adsorbed bond. This is also in accordance with the change of the low-energy electronic excitation at 0.35 eV. This peak, observable in the room temperature monolayer due to a partially filled former LUMO orbital, almost disappears in the background, which indicates that the former LUMO is now completely filled.

Within the vibronic spectrum, the changes induced by the phase transition are also very strong as seen in Fig. 5.23(b) for the A_g modes. Modes which were previously explained by charge transfer between the surface and the molecule are almost gone. Only for the strongest A_g modes at 1327 and 1560 cm^{-1} is some intensity still found, which is most likely due to molecules that remain in the room temperature phase (e.g., at steps or defects). The strong change in the vibronic spectrum is consistent with the changes in the electronic transitions. As the former LUMO is no longer partially filled after the phase transition (see Fig. 5.17c), the mechanism responsible for activation of the A_g modes is no longer accessible. However, modes which are observable by their infrared activity in the room temperature film are still found in the spectrum after the phase transition. Only the B_{3u} mode at 540 cm^{-1} is drastically weakened after the phase transition, whereas all other modes only show small intensity changes. Indeed, the structure at

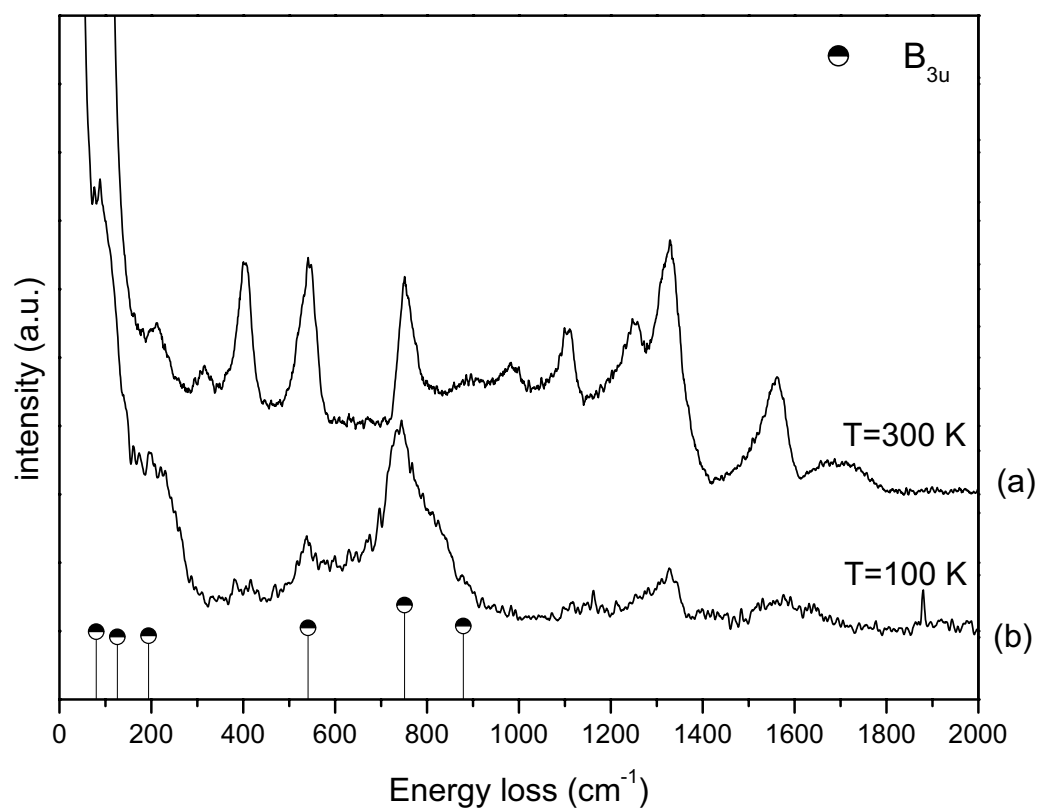


Figure 5.23: The known NTCDA room temperature monolayer (a) together with the vibrational spectrum after the phase transition to low temperature (b). The phase transition occurs at 155K while the measurement afterwards can only be taken at 100K. Energies for calculated B_{3u} vibrations are shown as half filled circle.

540 cm^{-1} might be due to a superposition of a B_{3u} and an A_g mode in the room temperature film, contributing only its B_{3u} component after the phase transition. On the high energy side of the peak at 751 cm^{-1} , a broad shoulder at 830 cm^{-1} is found after the phase transition. In principle this may arise due to two different effects. First, cooling the sample to 100K may lead to adsorption of molecules from the residual gas, i.e., H_2O , CO and CO_2 . Measuring with full cooling, i.e. at 100K after the phase transition is driven by the fact that measurements in the HREELS spectrometer are only reliable without annealing the sample during data taking. But direct cooling to low temperature without phase transition did not lead to this shoulder within 24h and therefore it is directly related to the phase transition. Secondly, the position of the peak fits to a calculated out-of-plane B_{2g} mode at 837 cm^{-1} , which can become infrared active via reduction of molecular symmetry D_{2h} to C_i . Consequently, other B_{1g} and B_{2g} modes should be found in the spectrum. Indeed, there might be a contribution of B_{1g} (719 cm^{-1}) and B_{2g} (693 cm^{-1}) modes to the broadening on the low-energy side of the peak at 751 cm^{-1} . For several other peaks, an assignment to B_g modes is only speculative since at almost the same energy position, B_{3u} modes are predicted, observed, and already assigned in the room temperature phase.

The described phase transition is not restricted to a perfect monolayer. For example, a compressed monolayer prepared by annealing already showed the corresponding LEED pattern, but in the vibronic spectrum, multilayer contributions were still observable. Nevertheless, the low-temperature monolayer phase transition could be achieved. In Fig. 5.24(b), the superposition of the known multilayer features and the low-temperature phase is shown. For comparison, the room temperature phase of the spectrum is plotted in Fig. 5.24(a) where the superposition of mono and multilayer is obvious (see Fig. 5.22). For example, in the latter film, the Fano modes, which are restricted to the RT monolayer, are seen at 1330 and 1560 cm^{-1} , while in the low-temperature spectrum, only the multilayer peaks like the C-O stretch mode at 1780 cm^{-1} are present in this range. Also, in the region around 400 cm^{-1} , the superposition of the two multilayer peaks with the monolayer peak is clearly visible in (a), while the RT monolayer peak disappears in (b). Thus it is obvious that spectrum (b) is the result of the phase transition. The Fano-shaped peak at 1560 cm^{-1} and the shoulder at 1350 cm^{-1} disappear, whereas the shoulder at 800 cm^{-1} discussed above is present in this spectrum. Taking the known Stranski Krastanov growth mode and the finding into account that the monolayer seems to be almost completely transferred into the low-temperature phase, it can be concluded that the phase transition at the interface can also occur in a densely packed film, already populated

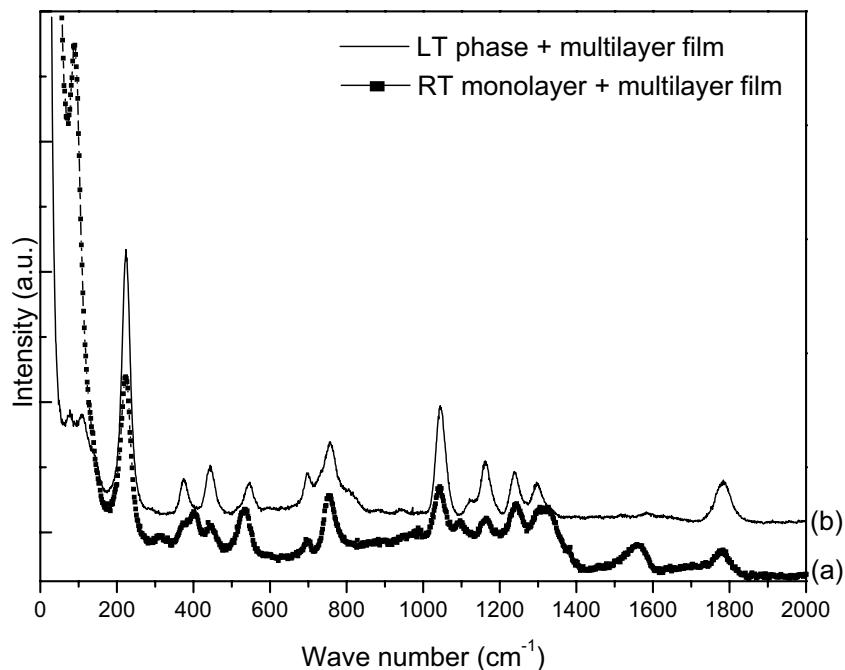


Figure 5.24: 2 ML NTCDA film at room temperature (a) shows the superposition of multilayer and monolayer features. After the phase transition (b) the multilayer features are observed together with the typical low temperature phase features, but the features typical for the RT monolayer film have disappeared.

with multilayer islands.

In [153], results addressing the phase transition for different spectroscopic techniques are summarized along with an explanation for this unusual finding of an order disorder phase transition upon cooling. A phase transition at constant pressure is driven by the gain in Gibbs free energy $\Delta G = \Delta H - T \cdot \Delta S$ (H is the enthalpy; S is the entropy). The molecule-substrate interaction is found to be stronger in the disordered phase, which is assigned to a more negative enthalpic contribution of H . The stronger binding energy is accompanied with a reduced bonding distance, which is interpreted in a way that the local order for a molecule is increased considerably. Thus the increased entropy due to the short range order overcompensates the loss of entropy in the long-range order regime, which could be observed due to, e.g., LEED.

Summary

In summary the data of NTCDA monolayers and multilayers on a Ag(111) surface using HREELS as a tool were presented.

The electronic excitation spectra reveal a partially filled molecular orbital which is strongly shifted compared to the multilayer. The existence of this state is responsible for the activation of normally forbidden A_g modes, which are observed in the vibrational spectra. The mechanism behind the activation of these modes is electron-phonon coupling, leading to the fact that these modes exhibit a Fano-like line shape. An analysis of these peak profiles taking advantage of a theoretical model, leads to the electron-phonon coupling constants for the involved modes in this system.

Cooling of a monolayer leads to a phase transition with strong changes in the spectroscopic features in both electronic and vibronic excitations. The phase transition is accompanied with a loss of long-range order and a complete filling of the partially filled molecular orbital, leading to stronger molecule surface bonding.

5.7 Crystalline growth of NTCDA films on Ag(111) investigated by high resolution low energy electron diffraction (SPA-LEED)

An investigation of the multilayer growth behavior of NTCDA multilayer films on a Ag(111) substrate using high resolution SPA-LEED and XPS measurements will be presented. For NTCDA monolayers three ordered phases depending on the coverage are known. On top of the compressed monolayer a Stranski-Krastanov growth mode is achieved on room temperature substrates where the resulting diffraction pattern of the islands can be described by the NTCDA bulk crystal. The bulk like islands grow in two distinct orientations on the surface.

The growth of organic thin films has achieved considerable attention. Both fundamental and applied aspects are of interest in this field [120, 166, 167]. While molecular beam epitaxy is an established tool for the growth of inorganic metals and semiconductors the growth of films with large organic molecules is still a field with many open questions [83, 168]. Various combinations of molecules and surfaces have been investigated to get insight into the influence of molecular size, functional groups, and molecule-substrate interaction. Detailed studies of the interface, i.e. the first and second organic layer, are necessary since these form in many cases the actual substrate where the multilayer growth starts.

In this case the growth of NTCDA multilayers on room temperature Ag(111) substrates was investigated. The interface on which the multilayer growth starts is a closed flat-lying monolayer of molecules, which is well known from STM, LEED, NEXAFS and XPS studies [142, 152]. It is known from former LEED and STM studies of this system that in the monolayer two different structures may occur depending on coverage [46], whereas a more detailed SPA-LEED examination has revealed an additional structure [47], leading to overall 3 different reconstructions. Thick NTCDA films have been investigated before using different methods. NEXAFS and HREELS measurements lead to the conclusion that for multilayers two growth regimes exist. A room temperature substrate leads to mostly upright standing molecules with an average tilt angle of 82° [48] whereas a cooled substrate (below 200K) leads to the growth of almost flat lying molecules [127] [chapter 5.5]. But also films with an average tilt angle of 55° are reported after annealing films prepared on a cold substrate [85]. This might be due to a superposition of the two known phases and/or due to additional phases.

The structure of the NTCDA molecular crystal (see Fig. 5.25b) is known to be monoclinic C_{2h}^5 ($P2_1/c$) [42] with two molecules per unit cell. This results in a lattice plane distance of 3.52\AA in direction of axis b (compare chapter 3.1.1). A view from the $[100]$ direction is plotted in detail in Fig. 5.25b. The lattice parameters derived by [42] are $a=7.862\text{\AA}$, $b=5.305\text{\AA}$, $c=12.574\text{\AA}$ and the angle $\beta=72.73^\circ$. In Fig. 5.25c a symmetry element of the crystal relevant in the further discussion namely a glide reflection is shown. When viewing the crystal from the $[100]$ direction the symmetry operations are obviously the $(\sigma \perp \vec{b})$ labelled mirror plane with translation vector $\vec{\tau} \parallel \vec{c}$ axis [42]. The grey molecules are the mirror image of the colored molecules and indicate the position before the glide operation.

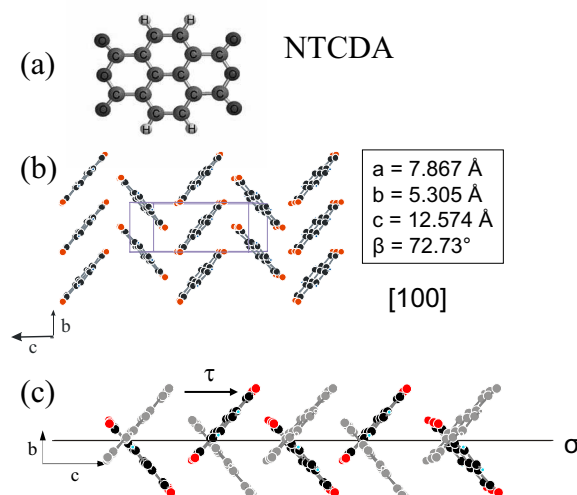


Figure 5.25: The NTCDA molecule (a), a NTCDA crystal viewed from $[100]$ (b) and the glide reflection plane (c) are displayed.

Experimental

The experiments were performed in a UHV system with a base pressure of about 1×10^{-10} mbar. The SPA-LEED (Spot Profile Analysis – Low Energy Electron Diffraction) instrument was manufactured by Omicron. The optics

is μ metal shielded inside the UHV chamber which allows experiments with low electron energies down to 20 eV. The optics itself allows a transfer width of up to 2000 Å [169] but this is limited by the mosaicity of the substrate crystal to a value of ≥ 500 Å [170].

The Ag(111) crystal is mounted on a heatable and coolable manipulator. The temperature of the sample was measured by a chromel-alumel thermocouple mounted at the sample holder. This leads to an estimated error in the absolute surface temperature of around ± 10 K but the reproducibility for different preparations is better than 1 K. The substrate was cleaned by repeated sputtering and annealing cycles. If a NTCDA film was on the sample it was thermally desorbed by annealing up to 800 K, using a ramp of 30 K/min for the begin and end of the heating cycle with a 15 min plateau of constant temperature in between. This was followed by 30 min sputtering with 500 eV Ar^+ ions at a partial Ar pressure of 2×10^{-5} mbar leading to a sample current of 3 μA . Then the surface was heated again with a 30 K/min ramp up to 720 K for 30 min. This cycle led to a Ag(111) surface which shows no carbon contamination in the XPS spectra.

NTCDA was purchased from Sigma-Aldrich and cleaned by gradient sublimation before it was loaded into the evaporation cell. The gradient sublimation is a necessary step in sample handling, which will be pointed out in Annex C. The molecular films were then evaporated at 550 K leading to an evaporation rate of 0.2 ML/min on the sample, which was held at a constant temperature of 290 K. Here 1 ML refers to a closed monolayer of flat lying molecules. The film thickness was deduced from the Ag 3d peak attenuation in XPS measurements and by extrapolation of the time needed to achieve the beta monolayer structure [47] (above 0.85 ML) as monitored by LEED assuming the same sticking coefficient for the multilayer as for the monolayer.

The SPA-LEED measurements were performed with an electron energy of 23 eV to reduce a possible beam damage in the films. All SPA-LEED patterns were recorded in 26 V windows corresponding to 139 % of the Ag(111) surface Brillouin zone. Due to this rather large window and due to the low electron energy distortions within the LEED pattern have to be taken into account. Some reflection spots are in the range of nonlinearities due to the aberration of the electric fields of the LEED electronics. The experimental resolution, which is on metal single crystals usually limited by the mosaic spread of the sample [170], was tested with the Ag(111) sample. A transfer width of more than 500 Å ($T = 2\pi/\Delta k_{\parallel}$ with Δk_{\parallel} being the FWHM of the (0,0) spot) at 20 eV electron energy was deduced.

Results and Discussion

For all three known NTCDA monolayer structures the NTCDA molecules are flat-lying on the surface and the structures do not show an analogy to the NTCDA molecular crystal phase, which consists of two molecules with inclined molecular planes per unit cell. As a result of this apparent misfit NTCDA films are expected to be stressed in the transition range between one monolayer and the relaxed bulk thus hampering a layer by layer growth in this coverage regime. For thick films, however, a new superstructure is found that will be presented here. Different growth behaviours depending on the preparation conditions were observed. First we will focus on the LEED pattern that is achieved for thick films. Then the growth mode of NTCDA films at intermediate film thickness will be discussed.

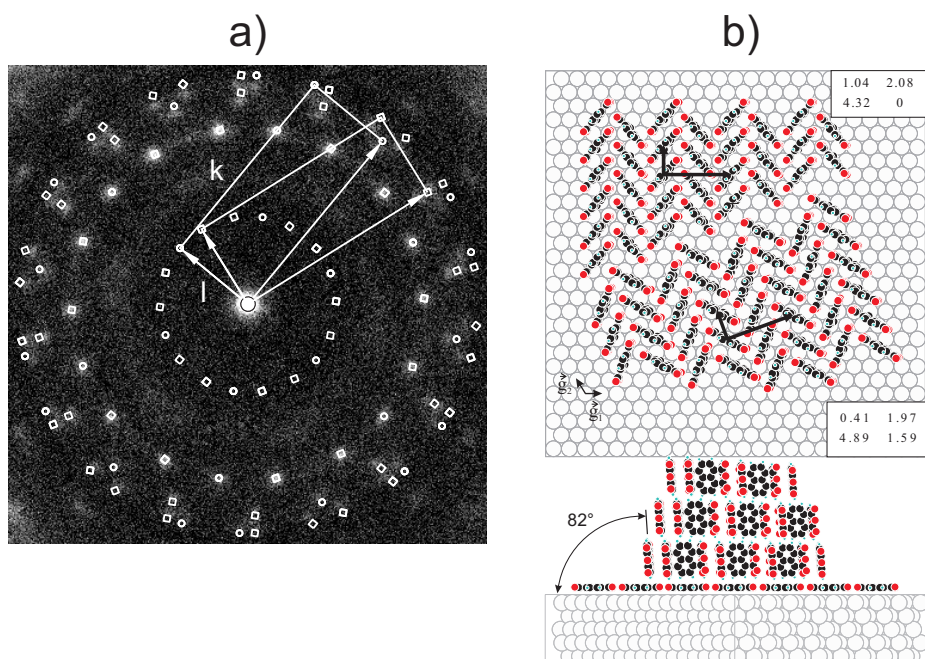


Figure 5.26: The SPA-LEED pattern of a 30 ML NTCDA/Ag(111) film taken with 23 eV primary energy shown together with two superstructure unit cells and simulated spots. The real space suggestion and the derived matrices are given on the right hand side. The molecules have an angle of 82° with respect to the surface, and the unit cells are rectangular with two molecules per unit cell.

The LEED pattern of a closed 30 ML thick film, prepared with a deposition rate of 1 ML/min and a substrate temperature of 285 K, is displayed in

Fig. 5.26a. A ring of 18 diffraction spots (middle ring) and an outer ring consisting of three different triangles of spots are observed. In order to explain the diffraction pattern two superstructures with the matrices

$$A = \begin{pmatrix} 1.04 & 2.08 \\ 4.32 & 0 \end{pmatrix}$$

(circles) and

$$B = \begin{pmatrix} 0.41 & 1.97 \\ 4.89 & 1.59 \end{pmatrix}$$

(squares) have to be taken into account, which both have an identical rectangular unit cell but are rotated by an angle of 18.6° within the surface plane. Because of the six-fold substrate symmetry superstructure A has 3 rotational domains (note that one entry is zero), superstructure B has 6 rotational and mirror domains. The hkl notation will be used to describe the reflection spots with an arbitrary $h \neq 0$ perpendicular to the surface only using the kl leading to spots (k, l). k is chosen as the long vector in reciprocal space and l as the short one as displayed in figure 5.26a.

A detailed assignment along with the according kl is found in Fig. 5.27 and will be outlined now. The middle ring is due to second order diffraction, namely 12 (0, 2) spots from matrix B and superimposed 6 (0, 2) spots from matrix A, whereas the outer ring consists of first and mixed second order spots. The V shaped triangles consist of 2 spots from matrix B ((1, 1) and its mirror spot) and one (1, 0) from matrix A. The other two triangles have also one first order spot. The triangle right of the V shaped spots consists of (1, 0) B and 120° rotated and mirrored (1, -1) B and a (1, -1) A. Taking the symmetry of the surface into account the left triangle consists of the mirrored spots of the right triangle as the high symmetry substrate axis is along (0,0) (1,0) direction. Therefore all observed spots are explained by the two matrices, but the simulation still predicts spots at positions where no intensity is observed. Most obvious are the (0, 1) A and B spots which form the inner ring. This point will be discussed in detail after the introduction of the suggested real space model of the molecules.

Using the reasonable assumption that the molecules tend to form their native organic molecular crystal structure in thick films particularly at elevated temperatures [171] only one possible orientation of the crystals on the surface is found. It allows to explain the LEED data, namely an orientation where the natural [100] cleavage plane of the NTCDA crystal is oriented parallel to the

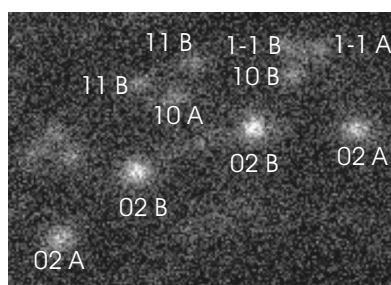


Figure 5.27: A segment of Fig.5.26a is plotted together with a detailed assignment of the diffraction spots. The spots are labeled with their according k l numbers and the matrix they belong to, while the detailed symmetry operations leading to them are outlined in the text.

surface. For illustration in Fig. 5.25b a top and a side view of the NTCDA islands on the Ag(111) surface are plotted where the molecules have an average tilt angle of 82° with respect to the surface. This orientation is consistent with NEXAFS data [48] and was also found in STM experiments on weakly interacting MoS₂ substrates [172]. Also for NTCDA multilayers on KBr an analogue orientation was determined from polarization dependent FTIR measurements [141]. Moreover HREELS measurements of NTCDA multilayers already indicated highly ordered films with upright standing molecules in the room temperature growth regime (see Chapter 5.4).

Provided that the growth model described above occurs, the absence of simulated spots in the measured data can be explained, which corroborates this model. A $P2_1/c$ (C_{2h}^5) crystal has a glide plane $\sigma \perp b$ and $\sigma \parallel c$ and a glide rotation parallel to the b -axis (see Fig. 5.25c) that limits the possible reflections. k and l in the assignment above were already chosen in a way to be consistent with directions of the later proposed 3d crystal structure. For $h0l$ with $l=2n$ ($n \in N$) every odd index l is not visible due to the glide plane. This is exactly what is observed for the $(0, l)$ spots where first order diffraction is not visible in the diffraction pattern. For $0k0$ with $k=2n$ ($n \in N$) also every odd index k will not be observed due to the glide rotation, but since this is only valid for $h=0$ and we measure the diffraction rods for a $h \neq 0$ all spots with $(k, 0)$ are visible in the diffraction pattern. In Fig. 5.28 these two cases are illustrated. The diffraction rods for hl and hk are plotted where for hl odd rods are undetectable and for hk only the end of the rods at $h=0$ is absent for odd k . For both a segment of the Ewald circle is plotted which

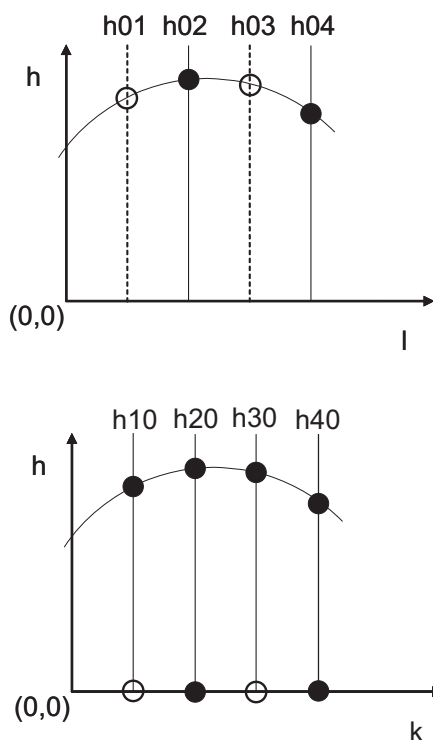


Figure 5.28: The glide reflection of the NTCDA molecular crystal displayed in Fig.5.25c leads to conditions limiting possible reflections plotted as hl and hk diagram together with an Ewald circle. Filled circles are expected to be observed while open circles are forbidden due to symmetry considerations.

leads, depending on the energy used, to the actually observed spots.

In Table 5.7 the derived matrices, real and reciprocal vectors together with their values and the area of the superstructure unit cell are summarized. The derived values for the real space vectors of the unit cell fit very well to the projected unit cell of the $[100]$ direction of the molecular crystal. The excellent agreement between the measured unit cell vectors and those from literature for the molecular crystal are highlighted. The largest relative error is found for $|a|$ to be 2%.

The simulated spots of the outer ring seem to be too far out compared to the observed spots whereas the peaks in the inner ring fit well to the simulated spots. Taking into account the aberration of the SPA-LEED optics for peaks in the outer region this mismatch could be reduced by rescaling. Moreover the aberration leads to the fact that the pattern is not fully rotational symmetric. In order to get an estimate for the error the pattern is compared with one

Table 5.7: Unit cell parameters of the two multilayer structures and the compressed monolayer. All vectors are in Cartesian coordinates, lengths are given in Å in real and Å⁻¹ in reciprocal space. The matrices are given for real space as vectors \vec{a} , \vec{b} whereas \vec{a}^* , \vec{b}^* are in reciprocal space. The vectors for the Ag(111) substrate are given in capital letters.

Superstructure	Multilayer A	Multilayer B	Monolayer
Matrix	$\begin{pmatrix} 1.04 & 2.08 \\ 4.32 & 0.00 \end{pmatrix}$	$\begin{pmatrix} 0.41 & 1.97 \\ 4.89 & 1.59 \end{pmatrix}$	$\begin{pmatrix} 3.79 & 6.52 \\ -2.98 & 0.58 \end{pmatrix}$
\vec{a}	(0.01, 5.2)	(-1.65, 4.92)	(2.18, 16.30)
\vec{b}	(12.49, 0)	(11.84, 3.98)	(-9.41, 1.26)
\vec{a}^*	(0, -1.21)	(0.38, 1.14)	(0.05, 0.38)
\vec{b}^*	(0.50, 0)	(0.48, 0.16)	(-0.66, 0.09)
a	5.2 Å	5.2 Å	16.45 Å
b	12.49 Å	12.5 Å	9.5 Å
a*	1.21 Å ⁻¹	1.20 Å ⁻¹	0.382 Å ⁻¹
b*	0.50 Å ⁻¹	0.50 Å ⁻¹	0.662 Å ⁻¹
Area	64.95 Å ²	65 Å ²	156.2 Å ²
Angle	90°	90°	90°
\vec{A}	(2.89, 0.0)	Real space NTCDA crystal	12.574 Å
\vec{B}	(-1.44, 2.5)		5.305 Å
\vec{A}^*	(2.17, 1.25)		7.867 Å
\vec{B}^*	(0.0, 2.50)		

achieved for a CuPc monolayer on Ag(111)

$$\begin{pmatrix} 5.55 & 2.55 \\ -0.33 & 4.67 \end{pmatrix}$$

(see Fig. 5.29). In this case the LEED pattern has a rich structure and allows to determine the matrix with an error below ± 0.02 . Moreover additional diffraction spots allow aligning the CuPc LEED pattern to the NTCDA counterpart with high accuracy. The comparison of both pictures proves that the deviation is only due to aberration but induces a larger error bar to the deduced matrix entries. As mentioned the aberration is not only radial which could be accounted for by a scaling factor but also has a rotational contribution and is therefore hard to recalculate. Therefore the error is estimated to be in the range of 0.05 as for higher values the simulated spots start to show a deviation from the measured spots for the circle of the inner 18 spots.

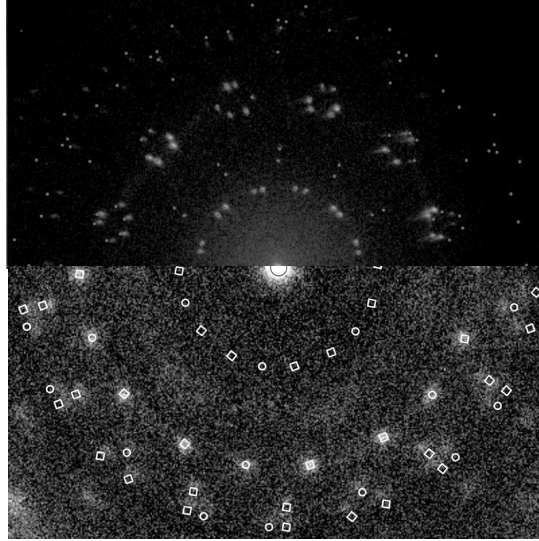


Figure 5.29: CuPc monolayer Ag(111) (upper) and NTCDA (lower) LEED pattern are displayed in order to estimate the aberration of the SPA-LEED optics in case of NTCDA.

For thinner NTCDA films (Fig.5.30) additional spots are revealed which are known from the monolayer measurements and originate from the so called

compressed monolayer [46]. The fact that these spots with the superstructure matrix

$$\begin{pmatrix} 3.97 & 6.52 \\ -2.98 & 0.58 \end{pmatrix}$$

are observable for a layer thickness up to several layers leads to the conclusion that for the current preparation conditions Stranski Krastanov growth starts beyond the monolayer. This is consistent with SMART measurements where the growth of islands on top of the first monolayer was also observed [49]. Moreover also in HREELS measurements a superposition of monolayer and multilayer vibrational signature was observed up to 6 ML for films grown on a room temperature substrate (see Chapter 5.5).

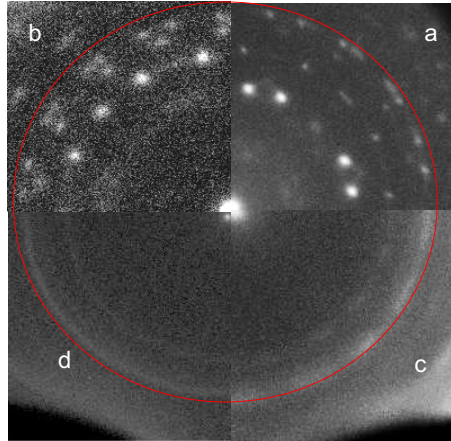


Figure 5.30: Diffraction patterns of NTCDA films with increasing film thickness. From Stranski-Krastanov growth (a) (5ML) to a highly ordered multilayer (b) (30ML). In (c) (50ML) the spots start to smear out to rings which remain in (d) (100 ML).

Using a low evaporation rate (0.2 ML/min) the compressed monolayer signal disappears with increasing film thickness and the spots of the multilayer start to smear out. This can be observed in Fig. 5.30c for a 50ML film. At the position of the spots there is still intensity but the spots start to connect

to form a ring-like structure. This can be explained by islands that do not only grow in the two preferential directions on the substrate (see Fig. 5.26) but start to have arbitrary azimuthal orientation. However, the crystallites are still oriented with the [100] plane perpendicular to the surface which can be concluded from the radius of the rings in the diffraction pattern. This has the same value as the radius of the spots, which can also be seen very clearly in Fig. 5.30. For thicker films the spots are completely smeared out azimuthally so much that homogeneous rings are formed (see Fig. 5.30d) for a 100ML film.

For sublimation onto a cold (200K and below) substrate, which leads to almost perfectly flat lying molecules [48, 85] [Chapter 5.5], no diffraction pattern was found. This is also consistent with the findings in Chapter 5.4 where the decreased intensity and the FWHM of the elastically reflected electrons in HREELS spectra were interpreted as a lack of long range lateral order in low temperature multilayer films.

Conclusions

Using SPA-LEED as tool to determine long range order and surface unit cells the multilayer growth of NTCDA/Ag(111) was studied. On a closed monolayer Stranski Krastanov growth starts leading to a superposition of monolayer and multilayer diffraction patterns. The multilayers grow in the structure of the NTCDA molecular crystal with the natural [100] cleavage plane as interface. The islands have two distinct orientations with respect to the surface: one is aligned with the Ag substrate direction (-100) and (-1-12), the other is rotated by 18.6° . Additional deposition first leads to closed multilayer films in an intermediate thickness range whereas in thicker films the relative orientation to the substrate is lost. This leads to an azimuthal smearing of the LEED spots and finally to a ring in the diffraction pattern. The films turned out to be sensitive to electron irradiation leading to beam damage, which can be assigned to the breaking of C=O bonds in the functional group.

Chapter 6

Zusammenfassung

Im Rahmen dieser Arbeit wurden vibronische und elektronische Zustände großer organischer Moleküle untersucht. Eine zentrale Frage ist die Wechselwirkung innerhalb der Moleküle, zwischen Molekülen, in dünnen Filmen und an Metall-Organik Grenzflächen. Als experimentelle Methoden wurden Hochauflösende Elektronenenergie Verlust Spektroskopie (HREELS) und hoch auflösende Röntgenabsorptionsspektroskopie (NEXAFS) verwendet.

Die elektronische und vibronische Struktur dünner NTCDA Schichten wurde mit HREELS untersucht. Die elektronischen Anregungsspektren von NTCDA Submonolagen auf einer Ag(111) Oberfläche zeigen ein teilgefülltes Molekülorbital, dessen Wechselwirkung mit totalsymmetrischen Molekülschwingungen zu den typischen asymmetrischen Fano Peaks führt. Die geordnete Monolage lässt sich durch Kühlung in eine ungeordnete Phase überführen, die deutliche Änderungen in den elektronischen und vibronischen Spektren zeigt. Multilagen ergeben in Abhängigkeit von den Präparationsbedingungen flach liegende bzw. fast aufrecht stehende Moleküle. Für aufrecht stehende Moleküle zeigen die Schichten Inselwachstum, wobei die Inseln wohlgeordnet sind und in Streuexperimenten eine Struktur zeigen, die dem Molekülkristall entsprechen.

Um die geordneten NTCDA Schichten im Detail zu untersuchen, wurden die verschiedene Schichten in Abhängigkeit von Schichtdicke und Präparationsparametern untersucht. Es zeigt sich, dass sich auf einem gekühlten Substrat keine langreichweitige Ordnung ausbildet, die zu einem Beugungsbild führt. Auf einem Raumtemperatursubstrat dagegen zeigt sich, dass die Moleküle ein Inselwachstum in ihrer Molekülkristallstruktur bevorzugen, wobei zwei Orientierungen der Inseln relativ zum Substrat vorkommen. Bei dicken Schichten geht der Bezug zum Substrat verloren und die Kristallite

wachsen mit einem definierten Oberflächenvektor, aber in unterschiedlicher azimuthaler Orientierung, was zu Ringen im Beugungsbild führt.

NTCDA Monolagen auf einer Ag(111) Oberfläche wurden mittels HREELS untersucht. Die elektronische Struktur der Spektren zeigt ein teilgefülltes Orbital, das im Vergleich mit den Multilagenspektren energetisch stark verschoben ist. Die Existenz dieses Zustandes führt dazu, dass Symmetrieverbotene A_g Moden in den Schwingungsspektren sichtbar werden. Die Kopplung von elektronischen mit vibronischen Zuständen führt zu den typischen Fano Peak Profilen. Beim Abkühlen dieser Monolagen ist ein Phasenübergang zu beobachten, der zu deutlichen Änderungen der elektronischen und vibronischen Spektren führt.

Für das Molekül ANQ wurde die intramolekulare Wechselwirkung untersucht. In den Sauerstoff Spektren zeigt sich eine vibronische Feinstruktur, die auf ein asymmetrisches Potential schließen lässt. Interessant ist die Frage, ob es sich dabei um eine Kopplung an C-H oder an C=O Moden handelt. Um diese Frage zu erörtern wurden, Spektren aus der kondensierten und der Gasphase von ANQ und einem ANQ Derivat (ANQ-Br₂Cl₂) verglichen, wobei sich zeigt, dass es sich wahrscheinlich um eine Ankopplung an C=O Moden handelt.

Hochaufgelöste C1s Spektren von normalem und völlig deuteriertem Naphthalin wurden sowohl in der kondensierten als auch in der Gasphase untersucht. In Abhängigkeit vom Endzustand wurden Unterschiede zwischen Gas- und kondensierter Phase beobachtet. Eine energetische Verschiebung der Resonanzen (Res. B, C, D) wird als Resultat der π - π Wechselwirkung in der kondensierten Phase interpretiert. Dies ist besonders bemerkenswert für Resonanz B, da sie unzweifelhaft einer Anregung in ein π^* zugeordnet werden kann. Die Resultate führen zu der Interpretation, dass für einige organische Molekülkristalle mehr als reine Van-der-Waals Wechselwirkung berücksichtigt werden muss.

Insgesamt zeigt sich, dass die intramolekulare Wechselwirkung in NEX-AFS Spektren eine Ankopplung an eine oder wenige vibronische Progressionen bevorzugt. Dabei können die elektronischen Anregungen wegen der delokalisierten Elektronensysteme auch vibronischen Zustände anregen, die nicht an dem angeregten Kohlenstoff Atom lokalisiert sind. Es konnte gezeigt werden, dass die Kondensation der Moleküle in Filmen zu Änderungen im Spektrum führt. Der Einfluss der intermolekularen Wechselwirkung lässt sich daran deutlich erkennen, wobei es deutliche Hinweise gibt, dass mehr als reine van der Waals Bindung zur Erklärung berücksichtigt werden muss.

Conclusions

In the frame of this thesis vibronic and electronic states of organic molecules have been examined. A central question is the interaction within and between the molecules in thin films and at metal-organic interfaces. The main experimental tools were high resolution electron energy loss spectroscopy (HREELS) and high resolution near edge X-ray absorption fine structure (NEXFAS).

The electronic and vibronic structure of thin NTCDA films was examined with low energy electrons as probe, i.e. HREELS. The spectra of the electronic excited molecular orbitals of submonolayer NTCDA on a Ag(111) shows a partially filled orbital. The interaction between this orbital and the total symmetric molecular vibrations leads to the typical Fano peak profiles which are seen in the vibrational spectra. The sub-monolayer superstructure can be driven to a phase transition into an disordered phase upon cooling, which is also seen in the electronic and vibronic excitation spectra. Multilayers show flat lying or upright standing molecules as a function of the preparation conditions. The upright standing molecules show an island growth mode, where the islands are well ordered and exhibit a structure in diffraction experiments which can be attributed to the molecular crystal structure.

In order to examine the order in more detail various thin films were examined using SPALEED as function of film thickness and preparation parameters. In case of a low temperature substrate no long range order leading to a diffraction pattern was found. In contrast growth on room temperature substrates leads to island growth of films in a structure of the molecular crystal, where two preferred orientations of the islands relative to the substrate were found. In case of thick films the reference to the substrate gets lost and the molecular crystals grow with a defined crystal direction with respect to the surface but with an arbitrary azimuthal orientation leading to circles in the diffraction pattern.

NTCDA monolayers on a Ag(111) surface using HREELS as a tool were ex-

aminated. The electronic excitation spectra reveal a partially filled molecular orbital which is strongly shifted compared to the multilayer. The existence of this state is responsible for the activation of normally forbidden Ag modes in the vibrational spectra. Due to the electron phonon coupling these modes exhibit a Fano like peak shape. Cooling a monolayer leads to a phase transition with strong changes in the spectroscopic features both in electronic and vibronic excitations.

In case of the molecule ANQ the intramolecular interaction was examined. In the oxygen NEXAFS spectra a vibronic fine structure is found, which leads to the conclusion that asymmetric potentials are involved. It is an interesting question if the fundamental vibration is has C-H or C=O character. In order to address this question spectra of condensed and gas phase ANQ were compared to an ANQ derivate (ANQ- Br₂Cl₂), with the conclusion that the coupling is most likely to a C=O mode.

High resolution C1s spectra of hydrogenated and fully deuterated naphthalene both in gas and condensed phase have been presented. Depending on the final state orbital distinct differences have been found between gas and condensed phase. A energetic shift of resonances (Res. B, C, D) is interpreted as effect of π - π interaction in the condensed phase. This is especially notable for resonance B which is undoubtly assigned to an excitation into a π^* orbital. The results lead to an interpretation, that for organic molecular crystals more than pure van-derWaals interaction has to be taken into account.

In summary it is found that the intramolecular interaction in NEXAFS spectra is preferentially coupled to one or a few vibronic progressions. Due to the delocalized electronic system maybe even states which are not spatially near the core excited atom can be involved. It could be shown that a condensation of the molecules in thin films leads to changes within the spectra. The influence the intermolecular interaction can be clearly seen in this finding, where additional hints are found that more than mere van-der-Waals binding has to be taken into account.

Appendix A

Excited states of Naphthalene

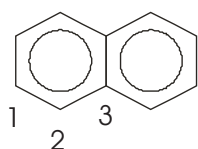
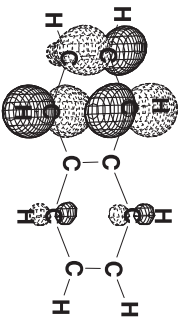
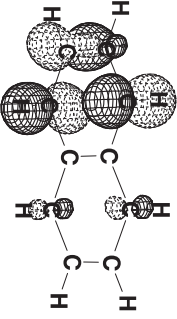
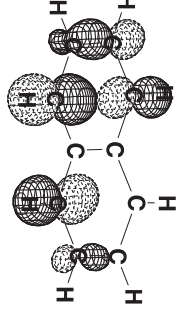
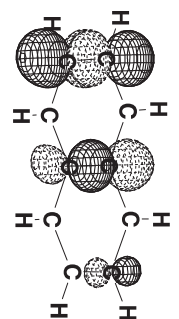
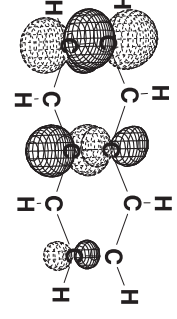
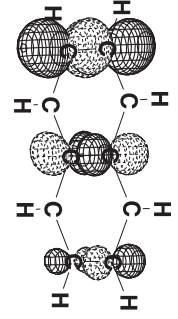
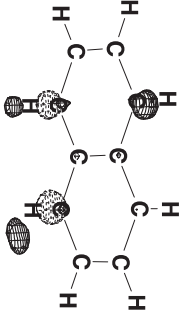
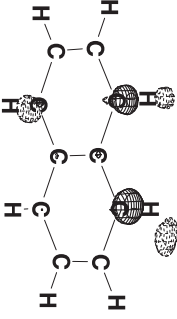
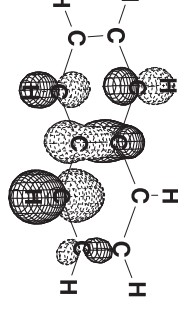
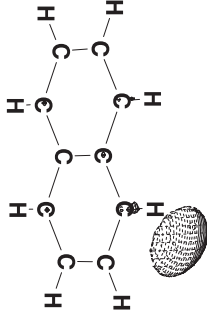


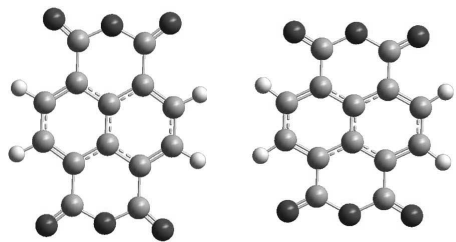
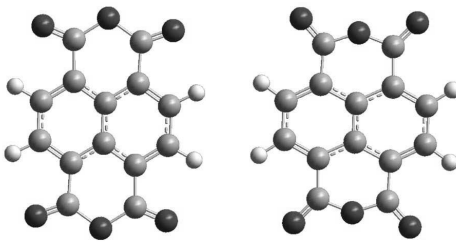
Table A.1: Lowest excited naphthalene states

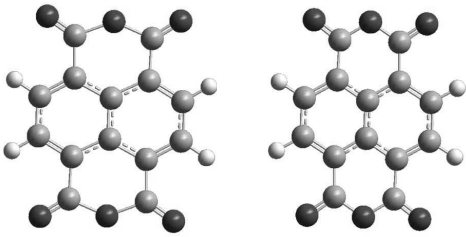
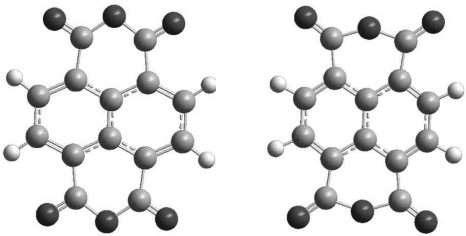
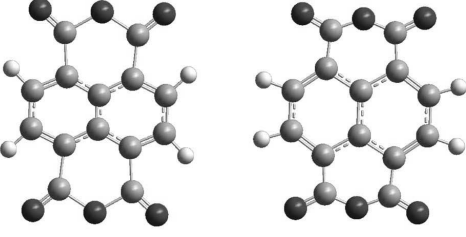
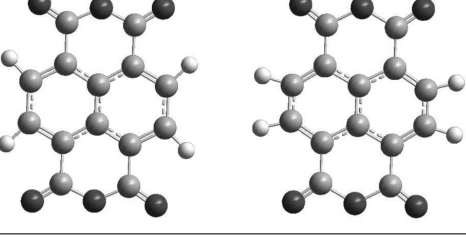
	C1	C2	C3
LUMO			
LUMO+1			
LUMO+2			
LUMO+3			

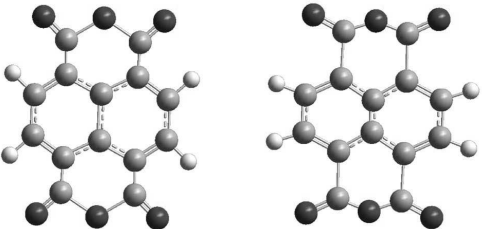
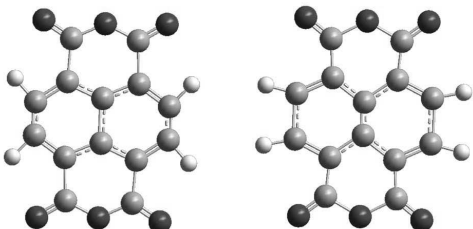
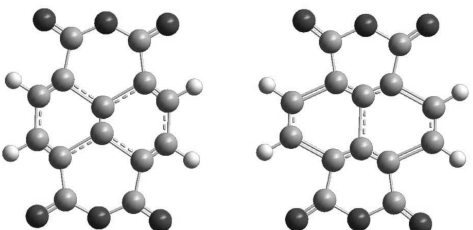
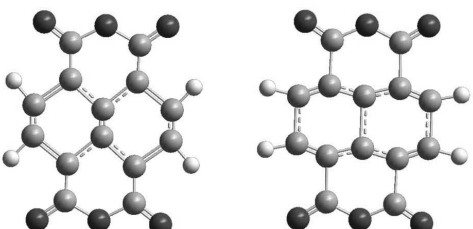
Appendix B

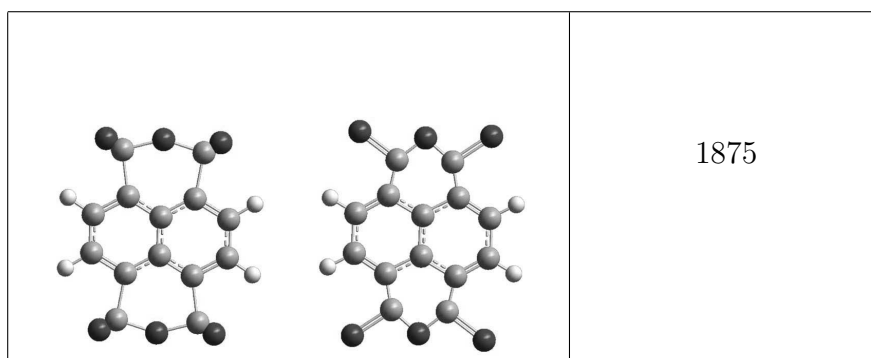
Visualization of NTCD A_g modes

In the following table some A_g modes are plotted during their molecular vibration in their extremal positions. In order clarify the influence of the vibration to the molecule the elongation of the vibration is plotted enhanced.

Vibration	Wavenumber (cm ⁻¹)
	315
	412

	549
	670
	1022
	1123

	1287
	1393
	1461
	1652



Appendix C

SPA-LEED annex

Beam damage during irradiation with electrons, which leads to a disappearance of the multilayer LEED pattern, was observed. On a time scale of 4 h the multilayer pattern fades without creating new spots whereas the monolayer pattern is unchanged as long as it is observable for the respective sample preparation. There are two possible explanations which could lead to this behaviour. In both scenarios the weak coupling within the multilayer crystals leads to an insufficient energy transport away from an excited molecule. This might either result in beam damage within the molecule resulting in a defect and thus in a loss of long range order. Or the energy transfer leads to desorption of the molecule (or fragments) from the substrate. Fig. C.1 compares the C 1s and Ag 3d signal of a film which showed mono- and multilayer LEED spots before the SPA-LEED measurement and only a monolayer signal afterwards. Since there is almost no change in the integral intensity of the carbon and silver peaks before and after more than 12 h of electron irradiation the conclusion that electron induced desorption has not to be taken into account can be drawn. However there are significant changes: the relative intensity of the anhydride (ring) carbon atoms is reduced (increased) reproducibly after the SPA-LEED measurement while the intensity of the substrate is increased. This leads to the conclusion that there is beam damage within the molecules. Assuming a beam damage at the anhydride groups leading to the desorption of O₂ or CO can explain the XPS and SPA-LEED results [173,174]. The decreasing signal of the anhydride carbon species leads to a relative increase of ring carbon intensity while the integrated intensity does not change. The Ag substrate signal is expected to increase slightly according to this scenario. The relative intensity of the carbon species leads to the conclusion that only a few % of the molecules are damaged which is obviously enough to hamper a long range order within the islands. Therefore

the beam damage is assigned to be preferentially located at the C=O of the anhydride groups.

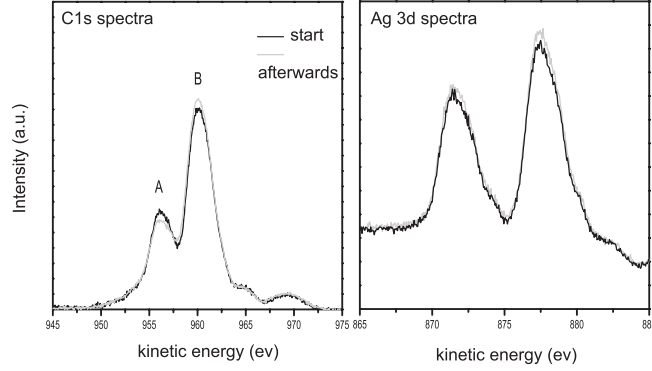


Figure C.1: A comparison of C1s and Ag3d spectra before (black) and after (gray) SPA-LEED measurement. The signal of carboxyl carbon (peak A) is decreased whereas the signal for ring carbon (peak B) is enhanced. The Ag substrate signal is slightly increased after electron irradiation.

As mentioned in Chapter 5.7, gradient sublimation of the purchased NTCDA was a necessary step which can be seen in Fig. C.2 where mass spectra from NTCDA as purchased and sublimated are compared. Both were recorded by evaporating the organic material from a crucible after comparable treatment, i.e. bake out, degassing, and sublimation at the same temperature. The intensities and ratios of those high masses, that are cracking products of NTCDA, are 1:1 within the error bar. But for low masses, namely 44u (CO_2) and 18u (H_2O) additional peaks are found in the unsublimated (a) NTCDA, which is assigned to remnants of the production process of the substance. These contaminations did not lead to a detectable signal in XPS, but may affect the conductivity of NTCDA according to [148]. Using the unsublimated NTCDA to prepare the known monolayer structures did lead to some additional spots within the known diffraction pattern and therefore more effects of contaminations have to be taken into account than just H_2O and CO_2 as suggested by QMS.

Working with unsublimated NTCDA in the evaporation cell leads to LEED patterns like that displayed in Fig. C.3 in which a superposition of a relaxed monolayer and an additional structure is found. Two possible matrices were derived for this new structure, namely:

$$M_{U1} = \begin{pmatrix} 3 & 0 \\ 1 & 2 \end{pmatrix}$$

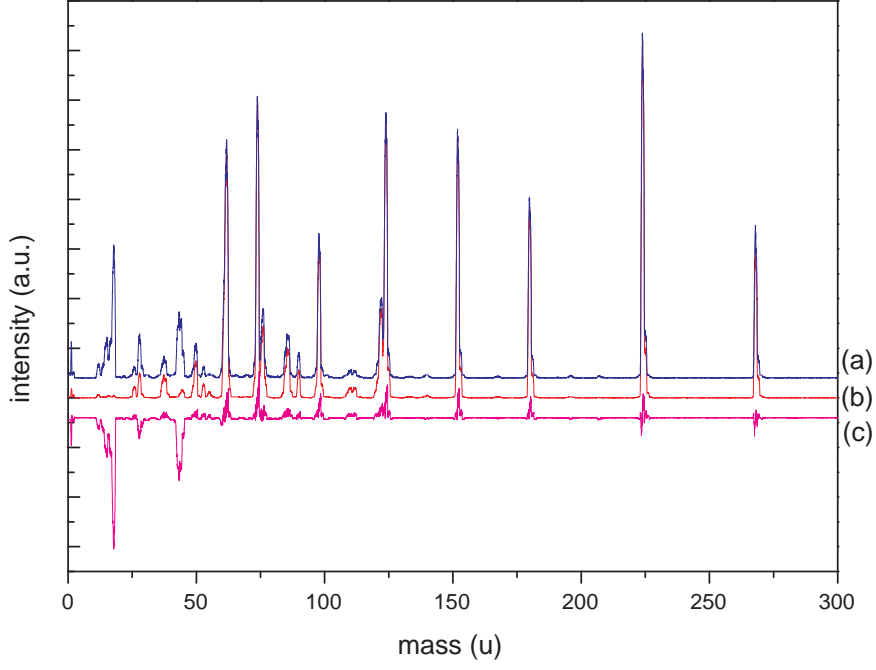


Figure C.2: Quadrupole mass spectra of as purchased unsublimated NTCDA (a) and sublimated NTCDA (b) and a difference spectrum (a)-(b)=(c) are plotted. The highest mass at 268 u is NTCDA with its typical cracking pattern for lower masses. For low masses a contamination is obvious at 18 u (H_2O) and 44 u (CO_2).

with an angle of 90° of the unit cell vectors, and

$$M_{U2} = \begin{pmatrix} 4 & 2 \\ -2 & 2 \end{pmatrix}$$

with an angle of 120° between the unit cell vectors. Keeping in mind that the determinant of a superstructure matrix is related proportional to the area of the structure on a surface one can compare the known relaxed monolayer with the new matrices. Judging from the determinate of the relaxed monolayer

$$(\text{Det}(\text{RM}) = \begin{vmatrix} 3.97 & 6.52 \\ -2.98 & 0.58 \end{vmatrix} = 24) \text{ with two molecules per unit cell a com-}$$

parison with these two superstructures can be drawn. $\text{Det}(M_{U1}) = \begin{vmatrix} 3 & 0 \\ 1 & 2 \end{vmatrix} = 6$ and $\text{Det}(M_{U2}) = \begin{vmatrix} 4 & 2 \\ -2 & 2 \end{vmatrix} = 8$ which directly leads to the conclusion that there is not enough space for a flat lying molecule in the unit cell or the molecules have a tilt angle with respect to the surface.

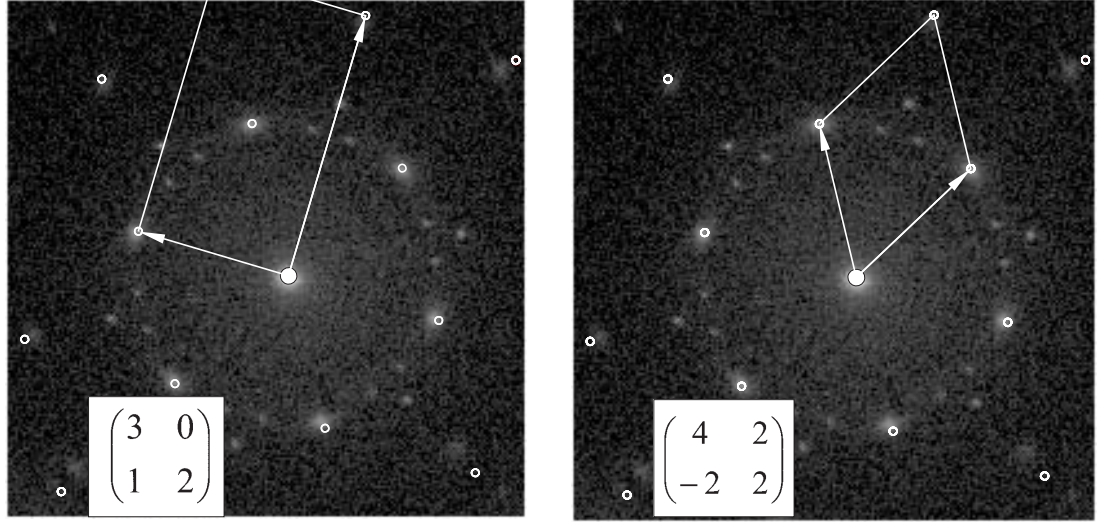


Figure C.3: Both identical LEED patterns show the superposition of the known NTCDA relaxed monolayer 3.3 and a pattern due to impurities. Two possible unit cells are suggested for the additional spots named M_{U1} left and M_{U2} right.

Bibliography

- [1] Bundespräsident Roman Herzog. *Ansprache anlässlich des Röntgenjubiläums in der Universität Würzburg, 8.11.1995.*
- [2] C. Väterlein, H. Neureiter, W. Gebauer, B. Ziegler, M. Sokolowski, P. Bäuerle, and E. Umbach. Organic light emitting devices based on vapor deposited films of end-capped sexithiophene: Evidence for schottky barriers and transport limitations. *J. Appl. Phys.*, 82 (6):3003–3013, 1997.
- [3] J. Lee, Y. Park, DV. Kim, HY. Chu, H. Lee, and LM. Do. High efficiency organic light-emitting devices with Al/NaF cathode. *Appl. Phys. Lett.*, 82 (2):173–175, 2003.
- [4] T. Dobbertin, M. Kroeger, D. Heithecker, D. Schneider, D. Metzdorf, H. Neuner, E. Becker, HH. Johannes, and W. Kowalsky. Inverted top-emitting organic light-emitting diodes using sputter-deposited anodes. *Appl. Phys. Lett.*, 82 (2):284–286, 2003.
- [5] K. Kim, M.K. Kim, H.S. Kang, M.Y. Cho, J. Joo, J.H. Kim, K.H. Kim, C.S. Hong, and D.H. Choi. New growth method of rubrene single crystal for organic field-effect transistor. *Synthetic Metals*, 157 (10-12):481–484, 2007.
- [6] G. Horowitz. Organic field-effect transistors. *Adv. Mater.*, 10(5):365–377, 1998.
- [7] M. Hiramoto, H. Fujiwara, and M. Yokoyama. 3-layered organic solar-cell with a photoactive interlayer of codeposited pigments. *Appl. Phys. Lett.*, 58 (10):1062–1064, 1991.
- [8] K. Tvingstedt, V. Andersson, F. Zhang, and O. Inganas. Folded reflective tandem polymer solar cell doubles efficiency. *Appl. Phys. Lett.*, 91 (12):Art. No. 123514, 2007.

- [9] T. Maruyama, A. Hirasawa, T. Shindow, K. Akimoto, H. Kato, and A. Kakizaki. Energy-level alignment at NTCDA/metal and PTCDA/NTCDA interfaces studied by ups. *J. Lumin.*, 87-9:782–784, 2000.
- [10] T. Kamtsume, M. Hiramoto, and M. Yokoyama. Photocurrent multiplication in naphthalene tetracarboxylic anhydride film at room temperature. *Appl. Phys. Lett.*, 69:3722, 1996.
- [11] Ch. Kittel. *Einführung in die Festkörperphysik*. R. Oldenburg Verlag, München Wien, 1996.
- [12] M.A. Van Hove. *Low-Energy-Electron Diffraction*. Springer-Verlag, 1986.
- [13] F.M. Probst and T.C. Piper. Detection of vibrational states of gases adsorbed on tungsten by low-energy-electron scattering. *Journal Vac. Sci.*, 4:53, 1967.
- [14] H. Ibach. Surface vibrations of silicon detected low-energy-electron-spectroscopy. *Journal Vac. Sci. Tech.*, 9:713, 1971.
- [15] H. Ibach and D. Mills. *Electron Energy Loss Spectroscopy and Surface Vibrations*. Academic Press, New York, 1982.
- [16] G. Herzberg. Infrared and raman spectra of polyatomic molecules. *Molecular Spectra and Molecular Structure*, 2, 1954.
- [17] A.A. Lucas and M. Sunjic. Fast-electron spectroscopy of surface excitations. *Phys. Rev. Lett.*, 26:229, 1971.
- [18] G. Ertl and J. Küppers. *Low Energy Electrons and Surface Chemistry*. Verlag Chemie, Weinheim, 1985.
- [19] Ed.R.F. Willis. *Vibrational Spectroscopy of Adsorbates*. Springer, Berlin, 1980.
- [20] H. Froizheim. *Electron Spectroscopy for Surface Analysis, Topics in the Current Physics, Vol.4, Ed. H.Ibach*. Springer, Berlin, 1977.
- [21] E.A. Stern and R.A. Ferrell. Surface plasma oscillations of a degenerate electron gas. *Phys. Rev.*, 120:130, 1960.
- [22] D.M. Newns. Electron-surface-plasmon scattering using a parabolic nontouching trajectory. *Phys. Rev. Lett.*, 38:36–40, 1977.

- [23] F. Delanaye and A. Lucas. Inelastic scattering of electrons by vibrational motion of molecules adsorbed at metal surfaces. *Surface Science*, 70:629–642, 1978.
- [24] E. Evans and D.L. Mills. Theory of inelastic scattering of slow electrons by long-wavelength surface optical phonons. *Physical Review B*, 5:4126, 1972.
- [25] E. Evans and D.L. Mills. Theory of inelastic scattering of slow electrons by long-wavelength surface of optical phonons: Multiphonon processes. *Physical Review B*, 7:853, 1973.
- [26] Z. Lenac, M. Sunjic, D. Socevic, and R. Brako. Low-energy scattering by molecules adsorbed on metal surfaces. *Surface Science*, 80:602–611, 1979.
- [27] D. Socevic, Z. Lenac, M. Sunjic, and R. Brako. Excitation of adsorbed molecule vibrations in low-energy electron-scattering. *Zeitschrift für Physik B*, 28:273–281, 1977.
- [28] B.N.J. Persson. Theory of inelastic scattering of slow electrons by molecules absorbed on metal surfaces. *Solid State Communications*, 24:573–575, 1977.
- [29] D.M. Newns. *Vibrational Spectroscopy of Adsorbates*, Ed. R.F. Willis. Springer, Berlin, 1980.
- [30] R.E. Palmer and P.J. Rous. Resonances in electron scattering by molecules on surfaces. *Rev. Mod. Phys.*, 64:383–440, 1992.
- [31] P. Jakob. Adsorption und thermische evolution von aromatischen molekülen auf ru(001). *Dissertation Universität München*, 1989.
- [32] R. F. Willis. *The Chemical Physics of Solid Surfaces and Heterogeneous Catalysis*, 2:59, 1983.
- [33] J.D. Jackson. *Klassische Elektrodynamik*. J.Wiley and Sons Inc., New York, 1975.
- [34] J. Stöhr. NEXAFS spectroscopy. *Springer Verlag, Berlin*, 1992.
- [35] Achim Schöll. Dissertation: High-resolution investigation of the electronic structure of organic thin films. 2003.

- [36] M. Born and R. Oppenheimer. Zur Quantentheorie der Moleküle. *Annalen der Physik*, 84:457 ff., 1927.
- [37] U. Höfer. *Hochauflösende Photoelektronen-Spektroskopie an Oberflächen*. PhD thesis, TU München, 1989.
- [38] Baker C. Baker A.D. Turner, D.W. and Brundle C.R. Molecular photoelectron spectroscopy. *John Wiley & Sons Ltd., London*, 1970.
- [39] Johann Weidlein. *Schwingungsspektroskopie*. Georg Thieme Verlag Stuttgart, New York, 1982.
- [40] F. Engelke. *Aufbau der Moleküle*. Teubner Studienbücher, Stuttgart, 1992.
- [41] D. Gador. Dissertation: Organische dünnschichten auf einkristalloberoberflächen:wachstumsverhalten und elektronische struktur an grenzflächen. *Universität Würzburg*, 2000.
- [42] L. Born and G. Heywang. Crystal structure of 1,4,5,8-Naphthalene-Tetracarboxylic-dianhydrid(NTDA). *Zeitschrift für Kristallographie*, 190:147–152, 1990.
- [43] V. Shklover. *Dissertation: HREELS- und FTIRRAS Untersuchungen an organischen Dünnschichten: PTCDA und NTCDA auf Ag*. PhD thesis, Universität Würzburg, 2002.
- [44] R. Fink, D. Gador, U. Stahl, Y. Zou, and E. Umbach. Substrate-dependent lateral order in naphthalene-tetracarboxylic-dianhydride monolayers. *Physical Review B*, 60:2818, 1999.
- [45] U. Stahl, D. Gador, R. Soukopp, A. Fink, and E. Umbach. Coverage-dependent superstructures in chemisorbed NTCDA monolayers: a combined LEED and STM study. *Surface Science*, 414:423–434, 1998.
- [46] U. Stahl, D. Gador, A. Soukopp, R. Fink, and E. Umbach. Coverage-dependent superstructures in chemisorbed NTCDA monolayers: a combined LEED and STM study. *Surface Science*, 414(3):423–434, 1998.
- [47] Lennart Kilian. Dissertation: Adsorption, struktur und morphologie hochgeordneter organischer adsorbatschichten. *Universität Würzburg*, 2002.

- [48] D. Gador, C. Buchberger, R. Fink, and E. Umbach. "manipulation" of molecular orientation in ultrathin organic films: NTCDA on Ag(111). *Europhys. Lett.*, 41:231–236, 1998.
- [49] Groh U. *Dissertation: Spektromikroskopische Untersuchungen an organischen Nanostrukturen*. PhD thesis, Universität Würzburg, 2006.
- [50] A. Schöll, D. Hübner, T. Schmidt, S. G. Urquhart, R. Fink, and E. Umbach. Anharmonicity of the core-excited state potential of an organic molecule from NEXAFS vibronic fine structure. *Chem. Phys. Lett.*, 392(4-6):297–302, 2004.
- [51] F. Holch. Diplomarbeit: NEXAFS - Spektroskopie an organischen Molekülen in der Gasphase. *Universität Würzburg*, 2004.
- [52] T.C.W. Mak and J. Trotter. The crystal structure of ace-naphthenequinone. *Acta Cryst.*, 16:811–815, 1963.
- [53] Specs. *HREELS Manual Delta 0.5*.
- [54] Meyer G. Scheithauer U. and Henzler M. A new LEED instrument for quantitative spot profile analysis. *Surface Science*, 178:441–451, 1986.
- [55] Igor. <http://www.wavemetrics.com/>.
- [56] Thermocoax. <http://www.thermocoax.com/>.
- [57] Sigma Aldrich. <http://www.sigmaaldrich.com>.
- [58] Lebow company. <http://www.lebowcompany.com/>.
- [59] Friatec. <http://www.friatec.de/>.
- [60] D. Hübner, F. Holch, M. L. M. Rocco, K. C. Prince, S. Stranges, A. Scholl, E. Umbach, and R. Fink. Isotope effects in high-resolution NEXAFS spectra of naphthalene. *Chem. Phys. Lett.*, 415(1-3):188–192, 2005.
- [61] E. E. Rennie, H. M. Koppe, B. Kempgens, U. Hergenbahn, A. Kivimäki, K. Maier, M. Neeb, A. Rudel, and A. M. Bradshaw. Vibrational and shake-up excitations in the C 1s photoionization of ethane and deuterated ethane. *J. Phys. B: At., Mol. Opt. Phys.*, 32(11):2691–2706, 1999.

- [62] U. Herzenhahn, O. Kugeler, E. E. Rennie, A. Rudel, and S. Marburger. Vibrational excitation of C 1s-ionized ethane. *Surface Review and Letters*, 9(1):13–19, 2002.
- [63] K. C. Prince, R. Richter, M. de Simone, M. Alagia, and M. Coreno. Near edge X-ray absorption spectra of some small polyatomic molecules. *J. Phys. Chem. A*, 107(12):1955–1963, 2003.
- [64] G. Remmers, M. Domke, A. Puschmann, T. Mandel, C. Xue, G. Kaindl, E. Hudson, and D. A. Shirley. High-resolution K-shell photoabsorption in formaldehyde. *Physical Review A*, 46(7):3935–3944, 1992.
- [65] S. G. Urquhart, H. Ade, M. Rafailovich, J. S. Sokolov, and Y. Zhang. Chemical and vibronic effects in the high-resolution near-edge X-ray absorption fine structure spectra of polystyrene isotopomers. *Chem. Phys. Lett.*, 322(5):412–418, 2000.
- [66] A. Schöll, Y. Zou, L. Kilian, D. Hübner, D. Gador, C. Jung, S. G. Urquhart, T. Schmidt, R. Fink, and E. Umbach. Electron-vibron coupling in high-resolution X-ray absorption spectra of organic materials: NTCDa on Ag(111). *Phys. Rev. Lett.*, 93(14), 2004.
- [67] Y. Ma, F. Sette, G. Meigs, S. Modesti, and C. T. Chen. Breaking of ground-state symmetry in core-excited ethylene and benzene. *Phys. Rev. Lett.*, 63(19):2044–2047, 1989.
- [68] C. Kolczewski, R. Puttner, O. Plashkevych, H. Agren, V. Staemmler, M. Martins, G. Snell, A. S. Schlachter, M. Sant’Anna, G. Kaindl, and L. G. M. Pettersson. Detailed study of pyridine at the C1s and N1s ionization thresholds: The influence of the vibrational fine structure. *J. Chem. Phys.*, 115(14):6426–6437, 2001.
- [69] E. E. Rennie, B. Kempgens, H. M. Koppe, U. Herzenhahn, J. Feldhaus, B. S. Itchkawitz, A. L. D. Kilcoyne, A. Kivimaki, K. Maier, M. N. Picanastelli, M. Polcik, A. Rudel, and A. M. Bradshaw. A comprehensive photoabsorption, photoionization, and shake-up excitation study of the C 1s cross section of benzene. *J. Chem. Phys.*, 113(17):7362–7375, 2000.
- [70] P. Väterlein, R. Fink, E. Umbach, and W. Wurth. Analysis of the X-ray absorption spectra of linear saturated hydrocarbons using the X alpha scattered-wave method. *J. Chem. Phys.*, 108(8):3313–3320, 1998.

- [71] I. Minkov, F. Gel'mukhanov, R. Friedlein, W. Osikowicz, C. Suess, G. Ohrwall, S. L. Sorensen, S. Braun, R. Murdey, W. R. Salaneck, and H. Agren. Core excitations of naphthalene: Vibrational structure versus chemical shifts. *J. Chem. Phys.*, 121(12):5733–5739, 2004.
- [72] M. B. Robin, I. Ishii, R. McLaren, and A. P. Hitchcock. Fluorination effects on the inner-shell spectra of unsaturated molecules. *J. Electron. Spectrosc. Relat. Phenom.*, 47:53–92, 1988.
- [73] E. Hollauer, E. D. Prucolo, M. L. M. Rocco, A. D. P. Netto, A. Schöll, and R. Fink. Configuration interaction simulation of the NEXAFS photoabsorption spectrum of naphthalene. *J. Braz. Chem. Soc.*, 16(1):31–36, 2005.
- [74] K. C. Prince, R. R. Blyth, R. Delaunay, M. Zitnik, J. Krempasky, J. Slezak, R. Camilloni, L. Avaldi, M. Coreno, G. Stefani, C. Furlani, M. de Simone, and S. Stranges. The gas-phase photoemission beamline at Elettra. *Journal of Synchrotron Radiation*, 5:565–568, 1998.
- [75] K. C. Prince, L. Avaldi, M. Coreno, R. Camilloni, and M. de Simone. Vibrational structure of core to Rydberg state excitations of carbon dioxide and dinitrogen oxide. *J. Phys. B: At., Mol. Opt. Phys.*, 32(11):2551–2567, 1999.
- [76] N. Kosugi. Strategies to vectorize conventional Scf-CI algorithms. *Theoretica Chimica Acta*, 72(2):149–173, 1987.
- [77] N. Kosugi. Molecular symmetries and vibrations in high-resolution inner-shell spectroscopy. *J. Electron. Spectrosc. Relat. Phenom.*, 79:351–356, 1996.
- [78] H. Agren, O. Vahtras, and V. Carravetta. Near-edge core photoabsorption in polyacenes - model molecules for graphite. *Chem. Phys.*, 196(1-2):47–58, 1995.
- [79] N. Kosugi and H. Kuroda. Efficient methods for solving the open-shell Scf problem and for obtaining an initial guess - the one-hamiltonian and the partial Scf methods. *Chem. Phys. Lett.*, 74(3):490–493, 1980.
- [80] E. R. Lippincott and E. J. Oreilly. Vibrational spectra and assignment of Naphthalene and Naphthalene-D-8. *J. Chem. Phys.*, 23(2):238–244, 1955.

- [81] I. Minkov, F. Gel'mukhanov, H. Agren, R. Friedlein, C. Suess, and W. R. Salaneck. Core excitations of biphenyl. *J. Phys. Chem. A*, 109(7):1330–1336, 2005.
- [82] E. Umbach, K. Glöckler, and M. Sokolowski. Surface "architecture" with large organic molecules: interface order and epitaxy. *Surface Science*, 404(1-3):20–31, 1998.
- [83] S. R. Forrest. Ultrathin organic films grown by organic molecular beam deposition and related techniques. *Chem. Rev.*, 97(6):1793–1896, 1997.
- [84] Paul Alivisatos. From molecules to materials current trends and future directions. *Adv. Matter.*, 10:1297–, 1998.
- [85] A. Schoell, Y. Zou, D. Huebner, S. G. Urquhart, T. Schmidt, R. Fink, and E. Umbach. A comparison of fine structures in high-resolution X-ray-absorption spectra of various condensed organic molecules. *J. Chem. Phys.*, 123(4), 2005.
- [86] H. Yamane and S. Kera. Intermolecular energy-band dispersion in PTCDA multilayers. *Physical Review B*, 68(3), 2003.
- [87] I. Salzmann B. Nickel H. Weiss N. Koch, A. Vollmer and J.P. Rabe. Evidence for temperature dependent electron band dispersion in pentacene. *Phys. Rev. Letters*, 96:156803, 2006.
- [88] A. Schöll S. Krause, M.B. Casu and E. Umbach. Determination of the transport levels by UPS and IPES: Organic semiconductors. *in preperation*.
- [89] M.B. Casu, Y. Zou, S. Kera, D. Batchelor, Th. Schmidt, and E. Umbach. Investigation of polarization effects in organic thin films by surface core level shifts. *Physical Review B*, 76 (19), 2007.
- [90] A. P. Hitchcock, G. Tourillon, R. Garrett, and N. Lazarz. C-1s excitation of azulene and polyazulene studied by electron-energy-loss spectroscopy and X-ray absorption-spectroscopy. *J. Phys. Chem.*, 93(22):7624–7628, 1989.
- [91] P. Yannoulis, R. Dudde, KH. Frank, and EE. Koch. Orientation of aromatic-hydrocarbons on metal-surfaces as determined by NEXAFS. *Surface Science*, 189:519–528, 1987.

- [92] M. L. Gordon, D. Tulumello, G. Cooper, A. P. Hitchcock, P. Glatzel, O. C. Mullins, S. P. Cramer, and U. Bergmann. Inner-shell excitation spectroscopy of fused-ring aromatic molecules by electron energy loss and X-ray raman techniques. *J. Phys. Chem. A*, 107(41):8512–8520, 2003.
- [93] A. Schöll, Y. Zou, T. Schmidt, R. Fink, and E. Umbach. Energy calibration and intensity normalization in high-resolution NEXAFS spectroscopy. *J. Electron. Spectrosc. Relat. Phenom.*, 129(1):1–8, 2003.
- [94] R.R. Blyth, R. Delaunay, M. Zitnik, J. Krempasky, R. Krempaska, J. Slezak, K.C. Prince, R. Richter, M. Vondracek, R. Camilloni, L. Avaldi, M. Coreno, G. Stefani, C. Furlani, M. de Simone, S. Stranges, and M.Y. Adam. The high resolution Gas Phase Photoemission beam-line, Elettra. *J. Electron. Spectrosc. Relat. Phenom.*, 103:959–964, 1999.
- [95] F. Holch. Investigation of intermolecular interaction in organic thin films by means of NEXAFS spectroscopy. *Dissertation Universität Würzburg*, 2010.
- [96] MO. Krause and JH. Oliver. Natural widths of atomic K-levels and L-levels, K-alpha X-ray-lines and several KLL auger lines. *J. Phys. Chem. Ref. Data*, 8(2):329–338, 1979.
- [97] MO. Krause. Atomic radiative and radiationless yields for K-shells and L-shells. *J. Phys. Chem. Ref. Data*, 8(2):307–327, 1979.
- [98] Karvonen J Coreno M Camilloni R Avaldi L de Simone M Prince KC, Vondracek M. A critical comparison of selected 1s and 2p core hole widths. *Journal of Electron Spectroscopy and Related Phenomena*, 103:141–147, 1999.
- [99] M. B. Robin. *Higher Excited States of Polyatomic Molecules, Volume I-II*. Academic Press, New York und London, 1974.
- [100] P. S. Bagus et al. Weiss, K. Rydberg transitions in X-ray absorption spectroscopy of alkanes: The importance of matrix effects. *J. Chem. Phys.*, 111(15):6834–6845, 1999.
- [101] AP. Hitchcock, DC. Newbury, and I ISHII et al. Carbon K-shell excitation of gasouse and condensed cyclic hydrocarbons - C₃H₆, C₄H₈, C₅H₈, C₅H₁₀, C₆H₁₀, C₆H₁₂, and C₈H₈. *J. Chem. Phys.*, 85:4849–4862, 1986.

- [102] Y. Zou, T. Araki, and et al. Solid state effects in the NEXAFS spectra of alkane-based van der Waals crystals: Breakdown of molecular model. *Chem. Phys. Lett.*, 430:287–292, 2006.
- [103] B. R. Holstein. The van der Waals interaction. *American Journal of Physics*, 69(4):441–449, 2001.
- [104] Y. Zou, L. Kilian, A. Scholl, T. Schmidt, R. Fink, and E. Umbach. Chemical bonding of ptcda on ag surfaces and the formation of interface states. *Surface Science*, 600:1240–1251, 2006.
- [105] M. Coreno, M. de Simone, K. C. Prince, R. Richter, M. Vondracek, L. Avaldi, and R. Camilloni. Vibrationally resolved oxygen $K \rightarrow \pi^*$ spectra of O₂ and CO. *Chem. Phys. Lett.*, 306(5-6):269–274, 1999.
- [106] Y. Ma, C. T. Chen, G. Meigs, K. Randall, and F. Sette. High-resolution k-shell photoabsorption measurements of simple molecules. *Physical Review A*, 44(3):1848–1858, 1991.
- [107] Y. Jugnet, F. J. Himpsel, P. Avouris, and E. E. Koch. High-resolution C 1s and O 1s core-excitation spectroscopy of chemisorbed, physisorbed, and free CO. *Phys. Rev. Lett.*, 53(2):198–201, 1984.
- [108] H. Koppel, F. X. Gadea, G. Klatt, J. Schirmer, and L. S. Cederbaum. Multistate vibronic coupling effects in the K-shell excitation spectrum of ethylene: Symmetry breaking and core-hole localization. *J. Chem. Phys.*, 106(11):4415–4429, 1997.
- [109] K. C. Prince, R. Richter, M. De Simone, and M. Corone. X-ray absorption spectra of some small polyatomic molecules. *Surface Review and Letters*, 9(1):159–164, 2002.
- [110] A. B. Trofimov, E. V. Gromov, H. Koppel, J. Schirmer, K. C. Prince, R. Richter, M. De Simone, and M. Corenok. A theoretical study of the 1b(1)(O 1s $\rightarrow \pi^*$) and (1)a(1)(O 1s $\rightarrow 3s$) excited states of formaldehyde. *J. Phys. B: At., Mol. Opt. Phys.*, 36(18):3805–3816, 2003.
- [111] R. Follath and F. Senf. New plane-grating monochromators for third generation synchrotron radiation light sources. *Nuclear Instruments & Methods in Physics Research Section a-Accelerators Spectrometers Detectors and Associated Equipment*, 390(3):388–394, 1997.
- [112] J.T. Seiders, E.L. Elliott, G.H. Grube, and J.S. Siegel. *J. Am. Chem. Soc.*, 121:7804–7813, 1999.

- [113] Y. Saitoh, H. Kimura, Y. Suzuki, T. Nakatani, T. Matsushita, T. Muro, T. Miyahara, M. Fujisawa, K. Soda, S. Ueda, H. Harada, M. Kotsugi, A. Sekiyama, and S. Suga. Performance of a very high resolution soft x-ray beamline BL25SU with a twin-helical undulator at spring-8. *Review of Scientific Instruments*, 71(9):3254–3259, 2000.
- [114] D.W. Rahkonen and M.O. Krause. Total and partial atomic-level widths. *Atomic and Nuclear Data Tables*, 14:139, 1974.
- [115] P.M. Morse. Diatomic molecules according to the wave mechanics. ii vibrational levels. *Physical Review*, 34:57–64, 1929.
- [116] R. Püttner, I. Dominguez, and et al. Vibrationally resolved o 1s core-excitation spectra of CO and NO. *Physical Review A*, 59:3415–3423, 1999.
- [117] W. Brütting, S. Berleb, and A.G. Mückel. Device physics of organic light-emitting diodes based on molecular materials. *Organic Electronics*, 2:1–36, 2001.
- [118] W. Brutting, S. Berleb, and A.G. Muckl. Space-charge limited conduction with a field and temperature dependent mobility in Alq light-emitting devices. *Synthetic Metals*, 122(1):99–104, 2001.
- [119] H. E. Katz. Organic molecular solids as thin film transistor semiconductors. *J. Mater. Chem.*, 7(3):369–376, 1997.
- [120] H. Hoppe and N. S. Sariciftci. Organic solar cells: An overview. *J. Mater. Res.*, 19(7):1924–1945, 2004.
- [121] E. Umbach, M. Sokolowski, and R. Fink. Substrate-interaction, long-range order, and epitaxy of large organic adsorbates. *Applied Physics a-Materials Science & Processing*, 63(6):565–576, 1996.
- [122] V. Shklover, F. S. Tautz, R. Scholz, S. Sloboshanin, M. Sokolowski, J. A. Schaefer, and E. Umbach. Differences in vibronic and electronic excitations of PTCDA on Ag(111) and Ag(110). *Surface Science*, 454:60–66, 2000.
- [123] F. S. Tautz, S. Sloboshanin, J. A. Schaefer, R. Scholz, V. Shklover, M. Sokolowski, and E. Umbach. Vibrational properties of ultrathin PTCDA films on Ag(110). *Physical Review B*, 61(24):16933–16947, 2000.

- [124] V. Shklover. *mündliche Mitteilung*, 2000.
- [125] M. Staufer, U. Birkenheuer, T. Belling, F. Nortemann, N. Rosch, W. Widdra, K. L. Kostov, T. Moritz, and D. Menzel. The vibrational structure of benzene adsorbed on Si(001). *J. Chem. Phys.*, 112(5):2498–2506, 2000.
- [126] C. Buchberger M. Bertram R. Fink E. Umbach D. Gador, Y. Zou. Nexafs investigations of ntcd a monolayers on different metal substrates. *J. Elec. Spec. Rel. Phen.*, 103:523, 1999.
- [127] D. Gador, C. Buchberger, R. Fink, and E. Umbach. Characterization of high-quality NTCDA films on metal substrates. *J. Electron. Spectrosc. Relat. Phenom.*, 96:11–17, 1998.
- [128] A. Schöll, Y. Zou, T. Schmidt, R. Fink, and E. Umbach. High-resolution photoemission study of different NTCDA monolayers on Ag(111): Bonding and screening influences on the line shapes. *J. Phys. Chem. B*, 108(38):14741–14748, 2004.
- [129] A. Schöll, Y. Zou, M. Jung, T. Schmidt, R. Fink, and E. Umbach. Line shapes and satellites in high-resolution X-ray photoelectron spectra of large pi-conjugated organic molecules. *J. Chem. Phys.*, 121(20):10260–10267, 2004.
- [130] Savoie R. The raman effect vol.2, applications, edited by by a. anderson. *Marcel Dekker, Inc. New York*, 1973.
- [131] A. S. Davydov. *Theory of Molecular Excitons*. Plenum Press, New York, 1971.
- [132] AE. Frisch and M. Frisch. Gaussian 98. *Gaussian 98 User’s Reference*, *Gaussian Inc., Pittsburgh PA*, 1998.
- [133] M.J. Frisch et al. Gaussian 98 user’s reference, gaussian inc., pittsburgh pa. 1998.
- [134] G. Rauhut and P. Pulay. Transferable scaling factors for density-functional derived vibrational force-fields. *J. Phys. Chem.*, 99(10):3093–3100, 1995.
- [135] A.D. Becke. Density-functional thermochemistry .3. the role of exact exchange. *J. Chem. Phys.*, 98(7):5648–5652, 1993.

- [136] A.D. Becke. Density-functional exchange-energy approximation with correct asymptotic-behavior. *Physical Review A*, 38(6):3098–3100, 1988.
- [137] J. P. Perdew and Y. Wang. Accurate and simple analytic representation of the electron-gas correlation-energy. *Physical Review B*, 45(23):13244–13249, 1992.
- [138] A. Gbureck. Dissertation universität würzburg. 1998.
- [139] B.G. Frederick, G.L. Nyberg, and N.V. Richardson. Spectral restoration in hreels. *J. Electron. Spectrosc. Relat. Phenom.*, 64/65:825, 1993.
- [140] Frederick B.G., Frederick B.B., and Richardson N.V. Multiple scattering contributions and defining the background for resolution enhancement in hreels. *Surface Science*, 368:82–95, 1996.
- [141] R. Aroca. Surface enhanced vibrational spectra of NTCDA on metal island films. *Asian Journal of Physics*, 7(2):391–404, 1998.
- [142] D. Gador, Y. Zou, C. Buchberger, M. Bertram, R. Fink, and E. Umbach. Nexafs investigations of NTCDA monolayers on different metal substrates. *J. Electron. Spectrosc. Relat. Phenom.*, 103:523–528, 1999.
- [143] F. S. Tautz, S. Sloboshanin, V. Shklover, R. Scholz, M. Sokolowski, J. A. Schaefer, and E. Umbach. Substrate influence on the ordering of organic submonolayers: a comparative study of PTCDA on Ag(110) and Ag(111) using hreels. *Appl. Surf. Sci.*, 166(1-4):363–369, 2000.
- [144] V. Shklover, S. Schmitt, E. Umbach, F. S. Tautz, M. Eremtchenko, Y. Shostak, J. A. Schaefer, and M. Sokolowski. Strong K-induced changes in perylene-tetracarboxylic-dianhydride films on Ag(110) studied by HREELS and LEED. *Surface Science*, 482:1241–1248, 2001.
- [145] F. S. Tautz, M. Eremtchenko, J. A. Schaefer, M. Sokolowski, V. Shklover, and E. Umbach. Strong electron-phonon coupling at a metal/organic interface: PTCDA/Ag(111). *Physical Review B*, 65(12), 2002.
- [146] M. Rocca, Y. B. Li, F. B. Demongeot, and U. Valbusa. Surface-plasmon dispersion and damping on Ag(111). *Physical Review B*, 52(20):14947–14953, 1995.

- [147] C. K. Chan, E. G. Kim, J. L. Bredas, and A. Kahn. Molecular n-type doping of 1,4,5,8-naphthalene tetracarboxylic dianhydride by pyronin b studied using direct and inverse photoelectron spectroscopies. *Advanced Functional Materials*, 16(6):831–837, 2006.
- [148] A. Nollau, M. Pfeiffer, T. Fritz, and K. Leo. Controlled n-type doping of a molecular organic semiconductor: Naphthalenetetracarboxylic dianhydride (NTCDA) doped with bis(ethylenedithio)-tetrathiafulvalene (BEDT-TTF). *J. Appl. Phys.*, 87(9):4340–4343, 2000.
- [149] H. Tachikawa and H. Kawabata. Hybrid density functional theory (DFT) study on electronic states of halogen-substituted organic-inorganic hybrid compounds: Al-NTCDA. *Jpn. J. Appl. Phys., Part 1*, 44(6A):3769–3773, 2005.
- [150] N Karl. Charge carrier transport in organic semiconductors. *Synthetic Metals*, 133:649–657, 2003.
- [151] Norbert Karl and Jörg Marktanner. Structural order and photoelectric properties of organic thin films. *Mol. Cryst. Liq. Cryst. Sci. Technol.*, 315:163 – 168, 1998.
- [152] R. Strohmaier, C. Ludwig, J. Petersen, B. Gompf, and W. Eisenmenger. STM investigations of NTCDA on weakly interacting substrates. *Surface Science*, 351(1-3):292–302, 1996.
- [153] A. Schöll, L. Kilian, Y. Zou, S. Hame J.Ziroff, F. Reinert, E. Umbach, and R.H. Fink. Disordering of an organic overlayer on a metal surface upon cooling. *Science*, 329:303–305, 2010.
- [154] M. Rocca and F. Moresco. HREELS and ELS-LEED studies of surface plasmons on Ag and Pd single crystals. *Progr. Surf. Sci.*, 53 (2-4):331–340, 1996.
- [155] E Umbach. Satellite structures in photoemission spectra from different types of adsorbates. *Surface Science*, 117 (1-3):482–502, 1982.
- [156] B. Azzedine, F. Forster, A. Schöll, D. Batchelor, J. Ziroff, E. Umbach, and F. Reinert. Electronic structure of 1 ML NTCDA/Ag(111) studied by photoemission spectroscopy. *Surface Science*, 601:4013–4017, 2007.
- [157] J. Stanzel, W. Weigand, L. Kilian, H. L. Meyerheim, C. Kumpf, and E. Umbach. Chemisorption of NTCDA on Ag(111): a NIXSW study including non-dipolar and electron-stimulated effects. *Surface Science*, 571(1-3):L311–L318, 2004.

- [158] U. Gomez, M. Leonhardt, H. Port, and HC Wolf HC. Optical properties of amorphous ultrathin films of perylene derivatives. *Chem. Phys. Lett.*, 268 (1-2):1–6, 1997.
- [159] M. J. Rice, N. O. Lipari, and S. Strässler. Dimerized organic linear-chain conductors and the unambiguous experimental determination of electron-molecular-vibration coupling constants. *Phys. Rev. Lett.*, 39:1359 – 1362, 1977.
- [160] M.J. Rice, V. M. Yartsev, and C. S. Jacobsen. Investigation of the nature of the unpaired electron states in the organic semiconductor N-methyl-N-ethylmorpholinium-tetracyanoquinodimethane. *Phys. Rev. B*, 21:3437 – 3446, 1980.
- [161] M.J. Rice. Towards the experimental determination of the fundamental microscopic parameters of organic ion-radical compounds. *Solid State Communications*, 31 (2):93–98, 1979.
- [162] A. Graja. *Organic conductors*. Marcel Dekker, New York, 1994.
- [163] Root. <http://root.cern.ch/>.
- [164] Tautz. Vibrational dynamics of semiconductor surfaces and interfaces probed by inelastic electron scattering. *Habilitationschrift*, 2000.
- [165] A. Devos and M. Lannoo. Electron-phonon coupling for aromatic molecular crystals: Possible consequences for their superconductivity. *Phys. Rev. B*, pages 8236–8239, 1998.
- [166] C.J. Brabec. Organic photovoltaics: technology and market. *Solar Energy Materials and Solar Cells*, 83(2-3):273–292, 2004.
- [167] C. D. Dimitrakopoulos and P. R. L. Malenfant. Organic thin film transistors for large area electronics. *Adv. Mater.*, 14(2):99–117, 2002.
- [168] Q. Chen, T. Rada, A. McDowall, and N. V. Richardson. Epitaxial growth of a crystalline organic semiconductor: Perylene/Cu110. *Chem. Mater.*, 14(2):743–749, 2002.
- [169] T. Schmidt. Entwicklung einer verbesserten elektronenbeugungsapparatur. *Diplomarbeit, Universität Hannover*, 1990.
- [170] M. Sokolowski and H. Pfnür. Continuous order-disorder phase-transitions of the $p(2 \times 2)$ and $(\sqrt{3} \times \sqrt{3})R30$ -degrees superstructures of sulfur on $\text{ru}(001)$ - effective critical exponents and finite-size effects. *Physical Review B*, 49(11):7716–7728, 1994.

- [171] S.R. Forrest and Y. Zhang. Ultrahigh-vacuum quasiepitaxial growth of model van der waals thin films. i. theory. *Physical Review B*, 49:11297 – 11308, 1994.
- [172] R. Strohmaier. A systematic STM study of planar aromatic molecules on inorganic substrates. *Surface Science*, 418:91–104, 1998.
- [173] M. Lepage, M. Michaud, and L. Sanche. Low energy electron total scattering cross section for the production of CO within condensed methanol. *J. Chem. Phys.*, 107 (9):3478–3484, 1997.
- [174] M. Lepage, M. Michaud, and L. Sanche. Low-energy electron scattering cross section for the production of CO within condensed acetone. *J. Chem. Phys.*, 113 (9):3602–3608, 2000.

Danksagung

Bevor ich mit dieser Arbeit schlieÙe, möchte ich mich noch bei denen bedanken, die in der einen oder anderen Weise am Gelingen dieser Arbeit ihren Anteil hatten.

An erster Stelle möchte ich mich bei Herrn Prof. Eberhard Umbach für die Möglichkeit, diese Arbeit an seinem Lehrstuhl anfertigen zu können, für die sowohl interessante als auch aktuelle Themenstellung und vor allem für die Geduld in der Finalisierung bedanken.

Weiter gilt mein Dank Prof. Dr. Rainer Fink für die Betreuung, Beratung, Hilfe bei physikalischen Diskussionen und das fast zeitnahe Korrektur lesen. Dr. Achim Schöll für zahllose hilfreiche Diskussionen. Dr. Vitaly Shklover, der mir zeigte, wie langsame Elektronen zu bändigen sind. Dr. Florian Holch für die Zeit der immer wieder herausfordernden und zahlreichen Strahlzeiten an Synchrotronquellen während der Gasphasen Messungen. Fehlen dürfen nicht Dr. Thomas Schmid für die zahlreichen und detaillierten Diskussionen im Einsatz bei BESSY und Dr. David Batchlor für die Beamlinebetreuung.

Bei den Betreuern des Computerpools, die stets für einen reibungsarmen Ablauf sorgten und immer für Fragen offen waren.

Weiter gilt mein Dank Frau Lukacs für die aufwendige Kristallpolitur und den Mitarbeitern der Elektronik- und Mechanikwerkstatt der Universität für ihre stets zuverlässige und schnelle Arbeit.

Allen Mitgliedern der Arbeitsgruppen Umbach danke ich für die angenehme Atmosphäre und die gute Zusammenarbeit.

Weiter möchte ich mich bei meiner Frau Diana Hübner für die sorgfältige Durchsicht meines Manuskripts und große Geduld in den letzten Jahren bedanken.

Erklärung

Ich versichere hiermit, dass ich die vorliegende Dissertation selbst verfasst und keine anderen als die angegebenen Quellen und Hilfsmittel verwendet habe.

Willsbach, den 17. November 2010

Dominique Hübner